Analysis of the Non-Isothermal Impaction-Spreading
and Freezing of Metal Droplets

by

George Kristian Schwenke

B. S. Chemical Engineering
Rensselaer Polytechnic Institute, 1994

Submitted to the Department of
Materials Science and Engineering
in Partial Fulfillment of the Requirements
for the Degree of

Master of Science
in
Materials Science and Engineering
at the
Massachusetts Institute of Technology

June, 1996

© Massachusetts Institute of Technology

Signature of Author ..../.................. ....
Department of Materials Science and Engineering
May 10, 1996

Certified by ....
Merton C. Flemings
Toyota Professor
Thesis Supervisor

Accepted by ....
Michael F. Rubner
TDK Professor of Materials Science and Engineering
Chair, Departmental Committee on Graduate Students

Analysis of the Non-Isothermal Impaction-Spreading
and Freezing of Metal Droplets

by

George Kristian Schwenke

Submitted to the Department of Materials Science and Engineering on May 10, 1996
in Partial Fulfillment of the Requirements for the Degree of Master of Science
in Materials Science and Engineering

ABSTRACT

A combined theoretical and experimental study has yielded new experimental data and a comprehensive model considering the flight. impact, spreading, and freezing of metal droplets on a solid substrate. The spreading model combines the best features of the analytic and numerical modeling approaches: transient modeling capability without computational complications. It is based on a combination of an integral energy balance and a transient force on the splat. Viscous, surface tension, and solidification effects are considered for an assumed cylindrical geometry. A new effect, energy loss to solidification, is considered in addition to these terms. Solidification energy is the energy lost as moving liquid freezes into stationary solid. Heat transfer modeling considers all sources of thermal resistance in the system and shows that the interface is limiting in most cases. A delayed solidification start for superheated droplets makes flow reversal possible by permitting the liquid to recoil some distance without leaving frozen solid below it. The Reynolds Number, Weber Number, and solidification delay time are critical parameters in determining spreading behavior.

Two experimental campaigns were run - one at MIT and one at NASA's Marshall Space Flight Center. Samples were levitation melted and then released to free-fall and subsequently impact. Drop heights at the two sites are such that a wide window of conditions was achieved. A direct high-speed digital photographic technique yields a series of clear, transient spreading images.

For conditions typical of the MIT experiments, frequent flow reversal and droplet oscillation are observed. The model output and observed spreading behavior match well. Results of two independent experiments under similar conditions confirm this consistency. The agreement is best for moderately superheated droplets with a solidification delay time long enough to permit some flow reversal, but not so long as to approach the fully liquid regime. The model also does a good qualitative job of describing the Marshall Space Flight Center experiments, though the quantitative agreement is not as good. Specifically, the observed initial spreading rate is higher than that predicted, and the extent of back flow tends to be exaggerated.

Thesis Supervisor: Professor Merton C. Flemings
Title: Toyota Professor of Materials Science and Engineering

TABLE OF CONTENTS

TABLE OF FIGURES

VARIABLE DEFINITIONS

Symbol	Meaning
a	Acceleration
A_c	Cross-Sectional Area for Heat Transfer
A_0	Initial Cylinder Surface Area
α	General, Liquid Thermal Diffusivity
α'	Solid Thermal Diffusivity
α''	Substrate Thermal Diffusivity
α_e	Constant in Electrical Conductivity - Temperature Relation
b	Liquid Layer Thickness
b_0	Initial Cylinder Height
β	Dimensionless Liquid Thickness
β_e	Constant in Electrical Conductivity - Temperature Relation
Bi	Biot Number
C	Constant in Electrical Conductivity - Temperature Relation
C_d	Drag Coefficient
c_p	General, Liquid Heat Capacity
c_p'	Solid Heat Capacity
c_p''	Substrate Heat Capacity
c_{pm}	Melting Point Heat Capacity
D_d	Sphere Diameter
E	Viscosity Activation Energy
E_g	Gravitational Energy of Splat
E_{gd}	Gravitational Energy of Droplet
E_k	Kinetic Energy of Splat
E_{kd}	Kinetic Energy of Droplet
E_{sd}	Surface Energy of Droplet
E_{sfc}	Surface Energy of Splat
E_{sol}	Solidification Losses
ε	Emissivity
ε_k	Dimensionless Splat Kinetic Energy
ε_{sfc}	Dimensionless Splat Surface Energy
ε_{sol}	Dimensionless Splat Solidification Losses
F	Freezing Number
Fr	Froude Number
f_s	Fraction Solid
f_s'	Integration Variable
F_{sfc}	Surface Tension Force
F_v	Viscous Force
g	Acceleration of Gravity
g_r	Radial Gravity Component
g_z	Axial Gravity Component
h	Interfacial Heat Transfer Coefficient

h_f	Latent Heat of Fusion
h_g	Convective Heat Transfer Coefficient
k	General, Liquid Thermal Conductivity
k'	Solid Thermal Conductivity
k''	Substrate Thermal Conductivity
k_g	Thermal Conductivity of Gas
l_f	Dimensionless Splat Viscous Losses
L_f	Viscous Losses
m	Splat Mass
μ	Viscosity
μ_0	Viscosity Pre-exponential
N_1	Dimensionless Liquid-to-Interface Thermal Resistance Ratio
N_2	Dimensionless Solid-to-Interface Thermal Resistance Ratio
N_3	Dimensionless Substrate-to-Interface Thermal Resistance Ratio
N_4	Dimensionless Freezing Velocity to Heat Flux Ratio
N_5	Dimensionless Temperature Difference
P	Pressure
Pr_g	Prandtl Number with respect to gas properties
q	Heat Flux
q_{conv}	Convective Heat Flux
q_{rad}	Radiative Heat Flux
Q	Dimensionless Heat Flux
θ	Contact Angle
r	Radial Coordinate
R	Splat Radius
R_d	Initial Spherical Droplet Radius
R_g	Gas Constant
R_s	Solid Radius
R_0	Initial Cylinder Thickness
Re	Reynolds Number
Re_g	Reynolds Number with respect to gas properties
ρ	General, Liquid Density
ρ'	Solid Density
ρ''	Substrate Density
ρ_m	Melting Point Density
σ	Surface Tension
σ_e	Electrical Conductivity
σ_m	Melting Point Surface Tension
σ_{sb}	Stefan-Boltzman Constant
t	Time
t'	Integration Variable
t_{min}	Minimum Free-Fall Time
t_r	Local Solidification Time
t_s	Solidification Delay Time

T	Temperature
T_d	Droplet Impact Temperature
T_g	Gas Temperature
T_m	Melting Temperature
T_s	Substrate Temperature
τ	Dimensionless Time
$\bar{\tau}$	Shear Stress
τ_r	Dimensionless Local Solidification Time
τ_s	Dimensionless Solidification Delay Time
U	Solidification Constant
v	Droplet Impact Velocity
v_{max}	Maximum Free-Fall Velocity
v_r	Radial Velocity
$\bar{v}_r$	Average Radial Velocity
v_z	Axial Velocity
V_s	Solid Volume
We	Weber Number
ξ	Dimensionless Radius; Spreading Extent
ξ_f	Final Spreading Extent
ξ_{lim}	Limiting Spreading Extent
ξ_s	Solid Spreading Extent
z	Axial Coordinate
z'	Integration Variable
z_s	Solid Layer Thickness
Z	Dimensionless Solid Thickness

ACKNOWLEDGMENTS

CHAPTER 1 - INTRODUCTION

1.1 Motivation

As technology in the aerospace, electronics, chemical processing, and other industries has advanced in recent years. new demands for material performance have arisen. The need for superior mechanical. corrosion resistance, and electronic properties has prompted the evolution of the Materials Processing Age. To obtain properties capable of fulfilling today's most challenging needs, a number of Rapid Solidification Processes have been developed. The extremely high cooling rates characteristic of these processes have the ability to produce very fine micro-structures, and to reduce segregation of alloying elements. To achieve these cooling rates, techniques such as melt spinning, spray cooling, and splat-quenching are used.

Two important Rapid Solidification Processes are Plasma Spraying and Spray Forming. These techniques also have the beneficial capability of melting refractories. Plasma Spraying involves feeding a powder into a plasma so that tiny particles melt while being accelerated towards a solid substrate, which is being coated. When a droplet hits, it spreads out and freezes. producing a solid coating in sequential thin layers. The process is frequently used in industry to apply thin coatings to pieces, and when the melting temperature of the coating material precludes other methods. Thermal Spraying is similar, but is typically used to fabricate near net shape parts rather than just coat them. In both cases, particle sizes are of the order of tens or hundreds of microns, and velocities are of the order of 100 m/s.

The industrial application of both processes still present challenges, however. If the operating conditions are not ideal, droplets can freeze in flight and bounce off the surface, or they can encounter liquid remaining from previous droplets upon impact. They can also fragment while spreading, or freeze in such a way as to trap gas or leave pores. Wetting, adhesion, ejection, and porosity are all concerns in such operations.

There is a great interest in understanding the mechanism by which an initially molten droplet impacts a solid surface. spreads out, and freezes. The droplet will spread initially as its axial momentum is redirected outwards by the pressure rise on impact. Viscous forces within the liquid, and surface tension forces at its boundary restrain this motion, all while solid grows from the droplet-substrate interface into the liquid. In the general case, the problem involves coupled heat transfer and fluid flow involving a changing free surface. Problems of this type are exceedingly difficult to solve. either analytically or numerically, so that simplifying assumptions are usually required.

Many researchers have examined this problem, trying to find a way to predict the spreading and freezing behavior of the droplet as a function of process parameters, in the hope of determining optimal conditions and minimizing the extent of the problems mentioned above. Research has also been done in closely related areas such as spray cooling[1], impact erosion[2], and 3-D printing. The published models differ widely in approach, considerations, and applicability. One goal of this work is to review some of the existing models, and to examine the conditions under which they are valid.

Undercooled liquid droplets striking a solid substrate possess the greatest driving force to solidify, and so have to potential to solidify at the highest rates, yet little work has been done on the impingement behavior of undercooled droplets. A strong glass-forming tendency in the undercooled droplet further complicates matters, because formation of an amorphous solid phase is now possible instead of, or in addition to a crystalline solid phase. It is another goal of this project to lay the groundwork for a comprehensive investigation of the impingement behavior of undercooled and glass-forming droplets. The analytic and experimental techniques reported in this study will soon be extended to just such a case.

1.2 Theory

In order to review and discuss the approaches and models proposed thus far, it is first necessary to define the problem in terms of the appropriate physical and mathematical

framework. First, the system geometry will be described, followed by the relevant fluid mechanics and heat transfer equations.

1.2.1 Geometry

To minimize its surface energy, any free-falling liquid droplet will assume a spherical shape, once sufficient time has passed for damping of oscillations induced in formation. Following impact on a flat substrate, the spherical droplet forms a splat with cylindrical geometry, as axial motion is redirected radially outwards. Angular variation is usually neglected because prediction of fluctuations at the splat periphery would require precise knowledge of the small scale irregularities in the droplet and/or substrate surfaces. This assumption, while it greatly simplifies the governing equations, prevents any attempt to predict the break-up into "fingers" that is quite commonly observed. Figure 1 is a schematic sketch of the system, before and after impact. Several important geometric variables are also shown. R_d and R are the radii of the initial droplet and subsequent splat; z_s and b are the solid and liquid axial thicknesses, respectively.
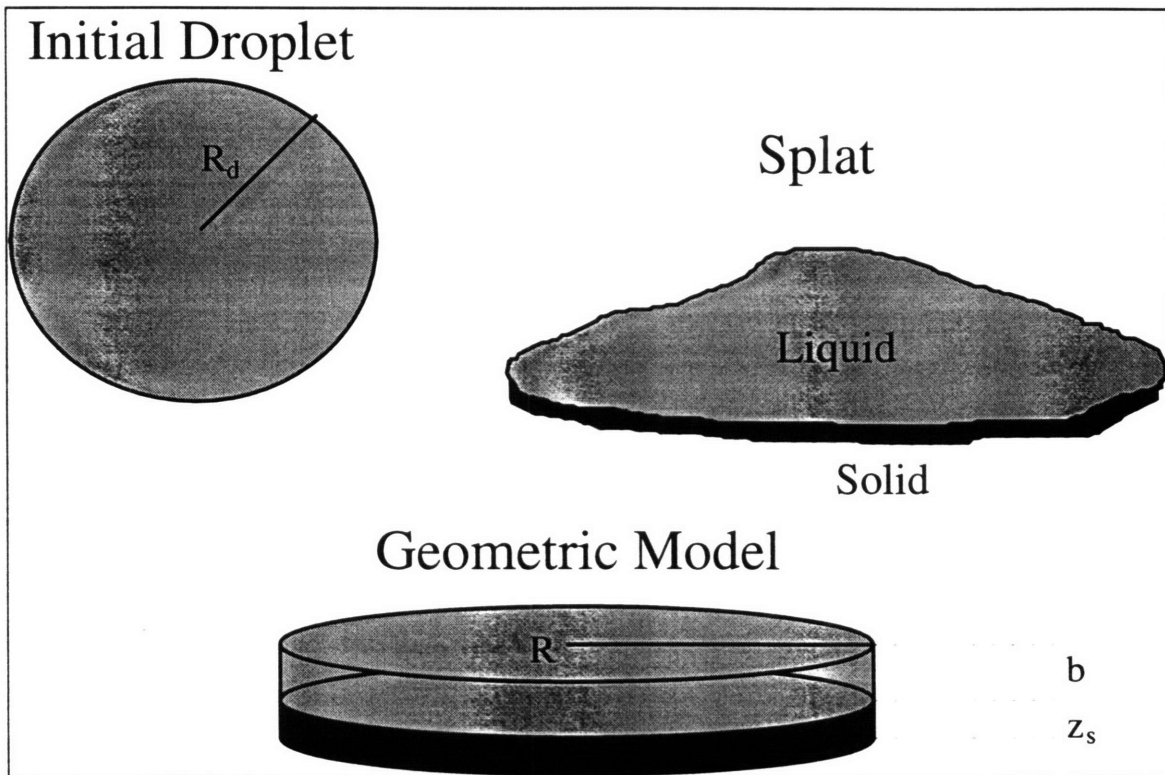
Figure 1: System Geometry

1.2.2 Fluid Mechanics

With a cylindrical coordinate system chosen, the fluid mechanics can be summarized by the Navier-Stokes Equations for an incompressible, Newtonian fluid:

$$\frac{1}{r}\frac{d}{dr}(r\,v_r) + \frac{d}{dz}(v_z) = 0 \qquad [1]$$

$$\rho\left(\frac{d v_r}{dt} + v_r\frac{d v_r}{dr} + v_z\frac{d v_r}{dz}\right) = -\frac{dP}{dr} + \mu\left[\frac{d}{dr}\left(\frac{1}{r}\frac{d}{dr}(r\,v_r)\right) + \frac{d^2 v_r}{dz^2}\right] + \rho g_r \qquad [2]$$

$$\rho\left(\frac{d v_z}{dt} + v_r\frac{d v_z}{dr} + v_z\frac{d v_z}{dz}\right) = -\frac{dP}{dz} + \mu\left[\frac{1}{r}\frac{d}{dr}\left(r\frac{d v_z}{dr}\right) + \frac{d^2 v_z}{dz^2}\right] + \rho g_z \qquad [3]$$

In equations 1-3, r and z are the radial and axial coordinates, t is time, v_r and v_z are the radial and axial velocities, ρ is the liquid density, μ its viscosity, P the pressure, and g_r and g_z the acceleration of gravity in the r and z directions. Equation 1 represents the requirement of continuity. Equations 2 and 3 are the radial and axial momentum balances, respectively. The boundary conditions dictate centerline symmetry, no slip at the substrate surface, and no shear stress at the free surface.

1.2.3 Heat Transfer

For small-sized spheres of high thermal conductivity, temperature gradients within the droplet are negligible, so that a spatially uniform temperature may be assumed at impact. Three possibilities exist for the thermal state of the droplet at impact: superheated, subcooled, or neither. If the droplet is superheated, some sensible heat must be removed before solidification begins. If it is undercooled, impact will cause nucleation and recalescense. thereby raising the temperature back to the melting point in the vicinity of the solidification front.

At time zero, the whole droplet is at some temperature, T_d, and the entire substrate is at T_s. Initially, only the splat-substrate interface provides any resistance to heat flow. As time proceeds. heat-affected zones grow on both sides of this interface, and solidification starts after the droplet side of the interface reaches the melting point, T_m.

14

The heat conducted out of the droplet and into the substrate must pass, in turn, through the heat-affected zone in the liquid, any solidified metal present, the droplet-substrate interface, and the heat-affected zone in the substrate. These four obstacles present four thermal resistances in series, across which a common total temperature difference exists. The resulting heat flow is the quotient of the temperature driving force and the sum of the various resistances.

For axial conduction, the heat diffusion equation,

$$k\frac{d^2 T}{dz^2} = \rho c_p \frac{dT}{dt}$$

[4]

applies in a medium of thermal conductivity k, density ρ, and heat capacity c_p. The boundary conditions dictate heat flux continuity between media and across the interface:

$$q = -k\frac{dT}{dz} = h\Delta T$$

[5]

q is the heat flux, and h is the interfacial heat transfer coefficient.

1.2.4 Dimensionless Numbers

When considering many simultaneous yet distinct effects on a system, it is frequently useful to compare the relative importance of two or more of these tendencies. It is also generally advantageous to formulate the governing equations in dimensionless form so that a wide range of conditions may be easily considered. Many authors introduce similar dimensionless variables representing normalized time and length ratios. In formulating the equations in terms of these quantities, other dimensionless numbers - representing such importance ratios drop out. Some of the more important dimensionless variables and numbers are defined below:

$$\tau = \frac{vt}{2R_d} = \text{Dimensionless Time}$$

[6]

$$\xi = \frac{R}{R_d} = \text{Dimensionless Radius; Spreading Extent}$$

[7]

15

$$\beta = \frac{b}{2R_d} = \text{Dimensionless Liquid Thickness} \qquad [8]$$

$$Z = \frac{z_s}{2R_d} = \text{Dimensionless Solid Thickness} \qquad [9]$$

$$\text{Re} = \frac{2\rho v R_d}{\mu} = \text{Reynolds Number} = \frac{\text{Inertial Forces}}{\text{Viscous Forces}} \qquad [10]$$

$$\text{We} = \frac{2\rho v^2 R_d}{\sigma} = \text{Weber Number} = \frac{\text{Inertial Forces}}{\text{Surface Tension Forces}} \qquad [11]$$

$$\text{Fr} = \frac{v^2}{2R_d g} = \text{Froude Number} = \frac{\text{Inertial Forces}}{\text{Gravitational Forces}} \qquad [12]$$

σ is the surface tension of the liquid. and v is the droplet's impact velocity.

1.3 Literature Review

With the problem now described, others' modeling attempts are reviewed. A descriptive, chronological summary is provided here; section 1.4 contains a general classification scheme and some discussion.

The first study aimed at characterizing the impact of liquid droplets was reported by Worthington[3]. He conducted experiments in which the splashing of milk and mercury droplets was spark-illuminated and sketched after naked-eye viewing. Even with such a simple set-up, he was able to discern radial rays shooting out from the point of impact, and being overtaken by a spreading cylinder.

Savic and Boult[4] studied the impact behavior of water and paraffin on cold and hot surfaces in a combined theoretical and experimental study. Taking multiple flash-illuminated photographs of each droplet, they obtained transient data for the centerline height.

Harlow and Shannon's Marker-and-Cell Method[5,6] was a pioneering effort in the field of computational fluid mechanics. It involved solving a finite difference approximation to the Navier-Stokes equations, including viscous forces. Surface tension was handled by

16

monitoring the motion of imaginary marker particles that moved with the fluid. This technique was applied to the splashing of a liquid drop[7], but the results presented concentrate on the initial stages only, neglecting viscous and surface tension effects. The salient feature of their analysis is the prediction of two outward-shooting jets originating at the point of droplet impact. The first, they claim, "moves with constant speed 1.6 times greater than the initial impact speed of the droplet.[8]" Their calculations also show a second wave, moving at the droplet impact speed. Shallow and deep pool results are also presented: "Even a very thin film of fluid in the pool is enough to interact appreciably with the lateral sheet jet to produce an upward motion.[9]"

Jones[10] developed an analytic model for the cooling, spreading, and freezing of droplets in rotary atomization. He considered pre-impact flight in addition to spreading. The effects of freezing and surface tension on droplet spreading were judged negligible, and viscous losses were modeled as if the droplet were a cylinder being compressed between two infinite plates. He reported a correlation for the splat aspect ratio as a function of several experimental parameters. The equivalent correlation in terms of final spreading extent, ξ_f, and Reynolds number is:

$$\xi_f = 1.159 \mathrm{Re}^{1/8} \tag{13}$$

Experiments involving rotary atomization of Aluminum and Magnesium produced splat thicknesses five times what Jones predicted. He attributed the discrepancy to surface oxidation, but others have blamed it on "prohibitively restrictive" assumptions.[11]

Madjeski[12] published one of the most famous and most advanced analytic models in 1976. He considered the effects of three spreading restraints - viscous losses, surface tension, and freezing - by performing an overall energy balance on a cylindrical splat. Viscous losses are calculated from shear stresses in an assumed laminar velocity field - the simplest that will fulfill the continuity equation. Liquid-vapor surface tension is considered as well. The droplet is assumed to be at the freezing temperature at impact so that the freezing velocity can be calculated from the solution to a Stefan Problem - conduction of the latent heat of fusion through a growing solid layer. Several limiting-

case solutions to a general equation are presented. For the case of important viscous and surface tension effects, but negligible freezing, the solution is:

$$\frac{3\xi_f^2}{We} + \frac{1}{Re}\left(\frac{\xi_f}{1.2941}\right)^5 = 1 \qquad [14]$$

for Re>100 and We>100.

Madjeski conducted experiments using Tin and Lead droplets thrown on Copper, Aluminum, and insulating substrates, inclined at various angles. One conclusion was that "the thermal properties of the cold surface on which the droplets solidify [have] essentially no influence on the value of ξ[13]." In 1983[14], he presented more calculations with this model, and extended the treatment to lower Weber and Reynolds numbers. The revised formula is:

$$\frac{3\xi_f^2}{We} + \frac{1}{Re}\left(\frac{\xi_f}{1.2941}\right)^5 = \exp\left(\frac{4.2011}{We^{0.8572}}\right) \qquad [15]$$

for Re>20 and We>10.

Collings et al.[15] present an alternative model, based primarily on surface tension effects. They calculate an upper bound for the spreading extent by neglecting viscous losses and equating the initial kinetic energy of the droplet with its final surface energy. The equilibrium contact angle, determined by Young's equation, is used, except in the case where a gas layer is forms in-between the splat and substrate. In that case, the contact angle, θ, equals 180°. The theoretical model is formulated in terms of the maximum liquid-vapor surface energy, but an equivalent expression in terms of dimensionless numbers exists:

$$\xi_f = \sqrt{\frac{We}{3(1-\cos\theta)}} \qquad [16]$$

Experiments with Nitronic 40W yielded a surface tension roughly twice that commonly reported. They attribute the differences to the fact that the solidified shapes were not always circular and flat, but sometimes hemispherical. Others[16] have questioned the

validity of neglecting viscous terms, and the use of the equilibrium contact angle in a fundamentally dynamic process.

In two papers,[1,17] Chandra and Avedisian examine the deformation behavior of a droplet of liquid n-heptane impacting a solid substrate of varying temperature and porosity. Impact on a liquid film was also studied. In both papers, single flash photography was used, recording a single image at successive times in the deformation of many droplets. Much of the paper is devoted to examining the evaporation behavior as the boiling point of n-heptane is surpassed, but some room temperature experiments are performed. The beautiful pictures they obtained reveal a liquid film or jet shooting out from the point of impact, as well as "rings or waves around the periphery,[18]" especially on a pre-wet surface. Transient spreading results are presented. After comparing their transient data to some of the previously released models, Chandra & Avedisian develop their own using a similar cylindrical geometry energy balance, and an order-of-magnitude approximation for viscous losses. Their relation between the final spreading extent and relevant dimensionless groups is:

$$\frac{3We}{2Re}\xi_f^4 + (1 - \cos\theta)\xi_f^2 - \left(\frac{We}{3} + 4\right) \approx 0 \qquad [17]$$

The contact angle is measured directly from the photographs because it depends on time. Values from 32° to 180° were observed. The predicted ξ_f values are higher than the observed ones by a factor of about 20-25%, likely due to underestimation of viscous losses.

Trapaga & Szekely[19,20] published two papers in which they modeled the isothermal and non-isothermal spreading of molten metal droplets, using the FLOW-3D® numerical simulation package. Results were compared to Savic & Boult, Harlow & Shannon, and Madjeski, with reasonable agreement. "The process of impinging of droplets is characterized mainly as an inertial process.[21]" All droplets initially spread rapidly, then they slow as they flatten out without overshooting. A high speed radial jet was seen to shoot out from the point of impact, but its velocity was three times the impact speed, not

1.6, as reported by Harlow & Shannon. Regression analysis yielded a correlation for the final spreading extent:

$$\xi_f = \text{Re}^{1/5} \tag{18}$$

Spreading extents were less than Madjeski's solidification-free model predicted. The effect of the Weber Number was described as "practically negligible[22]" for $200<\text{We}<2000$ and $100<\text{Re}<10^5$. The principal effect of surface tension is at the edge and towards end of the spreading process. In the non-isothermal study, solidification is seen to have a notable effect in arresting spreading. An average heat transfer coefficient, chosen to make predictions agree with experiments, is used. For this reason, the modeling of heat transfer is judged less rigorous than that of fluid flow.

Fukanuma & Ohmori[23] use a three-zone analytic model and a velocity field with an assumed time dependence to model the deformation process. They assume that viscous dissipation is significant only in the thin cylindrical region nearest the substrate, and they obtain a similar expression for the final spreading extent:

$$\frac{6\xi_f^2}{We} + \frac{1}{Re}\left(\frac{\xi_f}{1.06}\right)^6 = 1 \tag{19}$$

More importantly, they conducted a series of experiments using Tin and Zinc droplets impinging on stainless steel and alumina substrates. The transient data they report indicates that a slight splat shrinkage occurred; they attribute it to contraction upon solidification. Their experiments conditions will be simulated with the new model developed, and the results will be compared to their actual observations.

Sobolev[24] proposed a similar velocity distribution, and published another model. He neglects solidification and surface tension effects, on the assumptions that "the characteristic times of droplet flattening are considerably shorter than the time intervals of subsequent droplet solidification[25]" and that Weber Numbers during thermal spraying significantly exceed unity. His results are compared to Madjeski and to Trapaga & Szekely, and the agreement is good.

Shi et al.[26] measured the transient spreading extent of a water droplet impinging on a hot substrate, using an electrical resistance probe rather than a high-speed camera. Some oscillation was observed. Their experiments, too, will be simulated and used to compare.

Bennett & Poulikakos[27] review many of the existing models and note that there is disagreement in the literature as to whether freezing, viscous dissipation, or surface tension is principally responsible for arresting spreading. They decide that solidification is usually a secondary effect, compared to viscous and surface tension effects, so they attempt "to assess the extent of these separate contributions.[28]" Many previously released models are reviewed, and Bennett & Poulikakos comment upon the authors' assumptions. Collings' surface energy formulation and Madjeski's treatment of viscous dissipation are selected. The importance of using the correct contact angle is stressed, and they point out that the contact angle during spreading is not likely to be the same as that under static conditions. A value of 90° is assumed in their recommended model,

$$\frac{1}{Re}\left(\frac{\xi_f}{1.2941}\right)^5 + \frac{3\left(\xi_f^2 - 4\right)}{We} = 1 \qquad [20]$$

and used to define two distinct regimes, where viscous dissipation and surface tension are dominant in restraining spreading. These regimes are then plotted as a function of dimensionless numbers. Viscous effects disappear rapidly in the surface tension regime, but not vice versa. Such a plot is re-created in Figure 2, with the addition of a "both" region. The success or failure of each previous model is explained in terms of author's considerations and the region in which the experiments lie.

Fukai et al.[29] used a deforming finite element method to simulate droplet spreading, encompassing viscous, surface tension, and gravitational effects, but neglecting solidification. The Artificial Compressibility Method, a variable contact angle, and the abandonment of the no-slip boundary condition were important features of this model. Simulations of water and Tin droplets revealed flow reversal and maximum splat thicknesses at locations other than the center. "The occurrence of droplet recoiling and mass accumulation around the splat periphery are standout features.[30]" In a subsequent

paper[31], they used this model to predict flow reversal and droplet oscillation. Contact Angle Hysterisis was also noted as the dynamic contact angle changed upon reversal. Water droplet experiments on waxed and unwaxed pyrex glass were conducted, and agreed well with predictions.
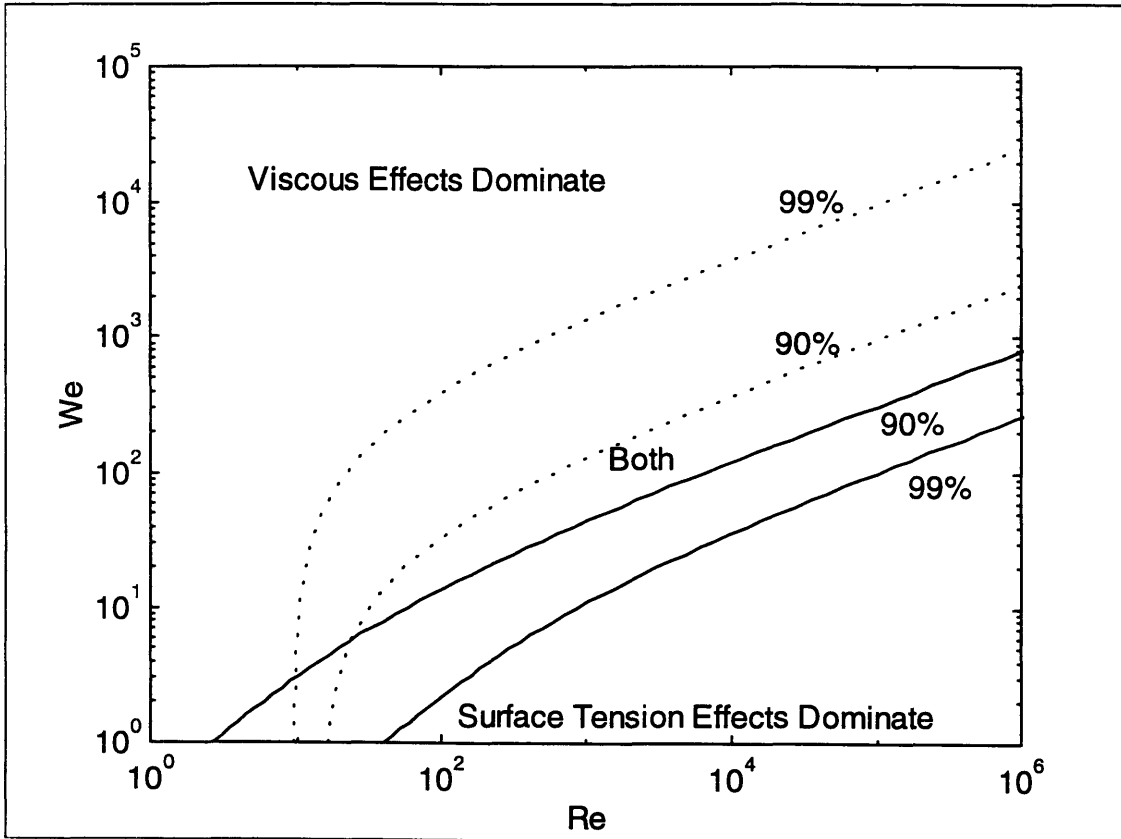
Figure 2: Bennett & Poulikakos' Regimes

Wang & Matthys examined the heat transfer aspects of the problem in their two papers[32,33] by conducting a series of experiments using Nickel droplets on different substrates. Metallic substrates yielded thin centered, thick edged splats whose edges would curl off or lift up. Droplet superheat and substrate properties had little effect, as interfacial heat transfer was limiting. Quartz substrates yielded thicker centered splats with no separation at the edge. Pyrometric temperature measurements of the splat's top surface temperature were compared to a one-dimensional heat transfer model, permitting quantitative evaluation of h. For metallic substrates, dual-valued heat transfer coefficients - one before and one after solidification - gave numeric predictions that

agreed well with the transient temperature data reported. Initially, heat transfer coefficients were near 10^4 W/m²K, but they dropped to near 2000 W/m²K after some time (τ=19 to 65). The first of these numbers is taken as the correct order-of-magnitude estimate for the heat transfer coefficient in the experiments in the present study. The second value was not used for the simple reason that the transition occurs at times that are long in comparison with the fluid flow time scale and the data recording period.

Kang[34] also studied the heat transfer aspects of splat quench solidification. The paper focuses on the development of a two dimensional conduction model for two droplets impacting in succession. The possibilities of droplet undercooling and radial conduction within the substrate are addressed. In addition, a pre-impact flight cooling model is formulated.

In Rolland's[35] comprehensive study of the formation, cooling, and impact of spray forming particles, pre-impact solidification of 100μm-sized Al-4.5% Cu and Al-4.3% Fe droplets is a key consideration. An improved free-fall model is developed, and a Freezing Number, equal to the ratio of the freezing to spreading times, is defined:

$$ F = \frac{\rho D_d^2 v \left(c_p (T_d - T_m) + h_f \right)}{A_c h (T_d - T_s)} \qquad [21] $$

D_d is the diameter of the droplet. h_f is the latent heat of fusion, and A_c is the cross sectional area for heat transfer. This freezing number is used in conjunction with the Weber Number to characterize the impingement behavior or the droplets. Oscillation, recoiling, folding back, bouncing, and curling up are all observed under different conditions.

From this list of published models, the variety of approaches, considerations, and methods is readily apparent.

1.4 Model Review

With some of the more important models introduced, it is now possible to categorize and compare them. Geometrically, some models assume a straight-forward cylindrical

geometry, while others employ more complicated contact angles, zones, or totally variable shapes. Fluid flow considerations include viscous, surface tension, and gravitational effects. Heat transfer modeling complexity ranges from total neglect, through a single controlling thermal resistance, to time-dependent heat transfer coefficients. Some general classifications are proposed first; then some important model considerations and features are examined more closely.

1.4.1 Model Classifications

One important distinction between models is that of their approach: analytic or numerical. Analytic models typically assume some geometry, a velocity field, or an approximation for viscous losses. These assumptions are frequently simplifications, but they can reveal what happens in limiting cases, as well as provide a good, quick idea of the nature of the spreading process. Numerical models rely on computationally intense direct calculations from the basic equations of fluid flow and heat transfer. Initial and boundary conditions are imposed on equations 1-5, and some algorithm is used to track the location and orientation of the free surface. By introducing spatial grids, finite time steps, and other variables, however, numerical models can introduce extra degrees of freedom and uncertainty.

Another classification is that of asymptotic versus transient models. Asymptotic models provide a means of estimating the final value of a variable, but they give no information its evolution. Transient models, however, give fully time-dependent data. Analytic models tend to be asymptotic, as viscous losses are frequently approximated from some classic fluid mechanics problem - such as deformation of a liquid between infinite, parallel plates. Numerical models, by their very nature, are transient. In some cases, asymptotic analytic models can be turned into transient analytic models for side-by-side comparison with numerical efforts and experiments.

1.4.2 Cylindrical Models

An important class of analytic models, the most important of which is Madjeski's, shares the characteristic feature of assuming a cylindrical geometry. In such "cylindrical models," the liquid is assumed to maintain the shape of a right circular cylinder throughout spreading and solid growth. For mass conservation reasons, the initial cylinder must have the same volume as the incident spherical droplet. This requirement establishes a relationship between the cylinder's initial height, b_0, and its radius, R_0,

$$b_0 = \frac{4\,R_d^3}{3\,R_0^2} \qquad\qquad [22]$$

but there is still an extra degree of freedom in being able to arbitrarily specify one or the other. An attractive choice would be to pick the values giving the same surface area as the spherical droplet. However, the cylinder surface area,

$$A_0 = 2\pi\,R_0^2 + 2\pi\,R_0\,b_0 \qquad\qquad [23]$$

will always be greater than that of a sphere of equal volume. Madjeski neglects the contribution of the bottom surface, thereby making such a match possible, but in doing so, he is effectively assuming ideal contact at the splat-substrate interface. This treatment may be appropriate for low-pressure spray forming - when nearly contamination-free metal-to-metal contact is achieved, but it is likely not valid when significant surface roughness is present, or when gas entrapment occurs.

When the real spherical droplet strikes the solid surface, contact is initially at a single point. As spreading proceeds, the contact area grows until the splat in essentially cylindrical. When approximating the splat as a cylinder throughout the spreading process, a smaller initial base area should be able to represent the spreading splat sooner than a larger one. Thus, initially tall and narrow cylinders would be preferred over initially short and wide ones. Also, some viscous energy dissipation occurs before such models effectively start - in the time in-between impact and when the splat shape truly becomes cylindrical. To minimize this undesirable effect, a tall and narrow initial cylinder would again be better than a short, wide one. These trends are counteracted by surface energy considerations, however. As the aspect ratio of a cylinder increases, so

does its surface energy. When the initial cylinder is too thin and tall, its surface energy is much larger than that of the spherical droplet.

Madjeksi[12] uses a cylinder radius equal to that of the sphere; Sobolev[24] uses an initial height of half the sphere diameter. Table 1 compares several of these starting values, and Figure 3 shows them schematically.

Initial Radius, R_0	Initial Height, b_0	Initial Sfc. Area, A_0	Comments
R_d	$2 R_d$	$4 \pi R_d^2$	Initial Sphere
$0.5 R_d$	$5.33 R_d$	$5.83 \pi R_d^2$	Half Radius
$0.82 R_d$	$2 R_d$	$4.60 \pi R_d^2$	Equal Height
$0.87 R_d$	$1.75 R_d$	$4.58 \pi R_d^2$	Minimum Area
R_d	$1.33 R_d$	$4.67 \pi R_d^2$	Equal Radius
$1.16 R_d$	R_d	$4.98 \pi R_d^2$	Half Height
$2 R_d$	$0.33 R_d$	$9.33 \pi R_d^2$	Twice Radius

Table 1: Initial Cylindrical Model Geometry

a)   b)   c)
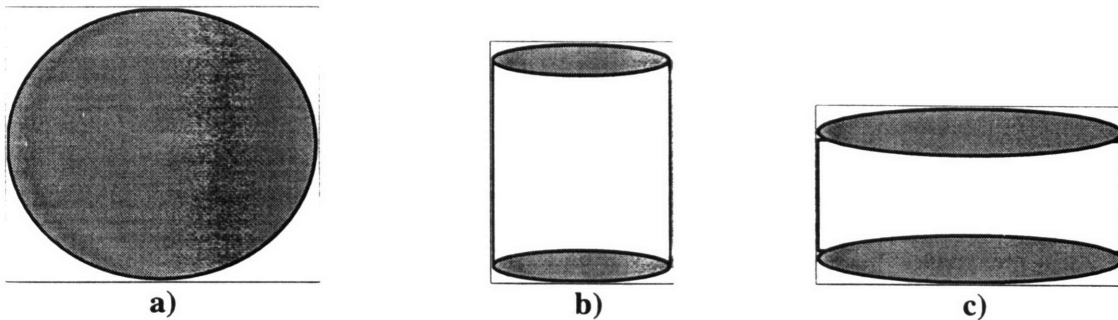
Figure 3: Initial Cylindrical Model Geometry

1.4.3 Energy Balances

Closely related to the asymptotic/transient classification is the issue of energy balances. Most models rely on some sort of energy balance to predict the splat characteristics from impact parameters. In the most general case, the incident droplet has kinetic, surface, and gravitational energies, E_{kd}, E_{sd}, and E_{gd}, respectively. The splat has similar terms, E_k, E_{sfc}, and E_g, plus L_f - the energy that has been lost to viscous friction, and E_{sol} - the kinetic energy lost as moving liquid freezes into stationary solid. Two statements of energy conservation are possible: the differential approach,

26

$$\frac{dE_k}{dt} + \frac{dE_{sfc}}{dt} + \frac{dE_g}{dt} + \frac{dL_f}{dt} + \frac{dE_{sol}}{dt} = 0 \qquad \text{[24]}$$

and the integral approach,

$$E_{kd} + E_{sd} + E_{gd} = E_k + E_{sfc} + E_g + L_f + E_{sol} \qquad \text{[25]}$$

The differential approach, used by Madjeski and others, can more easily give information on the dynamics of the system. The rate of change of the splat's kinetic energy will involve the derivative of the spreading rate, thereby permitting evaluation of this quantity. The weakness of the differential approach lies in the fact that it requires the energy of the system to remain constant, but it does not specify its value. Thus, the initial spreading rate must be determined some other way.

The integral approach reveals the exact value of the total system energy. It permits calculation of the initial spreading rate, but it cannot provide as much dynamic information because it does not involve the derivative of the spreading rate. Asymptotic models frequently employ approximations for L_f when using this approach. Many authors use this approach to calculate the initial spreading rate, but take only the droplet's kinetic energy into account.

A problem with modeling based solely on energy balances is that transient behavior, particularly flow reversal and oscillation, is difficult to predict. When a splat flows out, and then reverses direction, the spreading rate is zero at the moment of greatest spreading extent. While there is still a surface tension force pulling the splat back towards the center, a model based on the integral energy balance approach would not reflect this. Instead, such a calculation would merely reveal that the splat had flowed outward until it reached a point where the surface and viscous energy terms added up to the droplet's initial energy. Once the splat had ceased spreading at its maximum extent, such a pure energy balance model would predict no further change.

1.4.4 Solidification Modeling

As mentioned in section 1.2.3, heat flowing from the droplet into the substrate must pass through four potential barriers before it is dissipated in the substrate. If the liquid and

substrate are considered semi-infinite, a time-dependent thermal resistance can be defined for the heat-affected zone.[36] The resistance encountered in conduction through a solid is simply its length, z_s, divided by its thermal conductivity. Heat transfer at the interface can be represented in terms of a heat transfer coefficient[32], h, so that the resistance is $1/h$. With these expressions, the heat flux, q, can then be evaluated:

$$q = \frac{T_d - T_s}{\sqrt{\dfrac{\pi t}{k \rho c_p}} + \dfrac{z_s}{k'} + \dfrac{1}{h} + \sqrt{\dfrac{\pi t}{k'' \rho'' c_p''}}}$$

[26]

The physical properties included in equation 26 are defined in Table 2.

Region	Thermal Conductivity	Density	Specific Heat
Liquid	k	ρ	c_p
Solid	k'	ρ'	c_p'
Substrate	k''	ρ''	c_p''

Table 2: Physical Property Definitions

Balancing the heat flux with the rate of evolution of latent heat at the interface yields the solidification velocity:

$$\frac{d z_s}{dt} = \frac{q}{\rho h_f}$$

[27]

For a superheated droplet, there will be a length of time during which spreading occurs before solidification begins. Some heat must be extracted before the top side of the interface reaches the melting temperature and freezing starts. This delay time, t_s, is a critical parameter in assessing the spreading behavior of the splat, for it provides a measure of how long the splat will behave as if it were fully liquid. Up until t_s, the liquid heat-affected zone, the interface, and the solid heat-affected zone all resist heat flow between the droplet at T_d and substrate at T_s. The interface will be controlling at first, as it is the only resistance present, but the liquid and substrate heat-affected zones will grow. When the splat side of the interface reaches T_m, at t_s, freezing begins. Heat is now conducted between T_m and T_s, through a growing solid layer, the interface, and the substrate heat-affected zone.

Many previous modelers have sacrificed completeness in order to obtain an analytical solution by neglecting one or more of these facets. Madjeski[12] assumed that solidification commenced immediately and considered only the resistance of the solid layer, thereby solving the Stefan Problem. His solution can be represented by the equation.

$$z_s = 2U\sqrt{\alpha\,t} \qquad [28]$$

where U is the solidification constant, evaluated from the following expression:

$$\frac{\rho\,c_p(T_m - T_s)}{\sqrt{\pi}\,\rho\,h_f} = U erf(U)\exp(U^2) \qquad [29]$$

This solution will likely not be valid during the initial stages of freezing, or when there is poor heat transfer across the splat-substrate interface, because it assumes that the solid resistance is controlling for the entire duration of freezing. It also neglects the delay before solidification begins, so it should not handle superheated droplets well either.

Geiger & Poirier[37] present an analytic solution considering interfacial resistance and a semi-infinite substrate, but neglecting the liquid and solid contributions:

$$z_s = \frac{2k''\rho''c_p''(T_m - T_s)}{\pi h \rho\,h_f}\left[h\sqrt{\frac{\pi t}{k''\rho''c_p''}} - \ln\left(1 + h\sqrt{\frac{\pi t}{k''\rho''c_p''}}\right)\right] \qquad [30]$$

This solution would also have trouble predicting the freezing behavior of significantly superheated droplets, for it does not account for liquid resistance or a delay time either. It should be better able to handle the initial, interface-controlled stage than Madjeski's, but not as good at later times if the solid resistance becomes large. The performance of these approximations will be compared to the output from the solidification model developed in section 2.3.9.

1.4.5 Comparison

Table 3 contains a list of some of the models described above, and how they fit into each of the categories just described.

29

Author	Type	Fluid Flow Considerations	Heat Transfer Considerations	Initial Energy
Harlow & Shannon	Numerical, Transient	None	None	Kinetic
Jones	Analytic, Asymptotic	Viscosity	None	Kinetic
Madjeski	Analytic, Asymptotic	Viscosity, Surface Tension	Solid	Kinetic
Collings	Analytic, Asymptotic	Surface Tension	None	Kinetic, Surface
Chandra & Avedisian	Analytic, Asymptotic	Viscosity, Surface Tension	None	Kinetic, Surface
Trapaga & Szekely	Numerical, Transient	Viscosity, Surface Tension	Solid, Interface, Substrate	Kinetic, Surface
Fukanuma & Ohmori	Analytic, Transient	Viscosity, Surface Tension	None	Kinetic, Surface
Sobolev	Analytic, Transient	Viscosity	None	Kinetic
Bennett & Poulikakos	Analytic, Asymptotic	Viscosity, Surface Tension	None	Kinetic, Surface
Fukai	Numerical, Transient	Viscous, Surface Tension, Gravitational	None	Kinetic, Surface

Table 3: Summary of Models

The spreading model developed in Chapter 2 relies on a force balance approach to evaluate the derivative of the spreading rate and facilitate transient modeling. The force calculated is independent of the splat's kinetic energy, so that the tendency to recoil can be accommodated. A complete integral energy balance is used to find the initial splat spreading rate. The solidification model takes into account all of the resistances mentioned, so it should be able to avoid the shortcomings of Madjeski's and Geiger & Poirier's solutions.

1.5 Strategy

The preceding introduction, classification, and discussion of the published models represents the first step towards new understanding of the problem. Predictions from select previously published models will be compared to experimental data. Modifications and combinations of different authors' contributions will also be made, in order to formulate a new model, encompassing the best aspects of all types.

Experiments have been performed over a range of conditions wide enough to test model versatility. Standard metallic materials, with well-known physical properties, are used in

experiments conducted at MIT. Familiar materials as well as a new glass-forming alloy are also used at the Marshall Space Flight Center, under very different conditions. Others' data, when reported in the literature, has been included to supplement the range of conditions. Table 4 lists sources of transient experimental data, whether used to evaluate the model developed here or not.

Source	Material	Size	Velocity	Re	We
New	Co, Ni	5-8 mm	1.7 m/s	20,000	80
New	Ni	7.6 mm	44 m/s	4.8×10^5	66,000
Chandra & Avedisian	$n\text{-}C_7H_{16}$			2,300	43
Savic & Boult	H_2O	4.8 mm	6 m/s	30,000	2,300
Fukanuma & Ohmori	Sn, Zn			30,000	400
Watanabe et al.	$n\text{-}C_{16}H_{34}$, $n\text{-}C_{20}H_{42}$	3.5 mm	1.7 - 4.3 m/s	$10^3\text{-}10^4$	
Shi	H_2O	2-5 mm	1 - 3 m/s	2,775-15,844	33.9-582
Fukai	H_2O	1.9 mm	1.5 - 3.7 m/s	3,000-9,000	56-364

Table 4: Transient Splat Data

CHAPTER 2 - MODELS

2.1 Physical Properties

During flight or while spreading after impact, the metal cools, and its thermophysical properties change. Estimation of these values is a necessary step in any model. Simple equations for density, surface tension, and viscosity near the melting point were used when possible.[38] Thermal conductivities were calculated from the Wiedemann-Franz Law and the temperature dependence of the electrical resistivity.[39] Heat capacities and emissivities are approximated as constants.[40]

$$\rho = \rho_m + \frac{d\rho}{dT}(T - T_m) \qquad [31]$$

$$\sigma = \sigma_m + \frac{d\sigma}{dT}(T - T_m) \qquad [32]$$

$$\mu = \mu_0 \exp\left(\frac{E}{R_g T}\right) \qquad [33]$$

$$k = C\sigma_e T = C\left(\frac{1}{\alpha_e T + \beta_e}\right)T \qquad [34]$$

$$c_p \approx c_{pm} \qquad [35]$$

$$\varepsilon = 0.2 \qquad [36]$$

R_g and C are constants, 8.314 J/mol K and 2.45×10^{-8} WΩ/K^2, respectively; all other parameters are material properties. For pure materials, these values are tabulated.[38-40] For $Zr_{11}Ti_{34}Cu_{47}Ni_8$, no true melting *point* exists, so the liquidus temperature is used. The density and surface tension parameters are estimated from weighted averages of the values for the component elements. Characteristic of a glass-former, the viscosity has a very strong temperature dependence. Equation 33 is fit to the points: (T=648 K, $\mu=10^{13}$ P) and (T=1108 K, $\mu=1$ P).[41] One experimental thermal conductivity value was also available,[42] so it was assumed constant. Tables 5a and 5b show all of the parametric values for use with equations 31-34.

Metal	T_m [K]	h_f [J/kg]	ρ_m [kg/m^3]	$d\rho/dT$ [kg/m^3 K]	σ_m [N/m]	$d\sigma/dT$ [N/m K]
Co	1766	2.75×10^5	7750	-1.09	1.873	-4.9×10^{-4}
Ni	1727	2.93×10^5	7900	-1.19	1.778	-3.8×10^{-4}
$Zr_{11}Ti_{34}Cu_{47}Ni_8$	1153	x	6355	-0.5803	1.478	-2.5×10^{-3}

Table 5a: Physical Property Data

Metal	μ_0 [Pa s]	E [kJ/mol]	c_p [J/kg K]	α [$\mu\Omega$ cm/K]	β [$\mu\Omega$ cm]
Co	2.55×10^{-4}	44400	685	0.0612	-6
Ni	1.663×10^{-4}	50200	656	0.0127	63
$Zr_{11}Ti_{34}Cu_{47}Ni_8$	4.864×10^{-19}	3.88×10^5	575	x	x

Table 5b: Physical Property Data

2.2 Free-Fall Model

Before simulation of the actual droplet spreading begins, it is necessary to predict the conditions at impact, some time after releasing the droplet. This free-fall model permits calculation of these conditions for any combination of droplet material and surrounding gas, provided the appropriate physical properties are known or estimated. The model theory is generally applicable - to free-falling droplets as well as to those accelerated and melted by injection into plasma.

Knowing the initial droplet size and temperature, calculations reveal the force acting on the droplet, and its rate of heat loss to the surroundings. After a small time step, the momentum, temperature, and their rates of change are re-evaluated. The process is repeated at each of many small time steps, integrating the free-fall differential equations in an Runge-Kutta[43] fashion, until the droplet has hit the substrate.

Initially, the droplet accelerates in response to gravity alone. Except under vacuum conditions, drag forces will counteract this acceleration. Heat transfer occurs through radiation and through convection, if there is gas present. The Ranz-Marshall Equation,

$$\frac{h_g D_d}{k_g} = 2 + 0.6 \mathrm{Re}_g^{1/2} \mathrm{Pr}_g^{1/3} \qquad [37]$$

is used to calculate the heat transfer coefficient for a sphere falling through a fluid. h_g is the convective heat transfer coefficient, and D_d is the diameter of the sphere. k_g, Re_g, and Pr_g are the thermal conductivity, Reynolds Number and Prandtl number using gas properties.

A lumped capacitance energy balance is utilized, and a modified Biot Number,

$$\mathrm{Bi} = \frac{h_g D_d + \mathcal{E} \sigma_{sb} D_d T^3}{k} \qquad [38]$$

is calculated to check that this approach is warranted. The largest observed Biot Number values are still within the realm of lumped capacitance validity. σ_{sb} is the Stefan-Boltzman Constant, 5.678×10^{-8} W/m^{2}K^4.

The drag coefficient is evaluated according to the formula[44] :

$$C_d = 0.28 + 6 \mathrm{Re}_g^{-1/2} + 21 \mathrm{Re}_g^{-1} \qquad [39]$$

This free-fall model is very similar to Rolland's[35] and Jones'[10], except that radiation is considered in addition to convection because of the high melting temperatures of metals used. The Matlab™ code, "freefall.m," is included in Appendix 1.

2.3 Analytic Spreading Model

The analytic spreading model consists of two parts: an integral energy balance and a net force - due to surface tension and viscous effects - which acts upon the splat periphery, changing the spreading rate with time. First the energy balance and force are formulated from the assumed system geometry and velocity distribution for the all-liquid case. Then complicating heat transfer aspects are incorporated to examine the effects of solidification upon splat behavior. The equations obtained are non-dimensionalized for general use. A limiting case is discussed, and the calculational procedure is outlined.

2.3.1 Energy Balance

As stated in section 1.4.3, in the most general case, the spherical incident droplet has kinetic, surface, and gravitational energies, E_{kd}, E_{sd}, and E_{gd}, respectively. E_{gd} is generally neglected, and some authors do not consider E_{sd} either. To investigate these assumptions and justify neglecting either term, a comparison of the values of these terms is necessary.

The kinetic energy of the incident droplet,

$$E_{kd} = \frac{m v^2}{2} = \frac{2\pi\rho R_d^3 v^2}{3} \qquad [40]$$

is clearly the largest of the three terms considered. The surface energy of a spherical droplet is just the surface tension times the surface area:

$$E_{sd} = 4\pi\sigma R_d^2 \qquad [41]$$

The gravitational potential energy stored in holding a liquid sphere of radius R_d above some reference height in a gravity field with acceleration g is:

$$E_{gd} = 2\int_0^{R_d} \rho g \pi (R_d^2 - z^2) z \, dz = \frac{\pi\rho g R_d^4}{2} \qquad [42]$$

The ratios of these terms,

$$\frac{E_{sd}}{E_{kd}} = \frac{12\sigma}{\rho v^2 R_d} = \frac{12}{We} \qquad [43]$$

and

$$\frac{E_{gd}}{E_{kd}} = \frac{3g R_d}{4 v^2} = \frac{3}{8Fr} \qquad [44]$$

give an indication of the importance of surface tension and gravity, relative to kinetic energy. For typical plasma spraying and spray forming conditions, both the Weber and Froude Numbers are much larger than unity, indicating that these effects are indeed negligible. For typical MIT experimental conditions, We≈100 and Fr≈40, resulting in surface and gravitational energies of approximately 10% and 1% of the initial kinetic

energy. Gravitational effects are still quite minor, but the surface energy of the droplet needs to be considered.

The splat has similar terms, E_k and E_{sfc}, plus a term, L_f, to account for the cumulative losses to viscous friction. All of these factors depend on geometry and/or the velocity field within the splat. E_{sfc} and L_f manifest themselves by exerting effective forces on the splat, which alter its spreading rate and kinetic energy as time proceeds. The surface tension force will always act towards the state of lowest surface energy; the viscous force will always oppose motion. Splat surface energy as a function of splat geometry is first considered, then kinetic energy and viscous losses as functions of the velocity distribution.

2.3.2 Surface Energy

In section 1.4.2, potential values for initial cylinder dimensions were discussed. To obtain a splat surface area nearest to that of the incident droplet, an initial radius,

$$R_0 = \sqrt[3]{\frac{2}{3}} \approx 0.8736 \qquad [45]$$

is used. The surface energy of the splat, like that of the droplet, is simply the product of its surface area - given in equation 23 - and the surface tension of the metal. Equation 22 is valid for the liquid thickness at later times too, so substitution yields:

$$E_{sfc} = \sigma \left(2\pi R^2 + \frac{8\pi R_d^3}{3R} \right) \qquad [46]$$

2.3.3 Kinetic Energy

The kinetic energy of the incident droplet is given in equation 40 as one-half the product of mass and the square of velocity. Using the same approach in terms of the spreading rate of the splat gives

$$E_k = \frac{2\pi \rho R_d^3}{3} \left(\frac{dR}{dt} \right)^2 \qquad [47]$$

2.3.4 Viscous Losses

The exact value of the viscous losses in any spreading process will depend on case-specific conditions because of path dependence. Some authors[10,45] approximate these losses as classic, theoretical problems such as the deformation of cylinders between parallel plates. Others[1] use simple order-of-magnitude estimates. While reasonable for asymptotic solutions, these approaches are of little value for transient modeling. Other authors[12,24] evaluate a viscous dissipation rate that depends on the transient splat geometry and the velocity field. For a Newtonian fluid in laminar flow, the rate of viscous energy dissipation can be approximated as

$$\frac{dL_f}{dt} = 2\pi \int_0^R \overline{\tau}\,\overline{v_r}\,r\,dr \qquad [48]$$

where $\overline{\tau}$ is shear stress,

$$\overline{\tau} = \mu \frac{dv_r}{dz} \qquad [49]$$

and $\overline{v_r}$ is average radial velocity.

$$\overline{v_r} = \frac{1}{b}\int_0^b v_r\,dz \qquad [50]$$

With Madjeski's velocity field assumption,

$$v_z = -Cz^2 \qquad [51]$$

$$v_r = Czr \qquad [52]$$

shown in Figure 4, the rate of viscous dissipation equals:

$$\frac{dL_f}{dt} = \frac{3\pi\mu R^4}{4 R_d^3}\left(\frac{dR}{dt}\right)^2 \qquad [53]$$
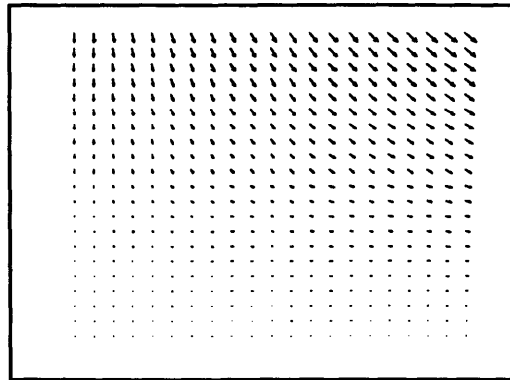
Figure 4: Madjeski Velocity Profile

To obtain the total energy lost to viscous dissipation up through time t, equation 53 is integrated:

$$L_f = \int_0^t \frac{dL_f}{dt}dt = \frac{3\pi\mu}{4R_d^3}\int_0^t R^4\left(\frac{dR}{dt}\right)^2 dt \qquad [54]$$

2.3.5 Splat Force Calculation

The net force on the splat during spreading is due to the combined effects of surface energy and viscosity. The surface tension force, F_{sfc}, equals the negative derivative of surface energy with respect to radius. From equation 46,

$$F_{sfc} = \frac{-dE_{sfc}}{dR} = -\pi\sigma\left(4R - \frac{8R_d^3}{3R^2}\right) \qquad [55]$$

F_{sfc} is proportional to the displacement from equilibrium, and it will be directed towards the state of lowest surface energy. The viscous force, F_v, is found by dividing the viscous dissipation rate by the spreading rate, just as force equals power divided by velocity.

$$F_v = \frac{-\left(\dfrac{dL_f}{dt}\right)}{\left(\dfrac{dR}{dt}\right)} = \frac{-3\pi\mu\,R^4}{4R_d^3}\left(\frac{dR}{dt}\right) \qquad [56]$$

F_v is proportional to the spreading rate, and will always oppose motion.

The splat acceleration, a, is the derivative of its spreading rate This acceleration is proportional to the sum of these forces.

$$a = \frac{d^2R}{dt^2} = \frac{F_{sfc} + F_v}{m} \qquad [57]$$

The proportionality constant is the mass, m, of the liquid, given by:

$$m = \frac{4\pi\rho\,R_d^3}{3} \qquad [58]$$

Combination of equations 55-58 gives

$$\frac{d^2R}{dt^2} = \frac{-3\sigma R}{\rho R_d^3} + \frac{2\sigma}{\rho R^2} - \frac{9\mu R^4}{16R_d^6}\left(\frac{dR}{dt}\right) \qquad [59]$$

2.3.6 Non-Dimensionalization

To make equation 59 more general and more mathematically tractable, dimensionless variables are introduced. These are the same quantities defined in section 1.2.4 and used in the technical literature.

$$\tau = \frac{vt}{2R_d} = \text{Dimensionless Time} \qquad [6]$$

$$\xi = \frac{R}{R_d} = \text{Dimensionless Radius; Spreading Extent} \qquad [7]$$

$$\beta = \frac{b}{2R_d} = \text{Dimensionless Liquid Height} \qquad [8]$$

The equivalent statement of equation 59 in term of these variables is:

$$\frac{d^2\xi}{d\tau^2} = \frac{-24\xi}{We} + \frac{16}{We\,\xi^2} - \frac{9\xi^4}{4\,Re}\left(\frac{d\xi}{d\tau}\right) \qquad [60]$$

With an initial spreading rate determined in the next section, the transient behavior of a liquid splat may now be calculated by integrating equation 59, subject to the initial conditions specified for ξ and $d\xi/d\tau$.

Three more dimensionless quantities prove useful in tracking the distribution of energy between its various forms. Dimensionless kinetic and surface energies, and viscous losses, ε_k, ε_{sfc}, l_f, respectively, can be defined in terms of these same dimensionless variables and numbers:

$$\varepsilon_k = \frac{E_k}{E_{kd} + E_{sd}} = \frac{\left(\dfrac{d\xi}{d\tau}\right)^2}{4 + \dfrac{48}{We}} \qquad [61]$$

$$\varepsilon_{sfc} = \frac{E_{sfc}}{E_{kd} + E_{sd}} = \frac{2\xi^2 + \dfrac{8}{3\xi}}{\dfrac{We}{3} + 4} \qquad [62]$$

$$l_f = \frac{L_f}{E_{kd} + E_{sd}} = \frac{\int\limits_{\tau'=0}^{\tau'=\tau} \xi^4 \left(\frac{d\xi}{d\tau}\right)^2 d\tau'}{\dfrac{8\,Re}{9} + \dfrac{32\,Re}{3\,We}} \qquad [63]$$

2.3.7 Initial Conditions

Time zero is taken as the instant when the droplet first hits the substrate. From a modeling point of view, the system consists of the initial cylinder, moving outwards at some initial spreading rate. Viscous losses are assumed to be zero at this point, so that the initial spreading rate can be found from an integral energy balance.

$$\frac{d\xi}{d\tau}\bigg|_0 = \sqrt{4 + \frac{48}{We} - \frac{12\,\xi_0^2}{We} - \frac{32}{We\,\xi_0}} \qquad [64]$$

2.3.8 Limiting Case

One interesting limiting case can be solved without integrating equation 60. When viscous losses are negligible, an upper bound on the spreading extent can be found by balancing the droplet's initial energy with the splat surface energy. In this case, $\varepsilon_{sfc}=1$, so equation 62 can be solved for the limiting spreading extent, ξ_{lim}:

$$2\,\xi_{lim}^2 + \frac{8}{3\,\xi_{lim}} = \frac{We}{3} + 4 \qquad [65]$$

A plot of ξ_{lim} versus We is included as Figure 5.

2.3.9 Solid Growth

Solidification changes nearly every aspect of the spreading process. It was excluded from the initial derivation for the sake of simplicity. In section 1.4.4, the heat flux is expressed in terms of the temperature driving force and the four thermal resistances, and the solidification velocity is related to the heat flux. Equations 26 and 27 are combined and non-dimensionalized with the following variables:

40
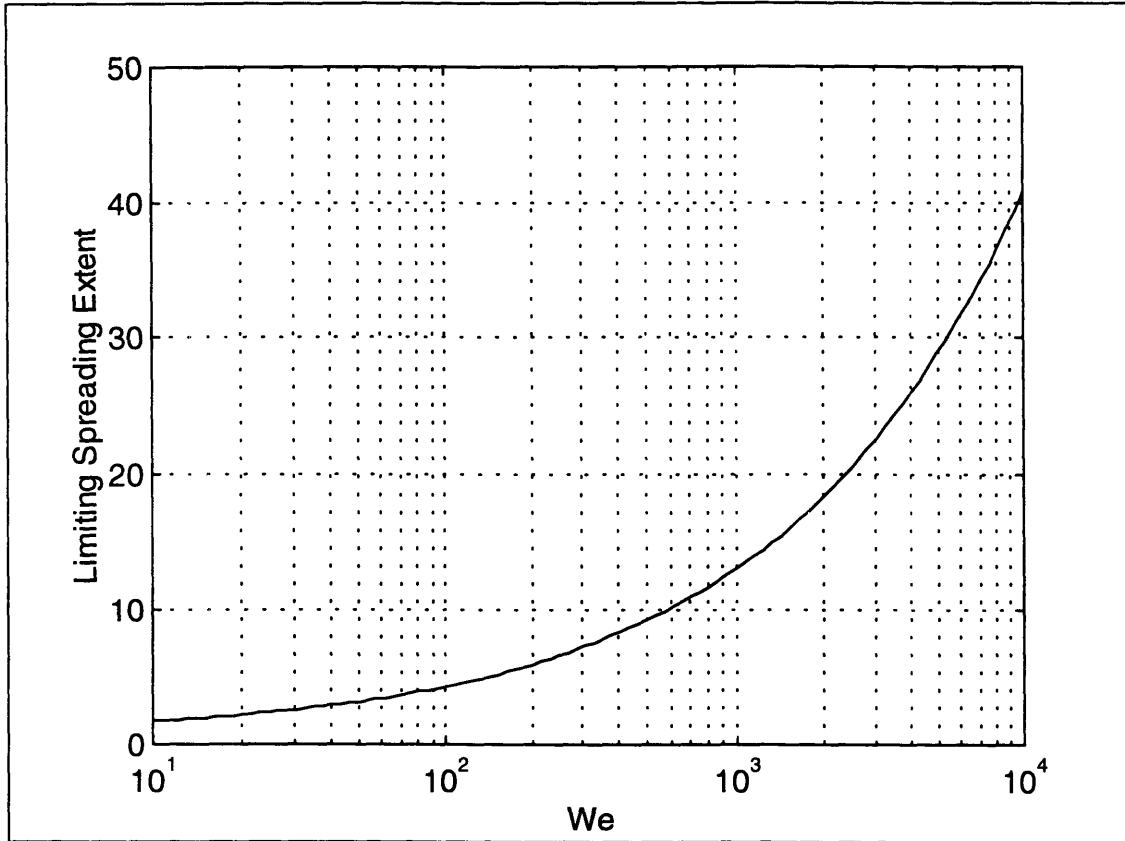
Figure 5: ξ_{lim} vs. We

$$Z = \frac{z_s}{2R_d} = \text{Dimensionless Solid Thickness} \qquad [9]$$

$$N_1 = h\sqrt{\frac{\pi t}{k\rho c_p}} = \frac{\text{Liquid Resistance}}{\text{Interface Resistance}} \qquad [66]$$

$$N_2 = \frac{h z_s}{k} = \frac{\text{Solid Resistance}}{\text{Interface Resistance}} \qquad [67]$$

$$N_3 = h\sqrt{\frac{\pi t}{k'\rho' c_p'}} = \frac{\text{Substrate Resistance}}{\text{Interface Resistance}} \qquad [68]$$

$$N_4 = \frac{h(T_d - T_s)}{\rho h_f v} = \frac{\text{Freezing Velocity}}{\text{Heat Flux}} \qquad [69]$$

$$N_5 = \frac{T_m - T_s}{T_d - T_s} = \text{Dimensionless Temperature Difference} \qquad [70]$$

41

$$Q = \frac{q}{h(T_d - T_s)} = \frac{\text{Heat Flux}}{\text{Maximum Heat Flux}}$$ [71]

The dimensionless solid growth equation is:

$$\frac{dZ}{d\tau} = N_4 Q = \frac{N_4}{(N_1 + 1 + N_3)}$$ [72]

before solidification begins, and

$$\frac{dZ}{d\tau} = N_4 N_5 Q = \frac{N_4 N_5}{(N_2 + 1 + N_3)}$$ [73]

after it has. With these dimensionless parameters specified. the thickness of the solid layer is found by integrating equations 72 and 73.

The time-dependent solid fraction, f_s, is related to the total solid volume, V_s, which can be found by integrating z_s over the total spatial extent of spreading. The solidification front moves out from the initial radius in small radial steps, and upwards in small axial increments, so that the solid will grow in thin concentric rings, much like a terraced mountain. integration of the volumes of these regions will give V_s.

$$V_s\{t\} = \pi R^2 z_s\{R_0, t - t_s\} - \int_0^R z_s\{r, t - t_s\} 2\pi r \, dr$$ [74]

This integral is challenging to evaluate because z_s depends on both time and position. It can be simplified by re-writing in terms of the local solidification time, t_r, which equals the time elapsed in-between the commencement of solidification at a position, and the present time. This transformation converts z_s from a function of both r and t to one of t_r only. The solid volume becomes:

$$V_s\{t\} = \pi R_0^2 z_s\{t - t_s\} + 2\pi \int_{t_r = t_s}^{t_r = t} z_s\{t_r\} R\{t - t_r\} \frac{dR}{dt}\{t - t_r\} d t_r$$ [75]

and its derivative equals:

$$\frac{dV_s}{dt}\{t\} = \pi R_0^2 \frac{d z_s}{dt}\{t - t_s\} + 2\pi \int_{t_r = t_s}^{t_r = t} \frac{d z_s}{dt}\{t_r\} R\{t - t_r\} \frac{dR}{dt}\{t - t_r\} d t_r$$ [76]

V_s and f_s are related by:

$$f_s = \frac{3\rho' V_s}{4\pi R_d^3 \rho} = \frac{\text{Solid Volume}}{\text{Fully Solid Volume}}$$ [77]

When equations 6, 7, 9, 76, and 77 are combined, the dimensionless solidification rate can be found:

$$\frac{df_s}{d\tau} = \frac{3\rho'}{2\rho}\left(\xi_0^2\frac{dZ}{dt}\{\tau-\tau_s\} + 2\int_{\tau_r=\tau_s}^{\tau_r=\tau}\frac{dZ}{d\tau}\{\tau_r\}\xi\{\tau-\tau_r\}\frac{d\xi}{d\tau}\{\tau-\tau_r\}d\tau_r\right)$$ [78]

If flow reversal occurs, and the liquid rolls back over previously-formed solid, equation 78 gets even more complex. Solid continues to grow where liquid still covers it, but not elsewhere. This consideration is included in the program source code, so that the splat may be modeled up until a second reversal occurs. Further simulation becomes mathematically challenging.

2.3.10 Solidification Effects

The first change due to solidification is the inclusion of a new term in the energy balance. As solid grows into the spreading splat, kinetic energy is lost as moving liquid freezes into stationary solid. This solidification loss, E_{sol}, can be quantified by considering an element of mass dm, moving at velocity v. As it freezes, it loses its kinetic energy, $v^2 dm/2$. In the splat, v is the spreading rate, dR/dt, and dm can be correlated to f_s.

$$dm = \frac{-4\pi\rho R_d^3}{3}df_s$$ [79]

The solidification losses need to be integrated as f_s changes,

$$E_{sol} = \int_{f_s'=0}^{f_s'=f_s}\frac{2\pi\rho R_d^3}{3}\left(\frac{dR}{dt}\right)^2 df_s'$$ [80]

or they can be equivalently expressed as a time integral:

$$E_{sol} = \int_{t'=0}^{t'=t}\frac{2\pi\rho R_d^3}{3}\left(\frac{dR}{dt}\right)^2\left(\frac{df_s}{dt}\right)dt'$$ [81]

In dimensionless form,

$$\varepsilon_{sol} = \frac{\int_{\tau'=0}^{\tau'=\tau}\left(\frac{d\xi}{d\tau}\right)^2\left(\frac{df_s}{d\tau}\right)d\tau'}{4+\frac{48}{We}}$$ [82]

43

Solidification also affects the surface energy of the splat. As metal freezes from the bottom upwards, and the center outwards, the splat acquires a lens shape. This curvature creates more surface area than a flat splat would have, so equation 46 must be modified to account for this solidification-induced liquid surface energy. Including the vertical side area of the concentric solid rings adds a term:

$$E_s = \sigma\left(2\pi R^2 + \frac{8\pi R_d^3}{3R} + 2\pi\int_{z'=0}^{z'=z_s} R\{z'\}dz'\right) \tag{83}$$

This integral, too, can be re-written in terms of the local solidification time, t_r.

$$E_s = \sigma\left(2\pi R^2 + \frac{8\pi R_d^3}{3R} + 2\pi\int_{t_r=t_s}^{t_r=t} R\{t-t_r\}\frac{dz_s}{dt}\{t_r\}dt_r\right) \tag{84}$$

With solid metal now present, there are also the possibilities of solid-vapor and solid-liquid interfacial energies. The solid-vapor interface is assumed to have the same surface energy as the liquid-vapor interface, and the latter effect is neglected.

The last effect of solidification is on the kinetic energy and viscous losses in the splat. The liquid thickness now decreases as freezing proceeds, so equations 22, 47, and 54 have to be modified.

$$b = \frac{4R_d^3(1-f_s)}{3R_0^2} \tag{85}$$

$$E_k = \frac{2\pi\rho R_d^3(1-f_s)}{3}\left(\frac{dR}{dt}\right)^2 \tag{86}$$

$$\frac{dL_f}{dt} = \frac{3\pi\mu R^4}{4R_d^3(1-f_s)}\left(\frac{dR}{dt}\right)^2 \tag{87}$$

With these revisions to the energy terms, new forces and a new acceleration can be found.

$$F_{sfc} = \frac{-dE_{sfc}}{dR} = -\pi\sigma\left(4R - \frac{8R_d^3(1-f_s)}{3R^2} + 2z_s\{t-t_s\}\right) \tag{88}$$

$$F_v = \frac{-\left(\dfrac{dL_f}{dt}\right)}{\left(\dfrac{dR}{dt}\right)} = \frac{-3\pi\mu R^4}{4R_d^3(1-f_s)}\left(\frac{dR}{dt}\right) \tag{89}$$

44

$$\frac{d^2 R}{dt^2} = \frac{-3\sigma R}{\rho R_d^3(1-f_s)} + \frac{2\sigma}{\rho R^2} - \frac{3z_s\{t-t_s\}}{2\rho R_d^3(1-f_s)} - \frac{9\mu R^4}{16 R_d^6(1-f_s)^2}\left(\frac{dR}{dt}\right)$$

[90]

$$\frac{d^2\xi}{d\tau^2} = \frac{-24\xi}{We(1-f_s)} + \frac{16}{We\,\xi^2} - \frac{24Z\{\tau-\tau_s\}}{We(1-f_s)}\frac{9\xi^4}{4\mathrm{Re}(1-f_s)^2}\left(\frac{d\xi}{d\tau}\right)$$

[91]

The new energy term, E_{sol}, does not exert a separate force on the droplet, but rather the other forces change with the new $(1-f_s)$ factor. E_{sol} merely accounts for the energy associated with these changes.

2.3.11 Solid Exposure

The final complicating factor to be considered when adding solidification is that of solid exposure. The first term of equation 84 is written as $2\pi R^2$, but it will change if liquid flow reversal has exposed any solid. The area will actually be $2\pi R_s^2$ if R_s, the solid spreading extent, is greater than R. Since this quantity does not depend on R, it drops out of the derivative in equation 88, so that the first term in both equations 90 and 91 will vanish. This change removes a potentially large inward-directed force and modifies the equilibrium state towards which the surface tension force pulls the splat.

One interesting result of this model set-up is that flow reversal is not possible for droplets with no solidification delay. The strong inward-directed force, relating to the splat's top and bottom surface energy, comes from the first term in equations 83, 84, 88, 90, and 91. When there is no solidification delay, this term vanishes at the instant that flow stops. The remaining terms are smaller in magnitude, so they are generally damped out by viscosity.

This tendency can be illustrated by considering the surface energy to be a potential height and the splat to be a rolling ball. Viscous and solidification losses would be correspond to friction, gradually removing energy from the system. Before solid exposure occurs, the potential function, E_{sfc}, is given by equation 84. Afterwards, it would be the same, but with $2\pi R_s^2$ replacing $2\pi R^2$. These curves are depicted schematically in Figure 6. Before solid exposure, the E_{sfc}-R potential plot resembles a valley with an equilibrium minimum

energy position. The spreading process can be likened to releasing a ball with an initial velocity from a certain radius. As the ball rolls, or the splat spreads, its velocity and the force acting on it change. After ceasing to spread forward, a point, marked by the 'o,' is reached where solid exposure occurs. Now the E_{sfc}-R potential plot is shown in Figure 6b. After this time, the surface energy cannot drop below the solid horizontal line because R_s is fixed. E_{sfc} rises continuously as R shrinks - slowly at first, then sharply. It also rises to the right, but the droplet is no longer spreading outwards. In the case of instant solidification, the droplet velocity here will be zero, so it will reside at this new equilibrium position. In the case of a finite solidification delay, the ball would continue rolling to the left, but it would slow gradually and finally come to a stop.
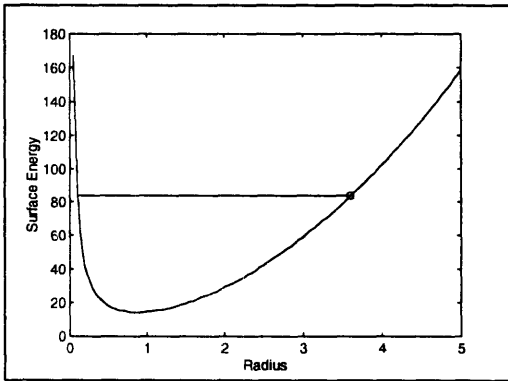
**Figure 6a: Surface Potential
Before Solid Exposure**
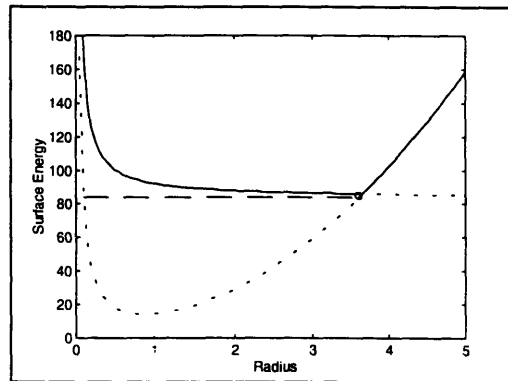
**Figure 6b: Surface Potential
After Solid Exposure**

2.3.12 Calculational Procedure

Equations 61-64, 72, 73, 78, 82, and 91, together with the dimensionless variable definitions, form the basis for the mathematical model of non-isothermal spreading and freezing of a molten metal droplet. At this point, some calculational procedure is necessary, except for the limiting cases described in section 2.3.8. Several Matlab™ programs were written for this purpose. "Begin.m" inputs the system data and thermophysical properties. "Freeze.m" determines the transient cooling behavior up to the start of solidification. "Splat.m" then calculates the transient spreading behavior. These models, despite appearing complex, are not all that computationally intensive. All calculations were done on a 33Mhz 486-DX personal computer, rather than a

workstation. Still, an average run took only a few minutes. Model results are presented in section 4. Appendix 1 contains the actual program code.

CHAPTER 3 - EXPERIMENTS

3.1 General Technique

The experimental technique used to obtain transient spreading data begins with the magnetic levitation and melting of single droplets. Millimeter-sized droplets were used, rather than the micron-sized particles characteristic of spray forming, to avoid observation and direct measurement problems. 5 to 8 mm sized particles can be weighed directly rather than having their sizes inferred from statistical distributions. Direct, single droplet pryrometric temperature measurement is also possible. Two separate experimental campaigns were conducted - one at MIT and one at NASA's Marshall Space Flight Center in Huntsville, Alabama.

3.2 MIT

Magnetic levitation and melting is accomplished with a Lepel Radio Frequency Generator, passing current through a coil, whose magnetic fields hold the droplet up against gravity and cause eddy currents, which resistively heat the sample. The surrounding atmosphere is controlled by passing gas over the sample and through the catch tank. Once molten, power to the coil is cut-off, causing the droplet to fall freely until it impacts the substrate. Following manual triggering, the spreading process is recorded via high speed digital photography. Subsequent image processing permits extraction of time-dependent dimensionless spreading variables (ξ and β), for comparison with model predictions.

3.2.1 Material Selection

In selecting materials for experimental use, a number of considerations were taken into account. Use of a commonly thermally sprayed alloy is desirable. The sample must also melt in the coil, as it is setup in the laboratory. This restriction excludes many refractory metals due to their melting points alone, as the coil cannot supply energy sufficient to match radiative losses at these temperatures. In practice, this requirement also prevented the use of Copper because its conductivity is too high for adequate resistive heating.

Silver is expected to behave similarly, so it was not tried. Aluminum also did not melt in the coil because its low density made it levitate farther out of the most intense magnetic fields.

Another practical material requirement is that no extravagant anti-oxidation measures should be necessary. Surface oxide can interfere with the spreading process, and significantly affect the surface tension of the droplet. This problem has been singled out as a source of past model-experiment disagreement.[10] Consequently, highly reactive metals such as Titanium, Zirconium, Aluminum, and Magnesium had to be excluded as well.

Due to laboratory health concerns, overly toxic materials were not used either. Heavy metals, carcinogenic metals, and/or metals with high vapor pressures, such as Mercury, Lead, Bismuth, Cadmium, Zinc, Chromium, and Beryllium were not considered. Finally, whatever materials were used needed to have melting points in the temperature range measurable by two-color pyrometry at 0.81 and 0.95 µm, so low-melters such as Aluminum, Zinc, and Tin could not be used. The only common metals meeting all of these requirements are Iron, Cobalt, and Nickel, so these three metals were used. Experimental data is presented below for Cobalt and Nickel samples of 99% purity.

3.2.2 Apparatus

The Lepel generated current at 100-200 kHz. The coil was made of Copper wire, wrapped around a test tube of 15mm outside diameter. Quartz tubing of the same diameter was placed inside the coil to provide sample containment and isolation. Gas flow over the sample was made possible by flexible tubing connected to the quartz tube top above the coil. A mixture of Helium and 4% Hydrogen was used to provide a mildly reducing atmosphere and to control droplet temperature via convective cooling. Argon, with its density greater than that of air, was also used to flush the catch tank in-between runs.

The catch tank consisted of a glass cylinder over which a tight-fitting plexi-glass cover was placed. This cover had been machined to accomodate sample and gas inlets. The substrates, 1.6 mm thick Copper plates - sanded and polished before each set of runs - were placed at the bottom of the catch tank, 10cm from the cover. Glass was also tried, because of reports of higher heat transfer coefficients[32], but it always cracked catastrophically. Figure 7 shows the experimental set-up schematically.
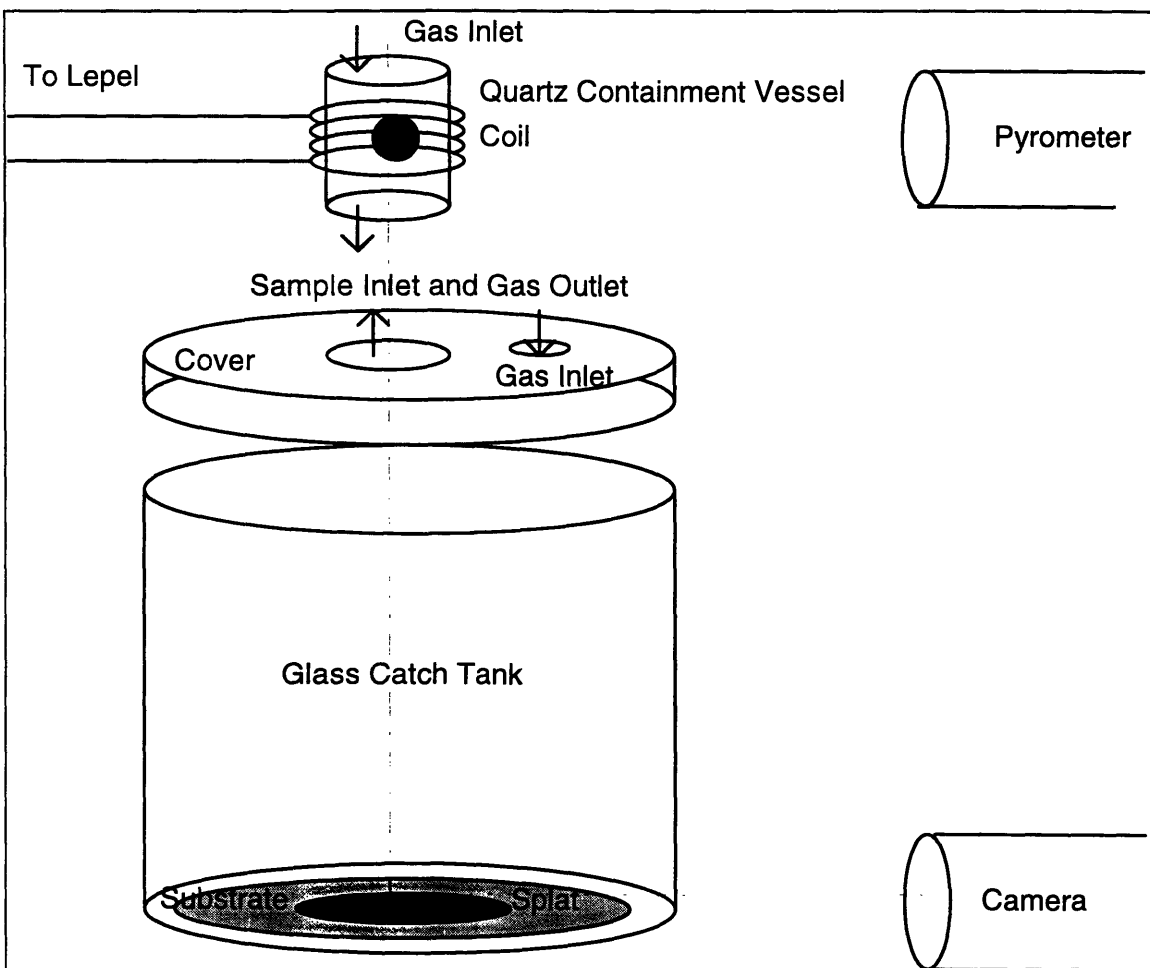
Figure 7: Schematic Experimental Setup

A Kodak EKTAPRO Motion Analyzer with a 200 mm lens was used to record digital high speed photographic images of the spreading and freezing process. The frame rate is variable from 30 to 40,500 per second, but most experiments were performed in the range from 4,500 to 18,000. The frame rates used, along with the field of view, and the number of images are listed in Table 6.

Frame Rate [#/sec.]	Field of View, Horizontal x Vertical, [Pixels]	Number of Images
4,500	256 x 256	1024
9,000	256 x 128	2048
18,000	256 x 64	4096

Table 6: Camera Settings

One benefit of working with Iron, Cobalt, and Nickel is that the melting points of these elements are high enough so that they give off ample light for photography. No external lighting was necessary to photograph the spreading process, so that no measures had to be taken to avoid specular refelctions. In fact, the camera was f-stopped down to f/32 to avoid over-exposure and saturation.

3.2.3 Procedure

For each experimental run, the sample was melt-processed once to before dropping to clean off surface oxide. It was then weighed and stored until use. Just prior to re-melting, all samples were dipped in an etching solution of $FeCl_3$, HCl, and H_2O to remove oxide once more, then rinsed in ethanol to remove organic contaminants. The quartz tube and catch tank were purged, and then the sample was insered into the coil by placing it on the end of a clean alumina rod. Coil power was turned on, and the sample would levitate, heat, and melt. Immediately after sample insertion, the substrate was positioned by cranking it up to a pre-set position of known height, upon which the camera had been focused. When the pyrometer indicated that the the droplet had passed through the melt plateau, the gas flowrate was adjusted to give the proper release temperature, and then the coil power shut off. Manual triggering was sufficiently accurate because of the low impact speeds.

Images were downloaded after each successful run: one as soon as the falling droplet was visible, one immediately prior to impact, and then many during spreading. The splats were removed from the substrate and saved. The substrate was then be cleared of any debris, and re-flushed for the next run.

51

Image processing was accomplished using a custom-written IPLab™ script. Automatic segmentation (cut off at a specified pixel intensity) was used to ensure consistent splat boundary definition. For each experiment, a representative image was used to set the segmentation threshold. Then each image was loaded, segmented, and measured manually. The resulting data were saved for comparison with model predictions. An average diameter and a correction factor were calculated for out-of-round droplets.

3.3 Marshall Space Flight Center

Similar levitation melting was performed at the top of the Marshall Space Flight Center drop tube, which is entirely atmosphere-controlled. No gas is forced over the levitating droplet, but the shaft can be evacuated or back-filled with the same gases. Following release, the droplet falls for several seconds and acquires a speed such that manual triggering is no longer adequate. Instead, an optical interruption-based trigger was used to start the camera a short time after the droplet was detected.

The Marshall setup is much less limiting regarding material selection. Nickel, Copper, Titanium, Nickel-Niobium and Nickel-Zirconium binary alloys, and the $Zr_{11}Ti_{34}Cu_{47}Ni_8$ glass-forming alloy were all melted and dropped. Because of the greater cooling that occurs during longer free fall times, and the lower melting points of some of the materials used, external lighting was necessary to photograph the spreading process.

A Hadland Photonics Imacon 486 camera was used in the Marshall experiments. It is capable of much higher effective frame rates (10ns interframe time limit), but it can only provide eight images of any one event - resulting in a shorter recording duration for each splat. Greater free-fall heights result in more uncertainty in the droplet's final speed, as well as an increased tendency for it to be out of the camera's field of view. The combination of these three factors reduces the number of successfully recorded splat events from the Marshall experiments.

CHAPTER 4 - RESULTS

4.1 Overview

The results of the two sets of experiments, described in chapter 3, will be presented in turn - first MIT then the Marshall Space Flight Center. For each set, recorded data and model predictions will be presented in tandem. Measured release conditions, free fall model output, impact conditions, spreading model output, and spreading observations will be presented in this order. Analysis, discussion, and conclusions will follow in Chapter 5.

4.2 MIT

The experiments conducted at MIT with Cobalt and Nickel samples are characterized by 5-8mm droplet diameters, a 15cm free fall, and impact onto a Copper plate. Eleven runs were done in total. Table 7 shows the release conditions for each.

ID#	Material	Mass [g]	Diameter at Release [mm]	Temperature at Release [K]	Height [cm]
319_1	Co	1.997	7.95	1901	15.5
319_2	Ni	1.721	7.49	1782	15.5
319_3	Ni	2.347	8.33	1840	15
319_4	Ni	2.224	8.17	1817	15.5
321_1	Ni	1.535	7.27	1958	14.4
328_1	Ni	1.159	6.56	1766	14.4
328_2	Ni	1.219	6.72	1909	14.4
329_3	Co	0.641	5.44	1919	14.4
329_4	Co	0.652	5.47	1899	14.4
329_5	Co	0.790	5.82	1854	14.4
329_6	Co	1.790	7.64	1846	14.4

Table 7: MIT Experimental Release Conditions

4.2.1 Free Fall Model Output

Figure 8 shows sample velocity and temperature output from the free fall model for MIT experimental conditions. The calculation was performed for ID# 319_1, using "freefall.m," with a time step of 2×10^{-4} seconds - a value small enough that results were essentially insensitive to further reduction.
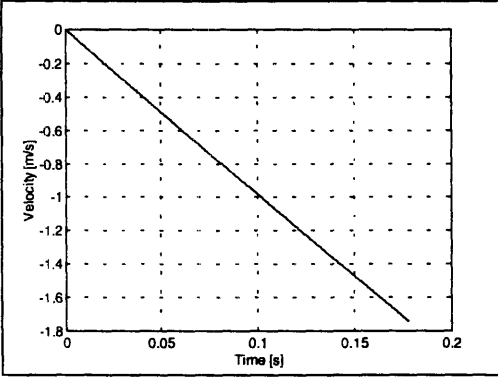
Figure 8a: Free-Fall Model Output MIT Experiment, Velocity Plot
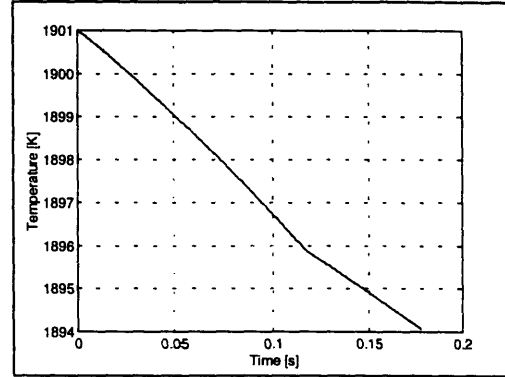
Figure 8b: Free-Fall Model Output MIT Experiment, Temperature Plot

From Figure 8a, it can be seen that drag does not significantly slow the falling droplet. Hence, its final velocity should be close to that for drag-free fall,

$$v_{max} = \sqrt{2gz} \qquad [92]$$

v_{max} equals -1.743 m/s in this case, revealing that the model is accurate. The temperature drops by a modest amount (7°) in the short time that the droplet is in flight. The change in slope of the temperature-time curve is due to the change in environment, when the droplet leaves the Helium/Hydrogen-flushed tube to enter the Argon-filled catch tank. Since Argon has a significantly lower thermal conductivity, convective losses decrease, and the droplet cools more slowly. A sharp transition in gas properties at a specific height is assumed. In addition, the low flowrate of gas over the droplet in the coil is neglected; the heat transfer coefficient is calculated assuming that the surrounding gas is stationary.

The relative importance of radiation versus convection can be seen in Figure 9, which plots the time-dependent heat flux ratio,

$$\frac{q_{rad}}{q_{conv}} = \frac{\varepsilon \sigma_{sb} T^4}{h_g (T - T_g)} \qquad [93]$$
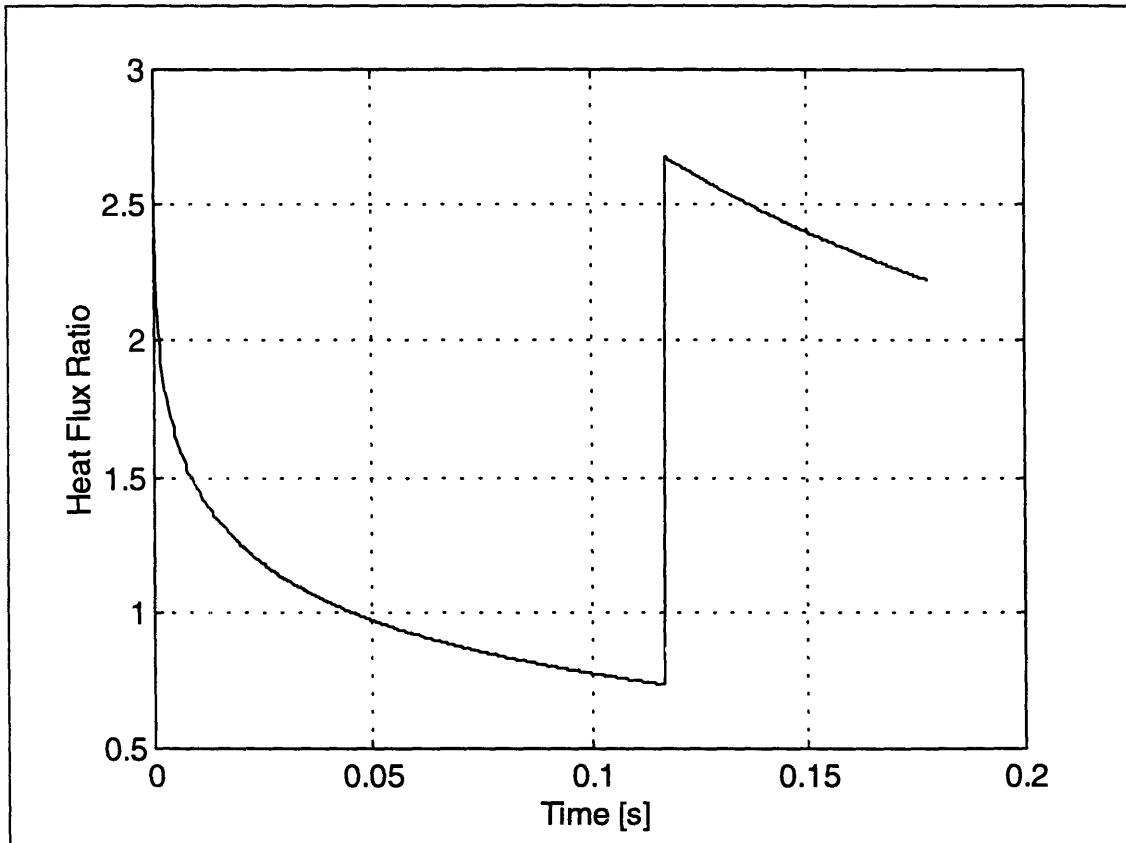
Figure 9: Radiative to Convective Heat Flux Ratio

Radiation is most important immediately after the droplet is released. As velocity increases, convection grows quickly until it causes more rapid cooling. When the droplet passes through the catch tank top height, the change in gas properties causes a discontinuity. Argon's low conductivity returns radiation to prime importance. By the time of impact, the total heat lost is nearly evenly split between these two effects: 54% radiative in this case.

Table 8 shows the free fall model output for each of the MIT experiments. Impact conditions are characterized in terms of the droplet velocity and temperature, as well as several important dimensionless numbers.

The freezing number, F, requires further explanation. In equation 21, F is expressed in terms of A_c, the contact area for heat extraction. Unfortunately, this is one of the very parameters that the spreading model will be used to predict. Proper evaluation of F

requires some knowledge of the flow regime upon impact. For the conditions here, where surface tension appears more important that viscosity (Re>>We), one of Madjeski's limiting solutions[12],

$$\xi = \sqrt{\frac{We}{3}}$$

[94]

can be used to evaluate A_c. This is actually what is proposed by Rolland.[35] With this assumption, the tabulated F values are found:

$$F = \frac{12\rho v\left(c_p(T_d - T_m) + h_f\right)}{Weh(T_d - T_s)}$$

[95]

ID#	Impact Velocity [m/s]	Impact Temperature [K]	Re	We	Fr	F
319_1	1.74	1894	24627	101	39	36
319_2	1.74	1776	20505	101	41	36
319_3	1.71	1834	24794	109	36	35
319_4	1.74	1811	23785	111	38	34
321_1	1.68	1950	25331	92	40	44
328_1	1.68	1759	16811	82	44	41
328_2	1.68	1901	21759	85	43	46
329_3	1.68	1908	16566	65	53	55
329_4	1.68	1889	16215	65	53	53
329_5	1.68	1845	16242	69	49	48
329_6	1.68	1840	21175	90	38	36

Table 8: MIT Experimental Impact Conditions

The dimensionless numbers are clustered around the values, $Re=2\times10^4$, $We=80$, $Fr=40$, and $F=40$. For these Froude numbers, gravitational effects are indeed small, so gravitational energy can be neglected, as justified in section 2.3.1. Weber numbers, on the other hand, are small enough that the droplet's initial surface energy does represent a significant fraction of the total system energy and should be considered. The freezing number values indicate that spreading will occur faster than freezing, but not disproportionately so.

4.2.2 Solidification Model Output

More insight into the heat transfer aspects can be gained by examining the dimensionless numbers comparing the thermal resistances. These values are shown in Table 9, for an assumed heat transfer coefficient of 10^4 W/m^2 K. The calculated solidification commencement times are also included.

ID#	$N_1/\tau^{0.5}$	N2/Z	$N_3/\tau^{0.5}$	N_4	N_5	τ_s
319_1	0.0808	1.871	0.0323	0.0044	0.9197	1.264
319_2	0.0719	0.8560	0.0313	0.0037	0.9668	0.237
319_3	0.0759	0.9520	0.0333	0.0039	0.9302	1.044
319_4	0.0748	0.9337	0.0327	0.0038	0.9444	0.655
321_1	0.0706	0.8309	0.0314	0.0044	0.8648	5.657
328_1	0.0686	0.7497	0.0298	0.0038	0.9781	0.110
328_2	0.0683	0.7680	0.0302	0.0042	0.8913	3.567
329_3	0.0681	1.280	0.0272	0.0046	0.9117	2.193
329_4	0.0681	1.287	0.0272	0.0045	0.9226	1.624
329_5	0.0700	1.369	0.0281	0.0044	0.9489	0.620
329_6	0.0802	1.780	0.0322	0.0044	0.9519	0.414

Table 9: MIT Experimental Heat Transfer Parameters

From table 9, the thermal resistances can finally be compared by examining N_1, N_2, and N_3 - the ratios of the liquid, solid, and substrate resistances to that of the interface. Liquid resistance is only considered up until τ_s. For the τ_s values listed, this results in N_1 values ranging from 0.02 to 0.17. For highly superheated droplets, the thermal resistance of the heat-affected zone in the liquid is clearly important. To evaluate N_2 and N_3, some values for τ and Z are needed. If most of the transient spreading behavior occurs before $\tau \approx 10$, and $Z \approx 0.05$, N_2 would be near 0.1, and N_3 would be near 0.3. All of the terms are less than unity, so the interface is still the largest single resistance. The other terms are significant, however - representing up to 30% of the interface resistance. Figure 10 plots the evolution of these ratios and the dimensionless heat flux, Q, for the conditions of experiment ID# 319_1. Figure 11 shows the growth of the solid thickness, and includes Madjeski's and Geiger & Poirier's solutions for comparison. The assumed heat transfer coefficient is used, as well as a higher value for comparison.
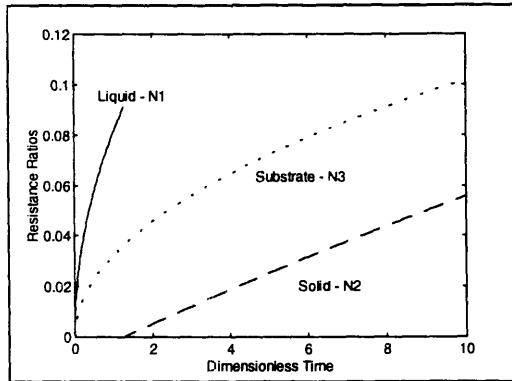
Figure 10a: Time Dependence of Thermal Resistance Ratios
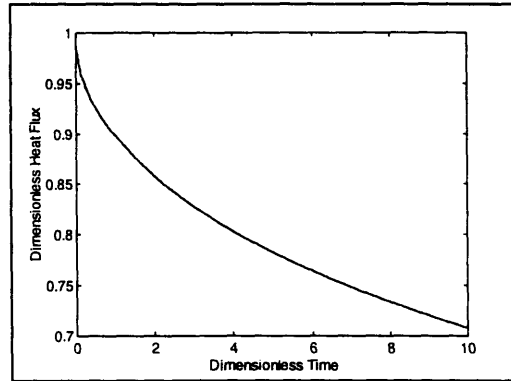
Figure 10b: Time Dependence of Heat Flux
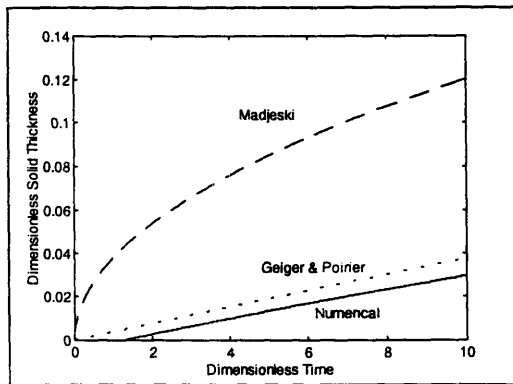
Figure 11a: Solid Growth
$h=10^4 \text{ W/m}^2 \text{ K}$
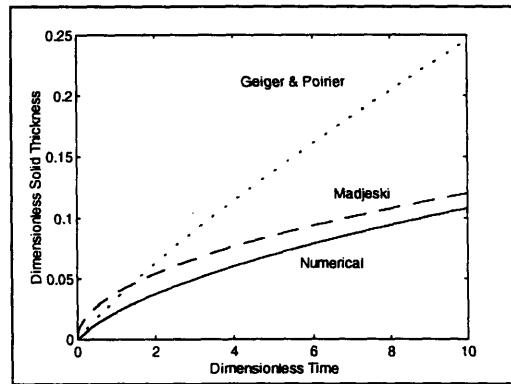
Figure 11b: Solid Growth
$h=10^5 \text{ W/m}^2 \text{ K}$

At the lower heat transfer coefficient, there is a significant delay before solidification starts. The thickness profile parallels Geiger & Poirier's solution, while Madjeski's predicts more rapid growth. At the higher heat transfer coefficient, Geiger & Poirier's solution overestimates the rate of growth while Madjeski's does better.

4.2.3 Observations

Immediately after impact, all droplets formed rapidly moving jets of fluid - a phenomenon which has been observed previously[19] and predicted numerically.[7,19] After this initial behavior, a variety of different spreading patterns was observed. In all cases, some flow reversal occurred. In some it was relatively minor, but in others a central column of liquid rose almost to the point of breaking up. The contact angle changed significantly as spreading proceeded. Rays or fingers almost always formed at the edge;

58

in some cases, they split off into smaller droplets. Occasionally, a thin solid layer at the periphery bottom was bent and pulled back in to the liquid.

Several representative examples of the transient spreading images described in chapter 3 are included here. Figure 12 shows a sequence of images of ID# 319_1. The liquid jet, finger-like protrusions, flow reversal, and subsequent re-spreading can all be seen.

0 ms

1.1 ms

3.8 ms

5.6 ms

16 ms

22.7 ms

24.9 ms

32.6 ms
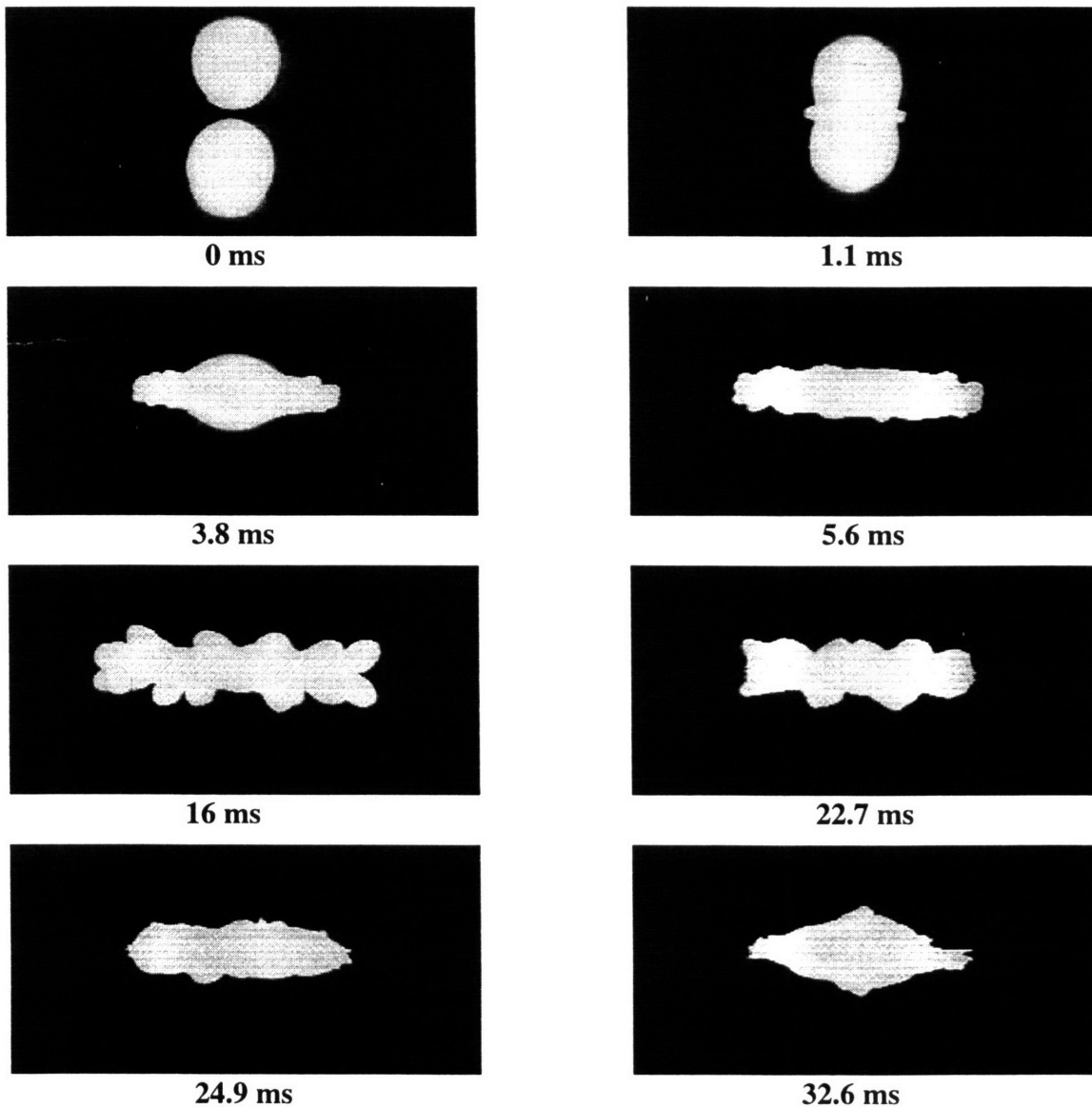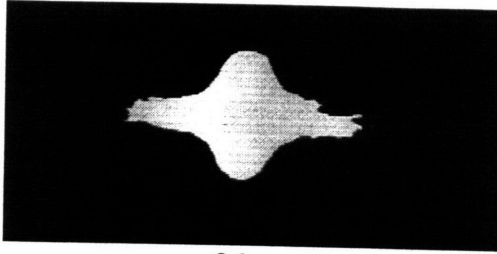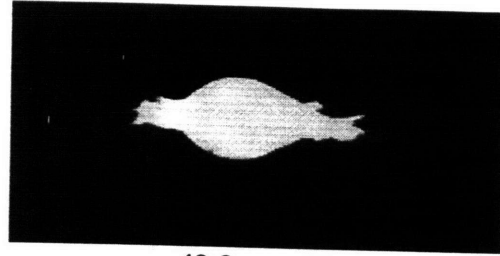
36 ms   **49.3 ms**

Figure 12: Spreading of MIT Splat ID# 319_1

Figure 13 shows a better view of the breakup at the edge. This image is of ID #319_2 at 9.8 ms. For both figures 12 and 13, the camera frame rate was 4,500 per second. With this amount of time per frame, and the bright radiation given off by the splats, the photographs are over-exposed. Consequently, the splat-reflection border is difficult to discern. In addition, the view is from an angle of 10°, so the image splat heights need to be corrected.
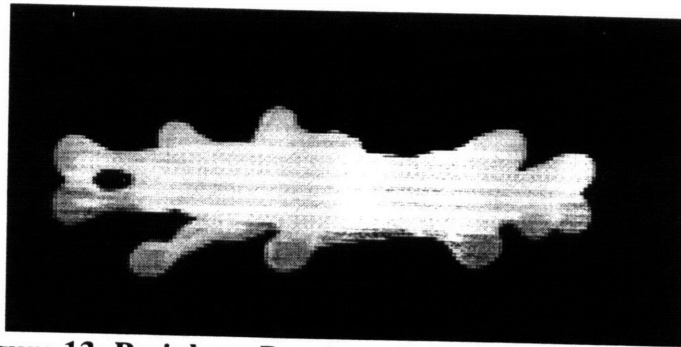
Figure 13: Periphery Break-up in MIT Splat ID #319_2

Figure 14 shows images from ID# 321_1, photographed at 18,000 frames/second from an angle as close to zero as equipment would allow. With a higher camera speed, there is less time for each exposure, so the contrast is better.

0 ms   **0.8 ms**   **1.7 ms**
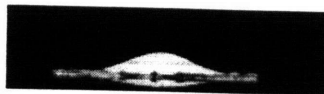
3.7 ms   **6.4 ms**

Figure 14: Spreading of MIT Splat ID# 321_1

As seen in Figure 15, ID# 328_1 at 9,000 frames per second. is actually darker than ID# 321_1 at 18,000 because the initial temperature is lower. This series clearly shows another frequent occurrence: mass accumulation at the periphery, followed by flow back towards the center.

| 0 ms | 0.9 ms | 3.6 ms |
| 5.8 ms | 18.2 ms | 26.9 ms |
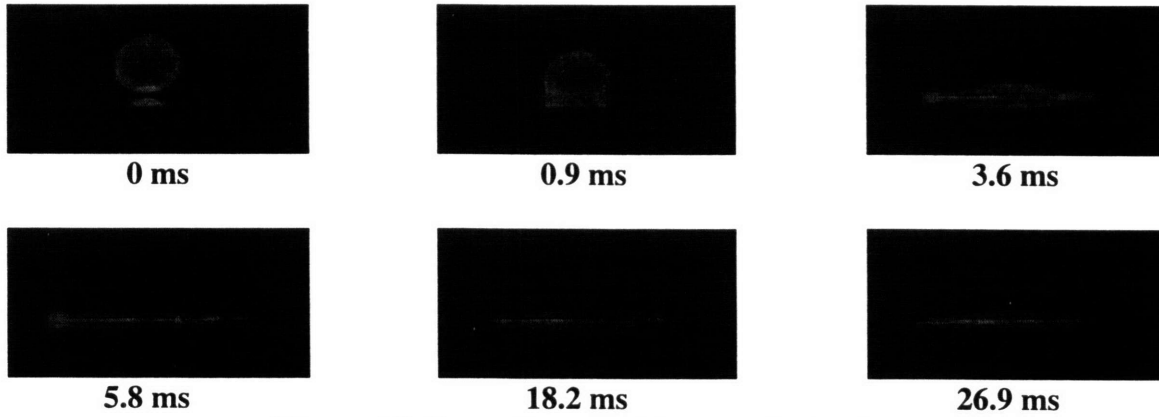
Figure 15: Spreading of MIT Splat ID #328_1

Figure 16, also at 9,000 frames per second, shows the most pronounced instance of back flow causing a liquid column to rise from the splat center. The changing contact angle can also be seen.

0 ms	0.7 ms
2.0 ms	5.8 ms
9.1 ms	12.4 ms

16.9 ms　　　　　　　　　　**24.7 ms**

32.4 ms　　　　　　　　　　**38 ms**
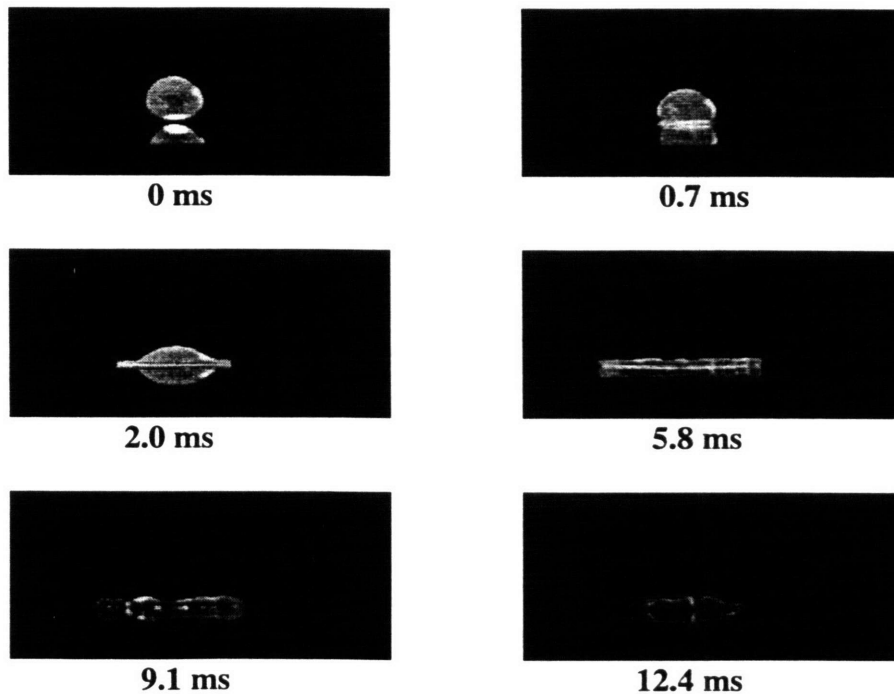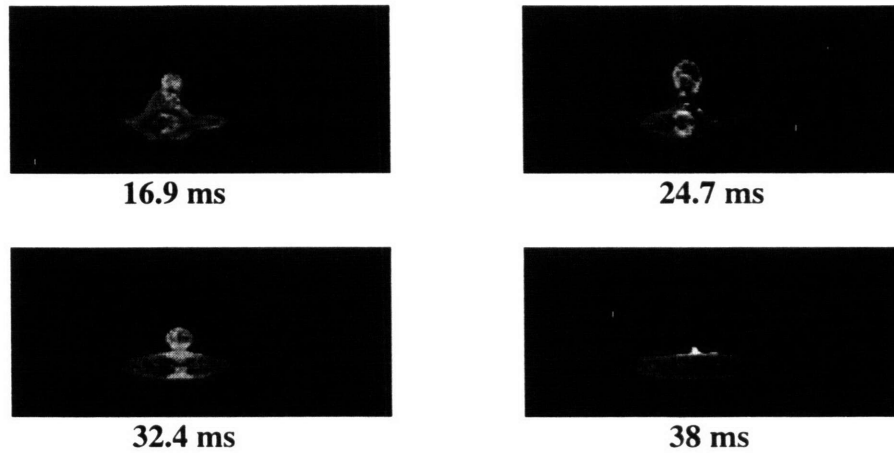
Figure 16: Spreading of MIT Splat ID# 329_3

Figure 17, images of splat ID# 329_4 also clearly shows periphery accumulation prior to flow reversal.

13.9 ms　　　　　　**18.3 ms**　　　　　　**19.4 ms**

20.6 ms　　　　　　**21.7 ms**　　　　　　**22.8 ms**

28.3 ms　　　　　　**33.9 ms**
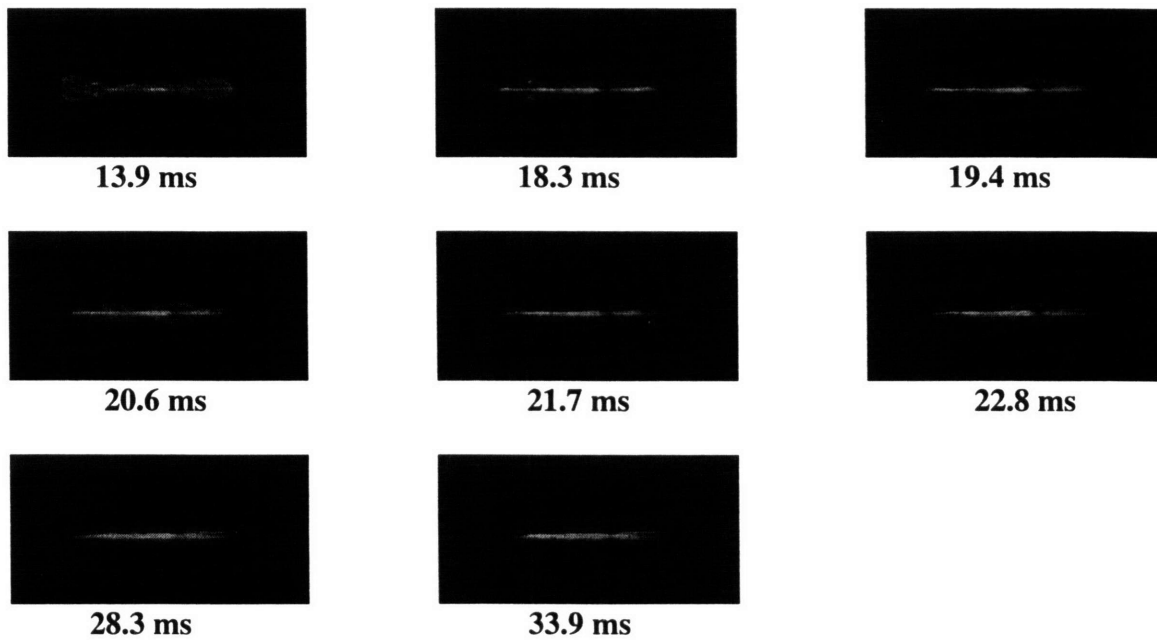
Figure 17: Spreading of MIT Splat ID# 329_4

These images and many more were analyzed as described, yielding transient spreading data. Complete data in tabular form is included in Appendix 2. A few cases of interest are shown here. Figures 18-21 show the behavior of ID#'s 319_1, 328_1, 329_3, and 329_4, respectively. ξ is marked by 'o,' and the observed height (the maximum of β plus Z) is marked by 'x.'
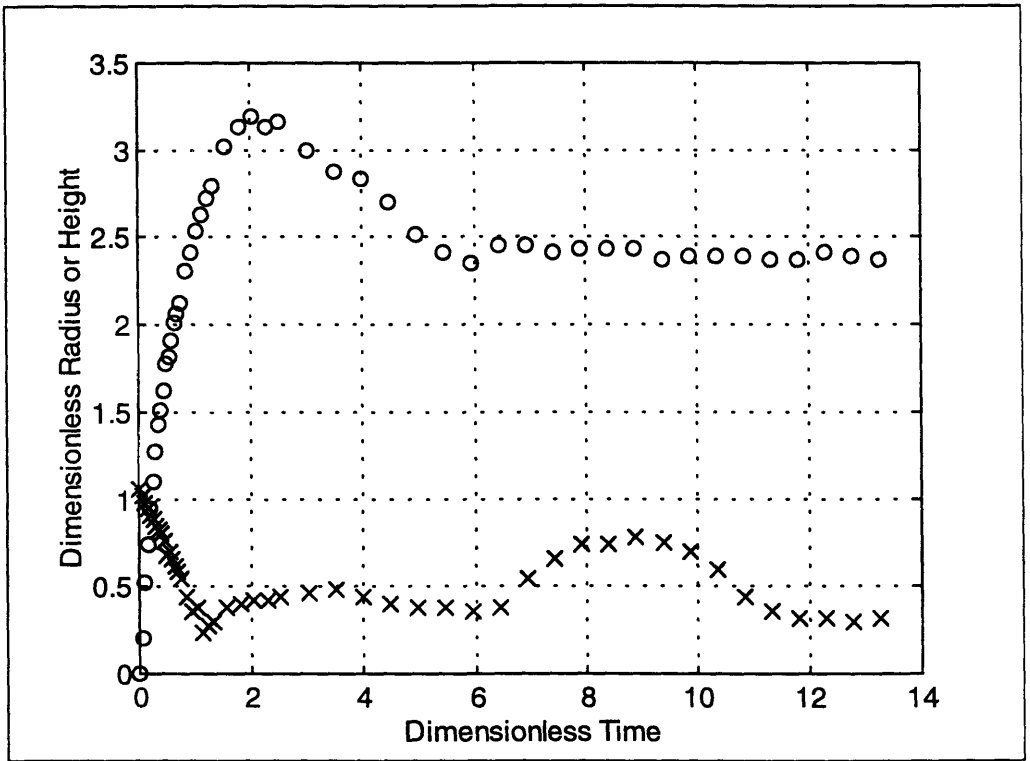
Figure 18: Transient Spreading of MIT Splat ID# 319_1
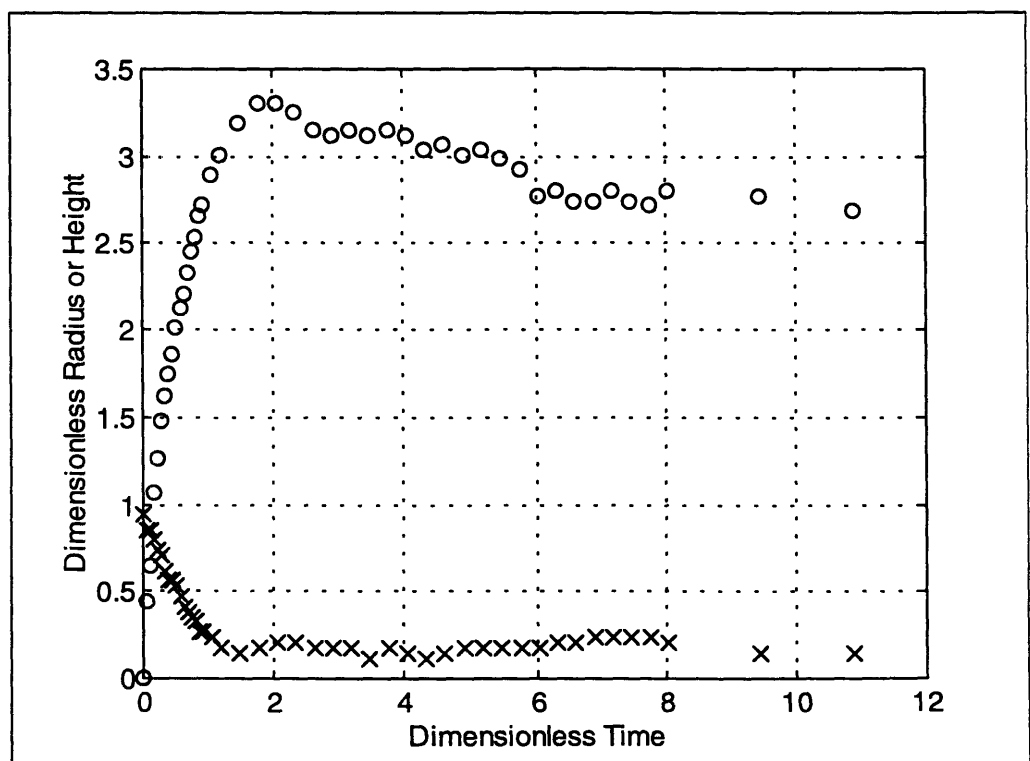
Figure 19: Transient Spreading of MIT Splat ID# 328_1
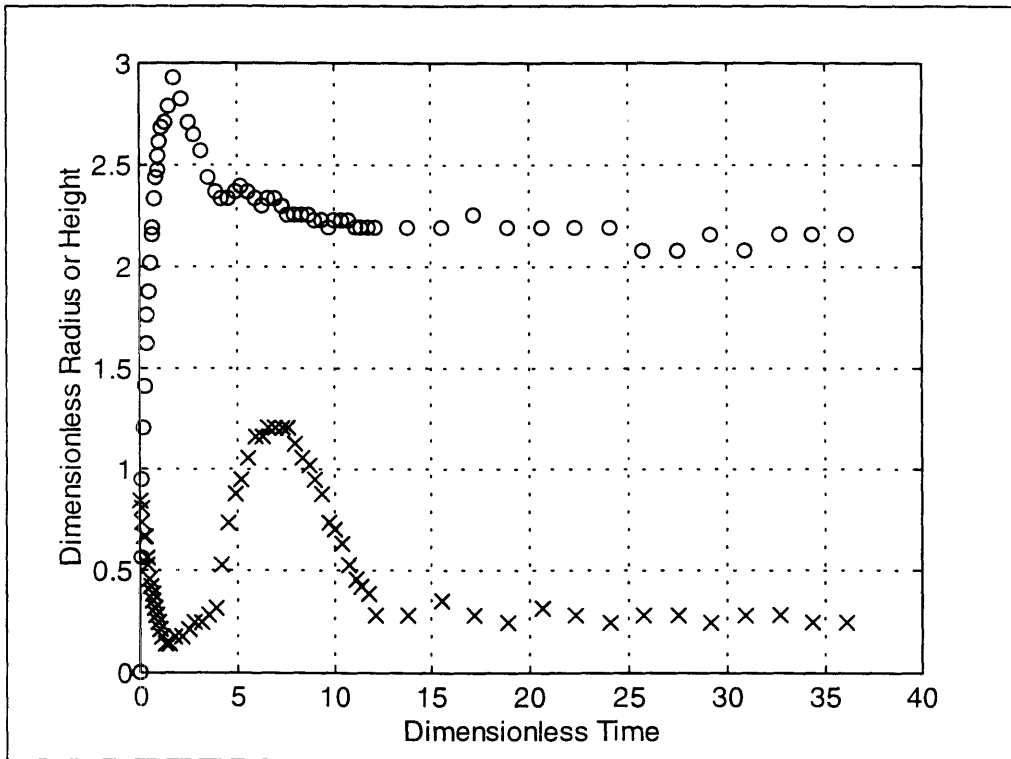
Figure 20: Transient Spreading of MIT Splat ID# 329_3
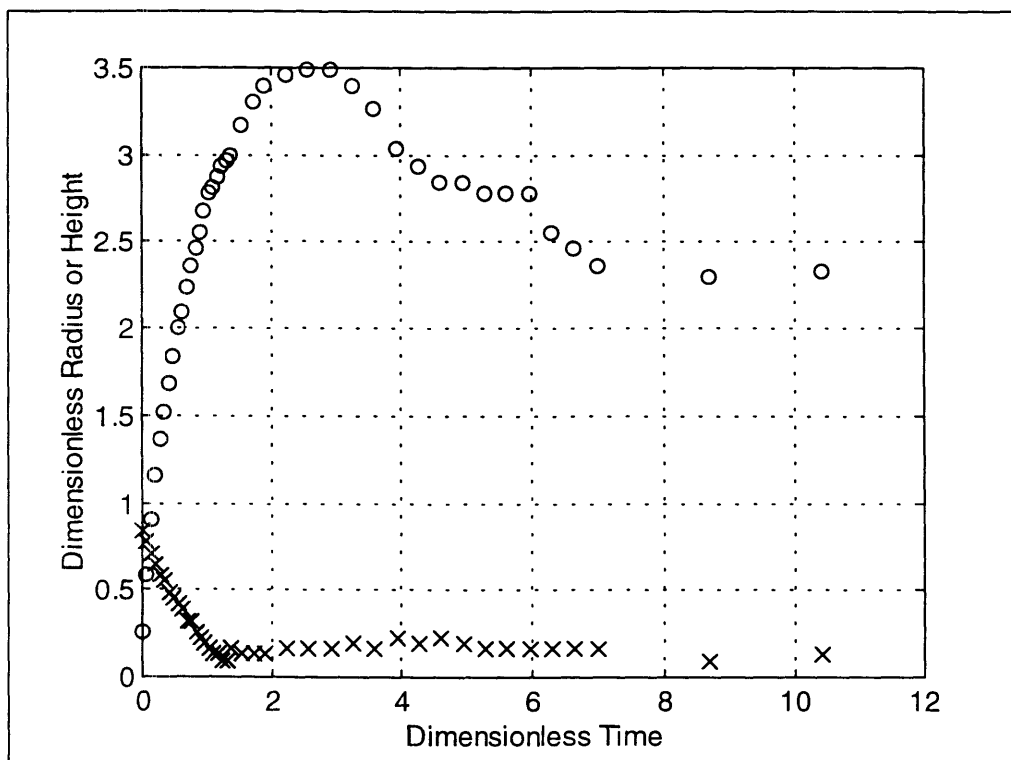
Figure 21: Transient Spreading of MIT Splat ID# 329_4

4.2.4 Spreading Model Predictions

Table 10 compares the observed final spreading extents, with the limiting value, as well as asymptotic predictions from Jones[10], Madjeski[12], Collings[5], Chandra & Avedisian[1], Trapaga & Szekely[19], Fukanuma & Ohmori[23], and Bennett & Poulikakos[27]. All formulas with contact angle dependence assume $\theta=90°$.

ID#	Obs.	Limit [65]	Jones [13]	Madj. [15]	Collings [16]	C&A [17]	T&S [18]	F&O [19]	B&P [20]
319_1	2.4	4.31	4.10	5.83	5.80	5.62	7.56	3.89	5.91
319_2	2.9	4.30	4.01	5.79	5.80	5.54	7.28	3.86	5.87
319_3	3.4	4.46	4.11	6.00	6.03	5.75	7.57	4.00	6.08
319_4	3.0	4.48	4.08	6.03	6.08	5.77	7.50	4.02	6.11
321_1	3.3	4.13	4.12	5.62	5.54	5.46	7.60	3.76	5.71
328_1	3.0	3.92	3.91	5.31	5.23	5.13	7.00	3.54	5.41
328_2	2.5	3.98	4.04	5.42	5.32	5.27	7.37	3.62	5.52
329_3	2.2	3.52	3.90	4.84	4.65	4.76	6.98	3.21	4.96
329_4	2.2	3.53	3.89	4.84	4.65	4.75	6.95	3.21	4.96
329_5	1.7	3.61	3.89	4.95	4.80	4.85	6.95	3.30	5.07
329_6	1.9	4.08	4.03	5.54	5.48	5.36	7.33	3.70	5.64

Table 10: Observed and Predicted MIT Final Spreading Extents

All the asymptotic models overestimate the final spreading extent. Some even predict values greater than the maximum possible.

The transient analytic spreading model developed in Chapter 2 is also used to model behavior under these conditions. These same four representative experiments, ID#'s 319_1, 328_1, 329_3, and 329_4, are chosen for comparison because both metals are included, and a wide range of Re, We, and τ_s is covered.

Figures 22-25 contain four graphs for each run. The first one plots the solid and liquid spreading extents versus dimensionless time. The observed peeling back is not modeled; any solid formed is assumed to stick to the substrate. While still flowing outwards, the submerged solid extent is marked by a dotted line. After flow reversal occurs, the liquid, which now rests on top of a wider solid splat, is depicted by a dashed line. The solid line marks the actual splat spreading extent, which is the greater of these two quantities. Experimentally observed points are indicated by an 'o' mark. The second plot shows

similar experimental observations of the maximum splat height, whether in the center or at the edge. The model prediction shown for comparison is the sum of the liquid and the maximum solid thicknesses. The third plot shows a time-dependent break-down of the system's component energies. The final plot in each series show the evolution of the solid fraction.
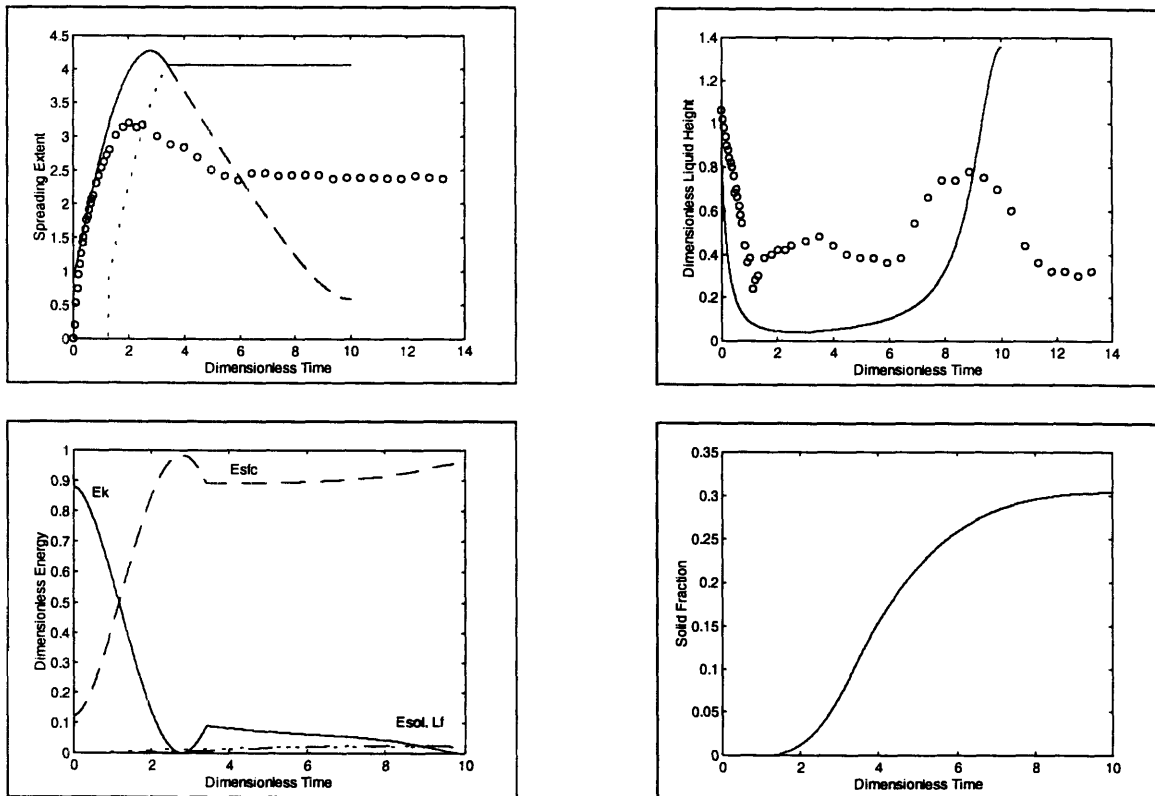
Figure 22: Spreading Model Output for MIT Splat ID# 319_1

Figure 22 reveals that the model predicts the same trends as the experiment showed, but it does not correctly predict all of the values in this case. Flow reversal and an increase in splat height are predicted and observed at similar times, but the model overestimates the extent of back-flow. The energy plot reveals the surface tension is the major means of consumption of the droplet's initial energy. The fraction solid rises quickly in-between the times when solidification starts and reversal occurs. Thereafter the splat is still solidifying, but at a slower rate because there is progressively less liquid area exposed, and the heat removed must be conducted through increasing thermal resistance.
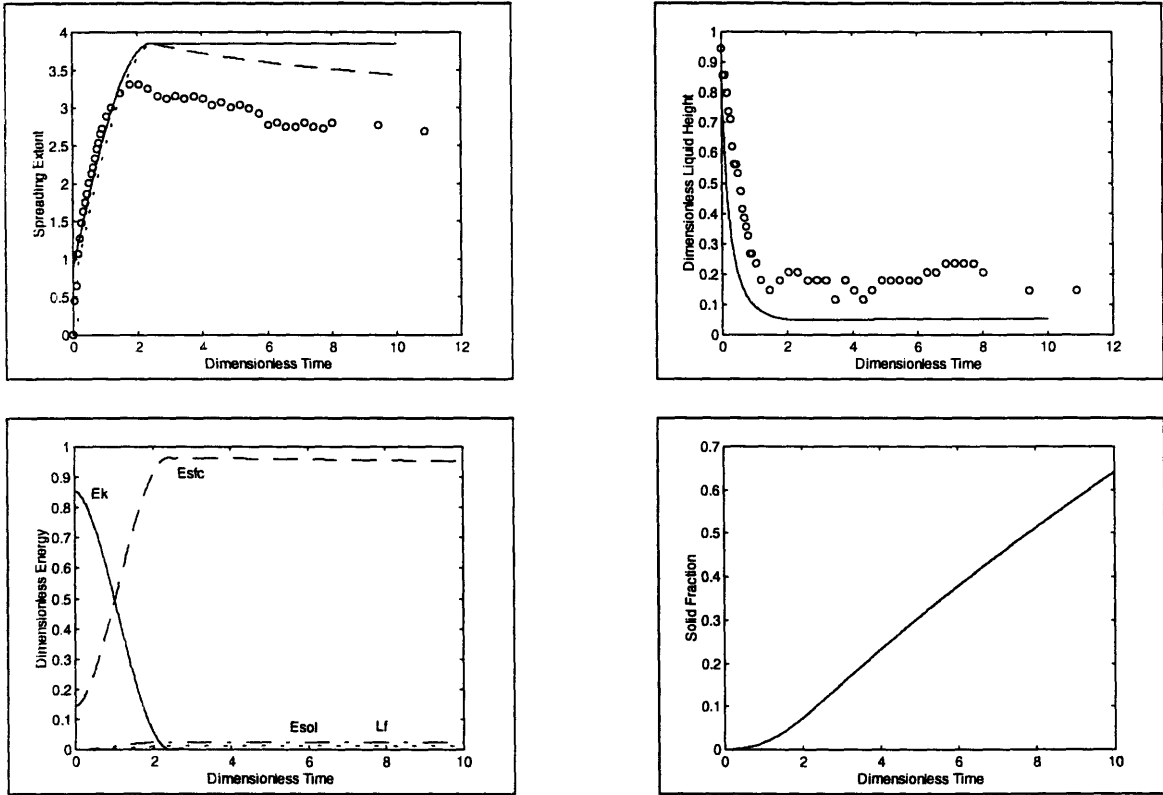
Figure 23: Spreading Model Output for MIT Splat ID# 328_1

Figure 23 shows similar behavior for ID# 328_1. The solidification delay is less in this case, so the frozen front stays closer to the liquid edge, preventing as large a flow reversal. Since more liquid area is exposed longer, the solid fraction grows to a value twice as large as the previous case.
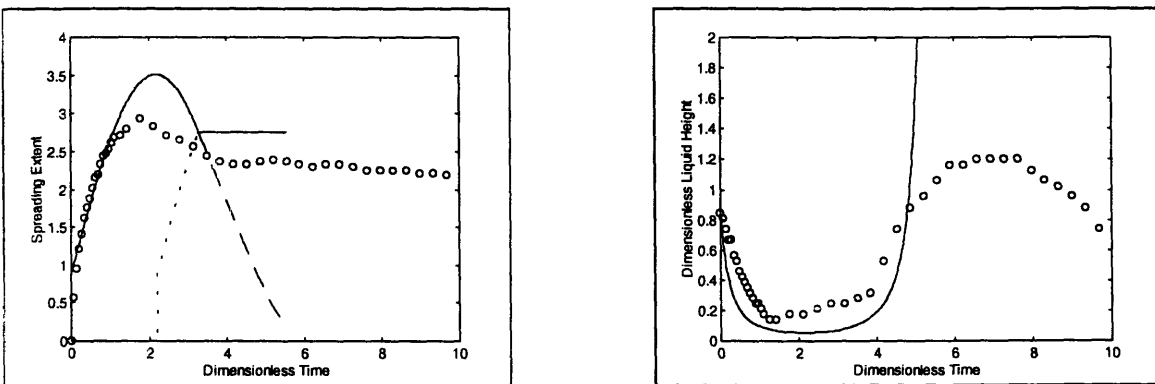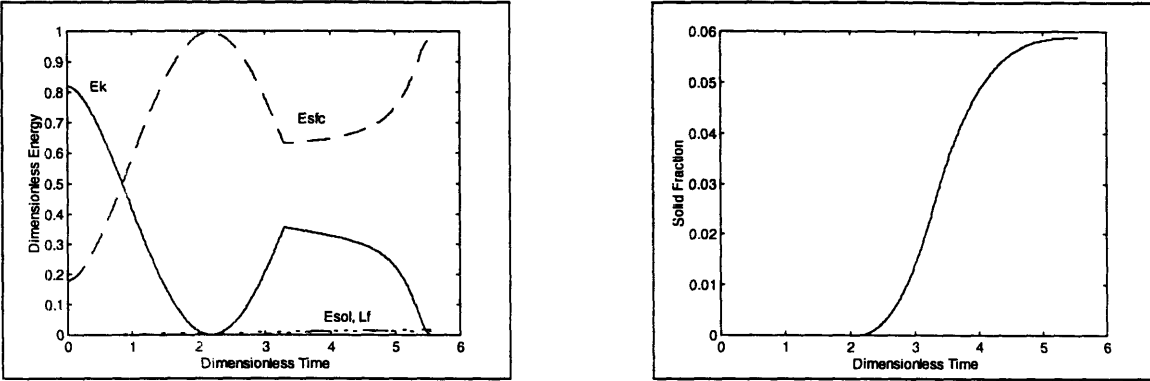
Figure 24: Spreading Model Output for MIT Splat ID# 329_3

ID# 329_3, as shown by Figure 24, contains much more significant splat oscillation. Though the experimental data goes to τ>30, the model calculation is stopped at τ≈6 due to difficulties predicting the solidification rate when multiple reversals occur. For the times presented, good agreement is obtained. The model predicts an excessive tendency to flow back towards the center, as shown by the continuing decrease of ξ, and the rise in splat height. This oscillatory behavior is due to the lowest Weber Number - 65- and one of the highest delay times - 2.193. These factors combine to produce energy oscillation between kinetic and surface terms, and a low solid fraction.

68
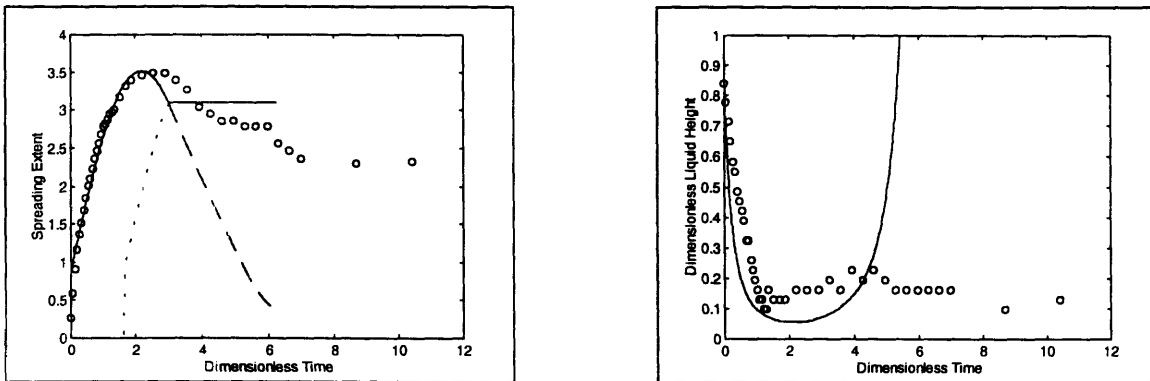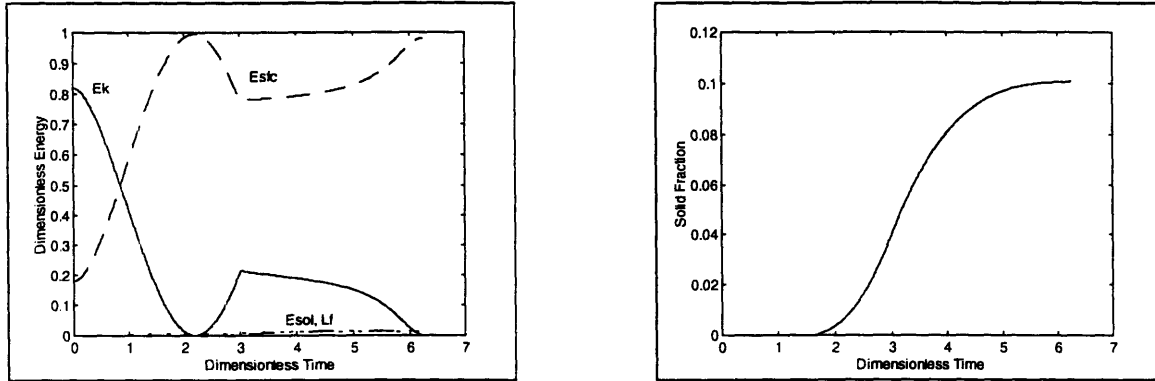
Figure 25: Spreading Model Output for MIT Splat ID# 329_4

ID# 329_4 is quite similar to 329_3, in terms of characteristic dimensionless numbers and transient behavior. The model agreement is even better in this case.

All simulations were performed using a time step, $d\tau=0.01$. An indication of numerical error is the difference between the sum of the dimensionless energy terms and unity. Though not plotted, this quantity was examined, and was found to be within a tolerance of one or two percent.

4.3 Marshall Space Flight Center Experiments

The Marshall Space Flight Center experiments used pure materials, binary alloys, and the glass-forming alloy, $Zr_{11}Ti_{34}Cu_{47}Ni_8$. Droplets of similar sizes were used, but the free fall height is 100m.

4.3.1 Free Fall Model Output

The droplet release temperatures are not known precisely, so a modest superheat of 50 K is assumed. Figure 26 demonstrates the free-fall model output for a 1.81 g Nickel droplet, released in a vacuum, and calculated with a time step of 0.004 s.
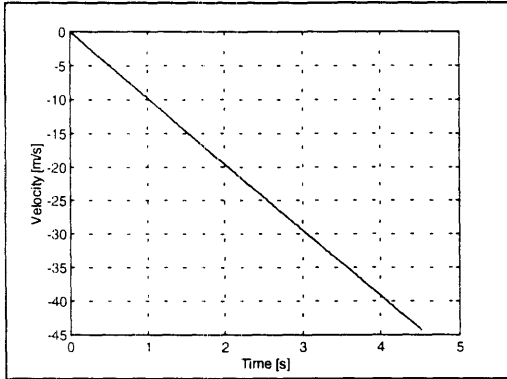
**Figure 26a: Free fall Model Output
MSFC Vacuum Experiment
Velocity Plot**
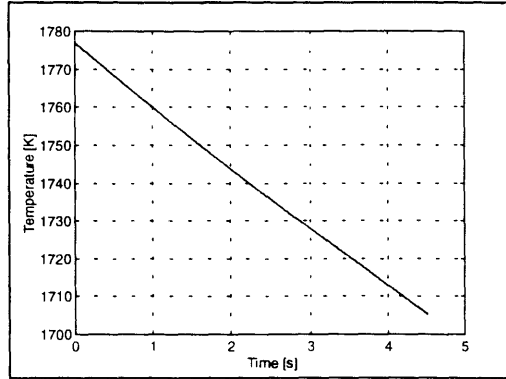
**Figure 26b: Free fall Model Output
MSFC Vacuum Experiment
Temperature Plot**

In a vacuum environment, the droplet accelerates until impact, hitting with velocity v_{max} at a time of

$$t_{min} = \sqrt{\frac{2z}{g}}$$ [96]

which equals 4.52s for this case. There are no convective heat losses, so the entire 72° temperature change is radiative. A $Zr_{11}Ti_{34}Cu_{47}Ni_8$ droplet of equal mass and superheat, falling through identical conditions would have the same impact velocity and radiative losses of 21°, giving an impact temperature of 1182K.

A more interesting case occurs when the tube is back-filled with gas. For the same Nickel droplet falling through Argon at 700 torr, Figure 27 shows the result.
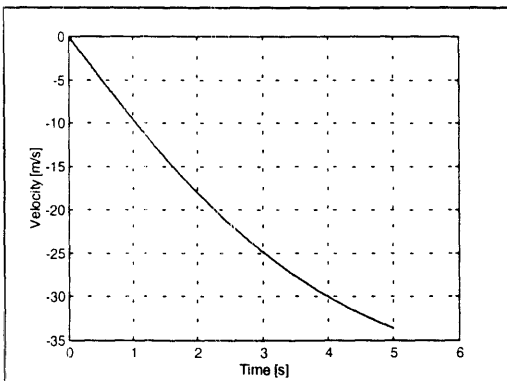
**Figure 27a: Free fall Model Output
MSFC Gas-Filled Experiment
Velocity Plot**
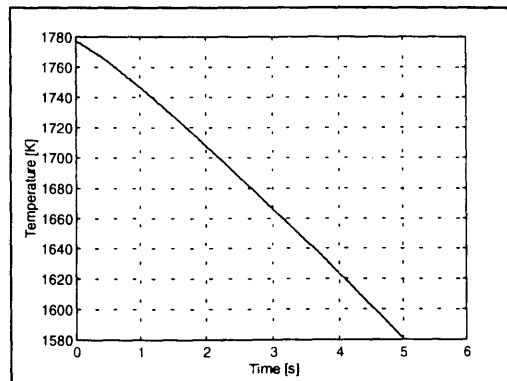
**Figure 27b: Free fall Model Output
MSFC Gas-Filled Experiment
Temperature Plot**

70

Drag effects do become important, slowing the droplet to 33.6 m/s, and extending its flight time by roughly 0.5 s. Convection now removes significant energy. If nucleation of the undercooled droplet is suppressed, its temperature falls by 196° - to an undercooling of 146° - with convection accounting for 64% of this loss. A $Zr_{11}Ti_{34}Cu_{47}Ni_8$ droplet experiences similar effects, impacting 5.08 seconds after release, with a velocity of 32.3 m/s, and a temperature of 1083K. Convective losses account for 83% of the heat lost in this case.

The dimensionless numbers characterizing these systems at impact are listed in Table 11.

System	Impact Velocity [m/s]	Impact Temperature [K]	Re	We	Fr
Ni, Vacuum	44.3	1705	4.6×10^5	6.6×10^4	2.6×10^4
Ni, Argon	33.6	1581	2.7×10^5	3.8×10^4	1.5×10^4
$Zr_{11}Ti_{34}Cu_{47}Ni_8$, Vacuum	44.3	1182	3.4×10^5	6.9×10^4	2.5×10^4
$Zr_{11}Ti_{34}Cu_{47}Ni_8$, Argon	32.3	1083	6732	3.6×10^4	1.3×10^4

Table 11: MSFC Experimental Impact Conditions

With the exception of the $Zr_{11}Ti_{34}Cu_{47}Ni_8$ - Argon simulation, all three dimensionless numbers are much larger than they were for the MIT experiments. Gravitational energy is certainly negligible; even the surface energy of the incident droplet is insignificant. Clearly, there is an overwhelming inertial tendency. The unusually low Reynolds number of the $Zr_{11}Ti_{34}Cu_{47}Ni_8$ - Argon case is due to the highly temperature dependent viscosity characteristic of glass-forming alloys and the substantial undercooling at impact.

4.3.2 Solidification Model Output

Freezing numbers cannot be defined as they were in equation 95, for the regime encompassing these conditions is not known *a priori*. Furthermore, $Zr_{11}Ti_{34}Cu_{47}Ni_8$ usually forms an amorphous phase rather than crystalline solidification, so that no latent heat of fusion is released. Table 12 gives the dimensionless heat transfer parameters for the example Nickel droplets only, again for $h=10^4$ W/m^2 K.

System	$N_1/\tau^{0.5}$	N_2/Z	$N_3/\tau^{0.5}$	N_4	N_5	τ_s
Ni - Vac.	0.0145	0.866	0.00624	1.37×10^{-4}	1	0
Ni - Ar	0.0169	0.862	0.00715	1.61×10^{-4}	1	0

Table 12: MSFC Experimental Heat Transfer Parameters

N_1, N_3, and N_4 all decrease due to the fact that the spreading time scale has shortened while that of heat transfer remains the same. Time is non-dimensionalized with respect to fluid flow, so the change in scale affects these numbers. N_2 values do not change significantly because they do not depend on time. Solidification also starts instantly now. As soon as contact is made, solid is nucleated, and the droplet recalesces. With the sudden back to the melting temperature, N_5 returns to unity.

4.3.3 Observations

A sample series of photographs of one Marshall Space Flight Center Drop, nt4798, is included as Figure 28. These photographs of a Nickel droplet were taken 20µs apart. The high speed lateral jet can be seen, but there is no sign of mass accumulation at the periphery, flow reversal, or a centerline height rise.
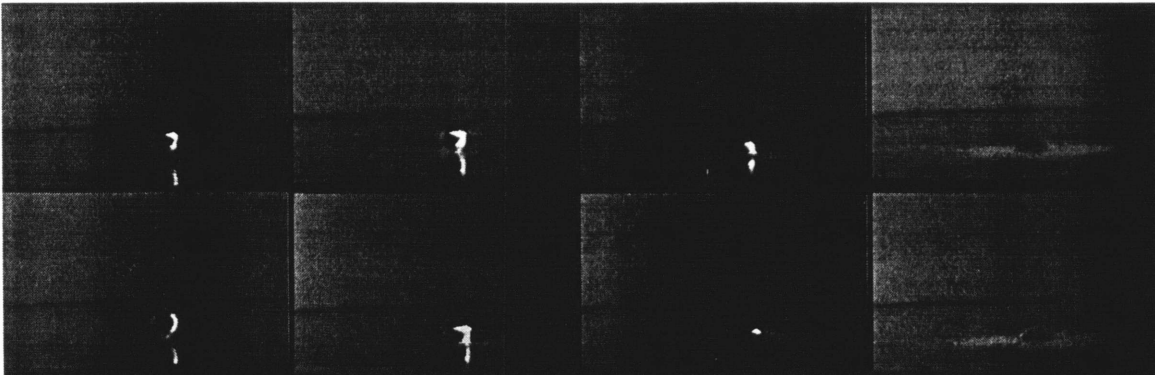
Figure 28: Spreading of Marshall Space Flight Center Splat ID# nt4798

Digitization of this image yields transient spreading data that is compared to model predictions in the next section.

4.3.4 Spreading Model Predictions

Again, the asymptotic models are presented first - in Table 13. Then the transient analytic model developed earlier is compared in Figure 29. The splat was not photographed for the entire duration of spreading, and it became too fragmented during removal to accurately measure the observed spreading extent. However, values near 10 were commonly observed.

System	Limit	Jones	Madj.	Collings	C&A	T&S	F&O	B&P
Ni-Vac.	105	5.91	17.5	148	17.8	13.6	9.30	17.5
Ni-Ar	79.6	5.53	15.7	113	15.6	12.2	8.51	15.7

Table 13: Predicted Final Spreading Extents - MSFC Experiments

It is obvious that surface tension is no longer the limiting factor, as evidenced by the huge difference between predictions based solely on this consideration (Limiting and Collings), and all others.
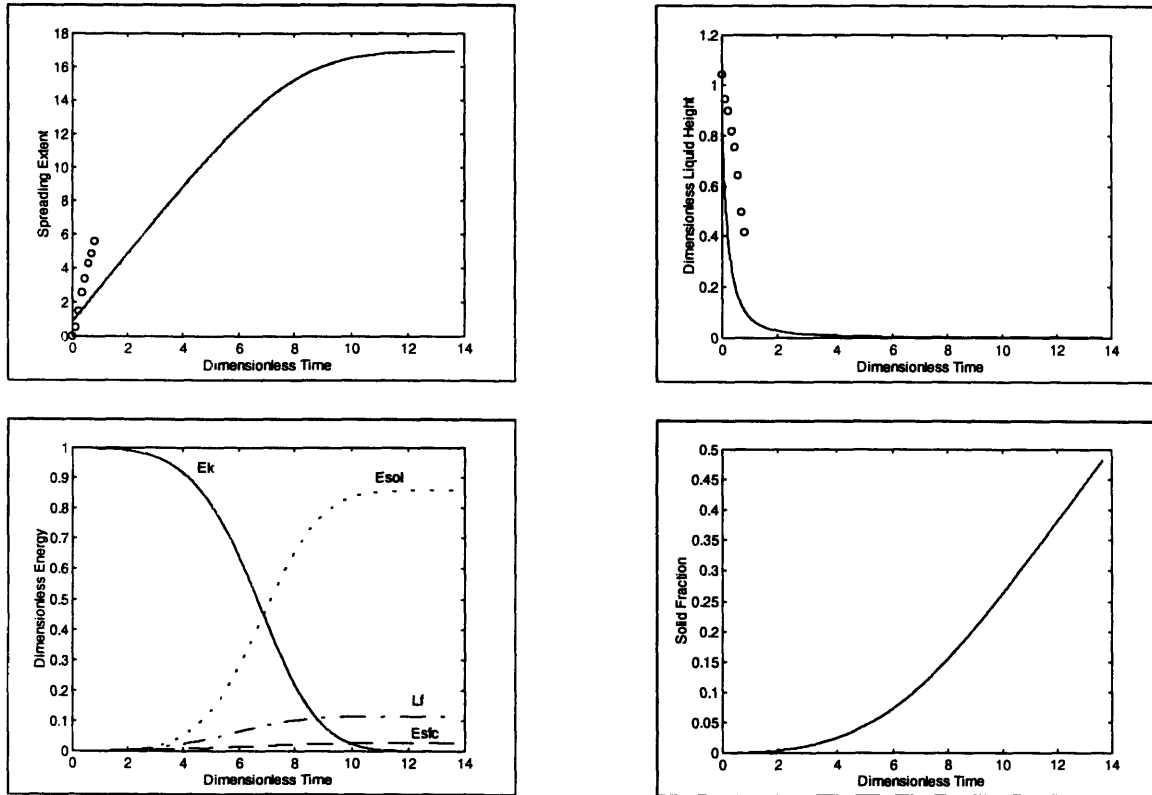
Figure 29: Spreading Model Output for MSFC Splat ID# nt4798

73

The quantitative model agreement under these conditions leaves something to be desired, but the behavior predicted makes intuitive sense. A longer period of spreading and higher spreading extents are required before solidification and viscous losses consume much of the initial energy. Surface effects are secondary in this case. Both model and experiment reveal an initial spreading period with a nearly constant rate. In reality the splat spreads faster because of the thin, jet-like, sheet of fluid formed at the bottom. This sheet moves outwards at a speed several times the impact velocity, giving a steep slope on a $\xi-\tau$ plot. The spreading model cannot represent this behavior well since the splat is assumed cylindrical. The entire model periphery moves outward at one rate, slower than that of such a jet.

4.4 Other Experiments

Just as the transient analytic spreading model can be applied to the experimental conditions of the MIT and Marshall Space Flight Center campaigns in this work, it can be compared to other reports of transient spreading data in the literature. Figure 30 shows the model predictions for the fully liquid cases of two of Shi's[26] experiments. The solid line and the 'o' marks correspond a case with Re=10,563 and We=259; the dotted line and 'x' marks are for Re=4397 and We=53.8. Figure 31 compares model output and Fukanuma & Ohmori's[27] experiment #5 - in which a Tin droplet spread and froze on a Stainless Steel surface. The characteristic dimensionless numbers are Re=22,072, We=181, and τ_s=0.0708.
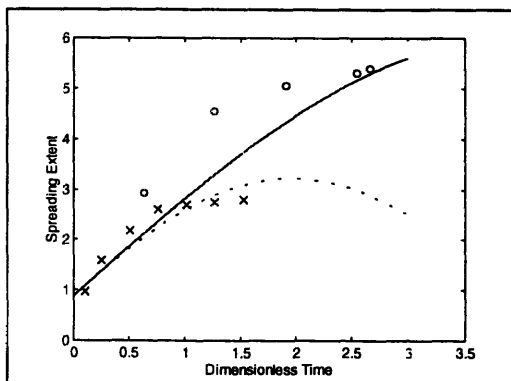
Figure 30: Spreading Model Output Comparison with Shi
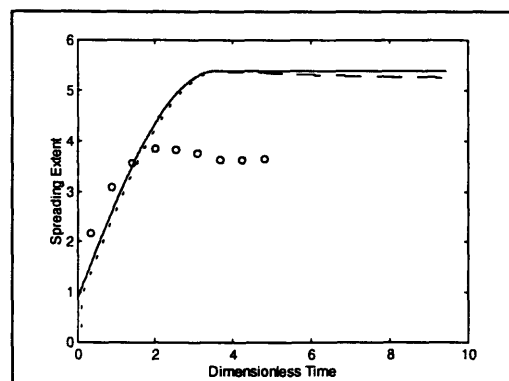
Figure 31: Spreading Model Output Comparison With Fukanuma & Ohmori

CHAPTER 5 - DISCUSSION AND CONCLUSIONS

5.1 Models Developed

A new comprehensive model has been developed to consider the flight, impact, spreading, and freezing of liquid metal droplets impacting a solid substrate. The pre-impact flight model is an improvement over existing models because it addresses radiation, which is an important heat transfer mode for many high-melting materials used in plasma spraying and spray forming. The spreading portion is based on a combination of an integral energy balance and a transient force on the splat. Viscous, surface tension, and solidification effects are considered for an assumed cylindrical geometry. The model contains many new features: revised surface energy considerations, solidification losses, the inclusion of all relevant heat transfer considerations, and a solidification delay.

This model combines the best features of the analytic and numerical modeling approaches. It is less calculationally intense than many pure numerical models, and consequently much less time-consuming - both in terms of set-up and computational time. It is still able to provide the same transient data for comparison with experimental observations, however.

The surface area of the assumed cylindrical shape now also includes the splat bottom, a curious omission from many previous models. Instead of picking an arbitrary convenient initial cylinder radius, a value is justified based on a surface energy argument. A new energy consideration, solidification energy, is added to the viscous and surface energy terms used by others. This solidification energy is the energy essentially frozen out of the moving liquid as it freezes into stationary solid. Heat transfer modeling encompasses all four thermal resistances in the system and shows that the interface is limiting in most cases. A delayed solidification start for superheated droplets makes flow reversal possible by permitting the liquid to recoil backwards some distance without leaving frozen solid below it.

5.2 Experimental Technique

In addition, a direct high-speed digital photographic technique is applied to the study of molten metal droplet spreading. Series of clear, transient spreading images - at the speeds necessary to observe typical spreading time scales - are obtained. The MIT experiments also demonstrate the ability to avoid the problems of artificial lighting by using sufficiently bright, high-melting samples. Image processing of the resulting photographs proves to be a consistent way to extract the desired spreading data for comparison with models.

5.3 Model Performance

For conditions typical of the MIT experiments, the model output matches well with the observed spreading behavior. Two independent experiments with similar conditions yield similar consistency. The agreement is best for moderately superheated droplets which can recoil, but which do wait so long to freeze that they approach the fully liquid flow regime. Calculations reveal frequent flow reversal and splat oscillations, but tend to exaggerated the extent of back flow. The difficulty lies in the fact that no significant outwardly-directed restoring force exists until the model splat is quite tall and narrow. Also, there is no account for the liquid's tendency to cling to the remaining mushy zone on top of solid that is being exposed during back flow. These real but unmodeled factors combine to hold the splat back from reversing as far as predicted.

The model also does a good qualitative job of describing the Marshall Space Flight Center experiments. The overwhelming inertial tendency at impact gives way primarily to viscous and solidification losses. Surface effects are secondary. The quantitative model-experiment agreement is not as good. Specifically, the observed initial spreading rate is higher than that predicted. This discrepancy can be explained by considering the thin fluid sheets described in previous works.[7,19] While much of the droplet retains its spherical shape and gradually approaches the substrate, the remainder is ejected radially outwards at spreading rates several times the incident velocity. Thus, part of the splat side is moving very rapidly outwards while the remainder is moving predominantly

downwards. This situation is quite different from the cylindrical model, which assumes the splat has a single radius and a single spreading rate - uniform across its height.

The assumed velocity distribution may also contribute to both of these discrepancies. Madjeski purposefully used a simple field in order to keep the problem manageable. A more complex field may be better able to represent the sharp velocity gradients in the liquid jet during the initial stages of spreading.

Predicted final spreading extents are lower than many other models at the same Reynolds and Weber numbers. This trend is due to the inclusion of both surface and viscous terms at all points rather than an assumption that a single effect is controlling. Taking the splat bottom surface into account also reduces the predicted spreading extents.

Due to difficulties in predicting solidification behavior after multiple reversals, it was not possible to simulate all cases until the termination of spreading. Consequently, the final breakdown of energy expenditure could not be found, and the Re-We window cannot be clearly divided into regions, as in Bennett & Poulikakos' paper. Still, quite a difference is apparent between the two sets of experiments conducted for this work. Surface tension is the primary restraint under conditions similar to those of the MIT experiments. Viscous and solidification losses are the critical features for the more inertially-dominated conditions typical of the Marshall Space Flight Center campaign.

Freezing appears to have more than the secondary effect described by Bennett & Poulikakos. Solidification phenomena affect the possibility and extent of flow reversal. Freezing can also consume energy comparable to that of viscous effects.

A potential area for model refinement is the treatment of the liquid and substrate heat-affected zones as semi-infinite media. This treatment is valid if the following inequality is true:

$$x > 2\sqrt{\alpha t} \qquad\qquad [97]$$

where x is a spatial dimension in the same direction as heat conduction, α is the thermal diffusivity:

$$\alpha = \frac{k}{\rho c_p} \qquad [98]$$

For a substrate of known thickness, equation 97 can be re-arranged to estimate the time during which it appears effectively semi-infinite.

$$t < \frac{x^2}{4\alpha} \qquad [99]$$

The Copper substrate used in the MIT experiments is 1.6 mm thick, so t must be less then 5 ms. This corresponds to $\tau \approx 1.2$ for a typical splat. Since most simulations were performed up to $\tau=10$, this assumption is clearly not valid for the duration of spreading. The effect of a finite substrate would be to decrease the heat flux through this layer and prolong solidification. Fortunately, the heat transfer process is dominated by interfacial resistance, even for times longer than this. At $\tau=10$, the semi-infinite substrate resistance would be 10% of the interface's. The same test can be applied to the liquid. The times obtained from typical x and α values are longer than the solidification delays of all but the most superheated droplets. Since the liquid resistance is only considered up to τ_s, this approximation should not lead to any negative consequences.

APPENDIX 1 - MATLAB™ SOURCE CODE

Appendix 1 contains the source code for the Matlab programs used: freefall.m, begin.m, freeze.m, and splat.m. Freefall.m computes droplet behavior before impact. Begin.m prompts the user for system information and defines some physical variables. Freeze.m models transient heat transfer until solidification starts, and splat.m computes the time-dependent spreading behavior. All programs use MKS quantities for variables.

A1.1 Freefall.m

```
% Matlab m-file script for Freefall Model
% Numerical Simulation of Droplet Descent Before Impingement
%
% Assumptions:
%       - zero initial velocity
%       - 1 atm stationary Helium for first few centimeters
%       - 1 atm stationary Argon for final 8.8
%       - lumped capacitance method
%       - linear density-temperature dependence
%       - linear surface energy-temperature dependence
%       - Arrhenius viscosity-temperature dependence
%       - Constant Specific Heat
%       - Nearly linear thermal conductivity temperature dependence
%
% Inputs
MIT=input('Enter Experiment Site, 1=MIT, 2=MSFC ');
if MIT==1
        Z=input('Enter Distance Between Coil Center and Catch Tank Lid Top [cm] ');
else
        Z=1e4;
end
me=input('Enter Code For Metal, 1=Co, 2=Ni, 3=Zr11Ti34Cu47Ni8 ');
m=input('Enter Droplet Mass [g] ');
T=input('Enter Droplet Release Temperature [K] ');
P=input('Enter Pressure [torr] ');
if (MIT==2)&(P~=0)
        gas=input('Enter Code for Gas, 1=He, 2=Ar ');
end
dt=input('Enter Time Step [s] ');
%
% Input Manipulation
if MIT==1
        Z=(Z+10)/100;                          % Add Catch Tank Depth and Covert cm to m
else
        Z=Z/100;                               % Convert cm to m
end
m=m/1000;                                      % Convert g to kg
P=P*101325/760;                                % Convert torr to Pa
%
% Constants
g=-9.8;                                        % Acceleration of Gravity [m/s2]
sb=5.67e-8;                                    % Stefan-Boltzman Constant [W/m2K4]
```

```
Tgas=300;
%
% Table of Metal Properties
% Rows for Co, Ni, Zr11Ti34Cu47Ni8
%        Tm   rhom   drho/dT  sigma dsigma/dT  mu0    E for mu  cp    alpha   beta  emissivity
%        [K] [kg/m3] [kg/m3 K] [J/m2] [J/m2 K] [kg/m s]  [J/mol] [J/kg K] [uohm cm/K] [uohm cm]
metprop=[1766 7750   -1.09   1.873 -4.9e-4  2.55e-4  4.44e4   685    .0612    -6     0.2;
         1727 7900   -1.19   1.778 -3.8e-4  1.663e-4 5.02e4   656    .0127    63     0.2;
         1153 6355   -0.58   1.478 -2.5e-4  4.864e-20 3.88e5  575    .0302    0      0.2];
% Matrix of Gas Properties - at 1atm, 300K
% Rows for He, Ar
%        rhog    mug     kg      cpg     Pr
%        [kg/m3] [kg/m s] [W/m K] [J/kg K]   []
gasprop=[0.1625  199e-7  152e-3   5193    0.680;
         1.623  2.265e-5 1.768e-2 520.4   0.6667];
%
% Initial Conditions
z=Z;                                                      % Initial Height
v=0;                                                      % Initial Droplet Velocity
t=0;                                                      % Initial Time
hitflag=0;                                                % Flag Signifying Impact
lumpflag=0;                                % Flag to check Lumped Capacitance Validity
dTcontot=0;                               % Cumulative Heat Lost Through Convection
dTradtot=0;                                % Cumulative Heat Lost Through Radiation
Bimax=0;                                                  % Maximum Biot Number
I=1;                                                      % Iteration Index
%
% Freefall Algorithm
while hitflag==0
    % Metal Properties
    rhodrop=metprop(me,2)+metprop(me,3)*(T(i)-metprop(me,1));
    cpdrop=metprop(me,8);
    e=metprop(me,11);
    kdrop=2.45*T(i)/(metprop(me,9)*T(i)+metprop(me,10));
    udrop=metprop(me,6)*exp(metprop(me,7)/(8.314*T(i)));
    sdrop=metprop(me,4)+metprop(me,5)*(T(i)-metprop(me,1));
    %
    % Particle Diameter
    D(i)=(6*m/(pi*rhodrop))^(1/3);
    %
    if MIT==1
        % Gas Properties
        if z(i)>8.8e-2                                    % Helium Atmosphere
            rhogas=gasprop(1,1);
            ugas=gasprop(1,2);
            kgas=gasprop(1,3);
            Prgas=gasprop(1,5);
        else                                              % Argon Atmosphere
            rhogas=gasprop(2,1);
            ugas=gasprop(2,2);
            kgas=gasprop(2,3);
            Prgas=gasprop(2,5);
        end
        % Gas Reynolds Number
        Regas=abs(rhogas*v(i)*D(i)/ugas);
```

```
%
% Drag Coefficient
if Regas~=0
    Cd(i)=0.28+6*Regas^(-0.5)+21/Regas;
else
    Cd(i)=0;
end
%
% Convective Heat Transfer Coefficient evaluated with Ranz-Marshall Equation
h=kgas*(2+0.6*Regas^(1/2)*Prgas^(1/3))/D(i);
%
    % Check Lumped Capacitance Validity with Biot Number (takes Radiation and Convection into
account)
    Bi=(h+e*sb*T(i)^3)*D(i)/kdrop;
    if Bi>0.1
        lumpflag=1;
    end
    if Bi>Bimax
        Bimax=Bi;
    end
%
% Calculation of Force on Droplet and Droplet Acceleration
a=g+Cd(i)*rhogas*pi*D(i)^2*v(i)^2/(8*m);
%
% Calculation of New Droplet Height via Three Term Taylor Series
z(i+1)=z(i)+v(i)*dt+a*dt^2/2;
%
% Check for Impaction
if z(i+1)<0
    hitflag=1;
end
%
% Calculation of New Droplet Velocity via Runge-Kutta Integration
kn1=a;
vkn2=v(i)+kn1*dt/2;
Rekn2=abs(rhogas*vkn2*D(i)/ugas);
if Rekn2~=0
    Cdkn2=0.28+6*Rekn2^(-0.5)+21/Rekn2;
else
    Cdkn2=0;
end
kn2=g+Cdkn2*rhogas*pi*D(i)^2*vkn2^2/(8*m);
vkn3=v(i)+kn2*dt/2;
Rekn3=abs(rhogas*vkn3*D(i)/ugas);
if Rekn3~=0
    Cdkn3=0.28+6*Rekn3^(-0.5)+21/Rekn3;
else
    Cdkn3=0;
end
kn3=g+Cdkn3*rhogas*pi*D(i)^2*vkn3^2/(8*m);
vkn4=v(i)+kn3*dt;
Rekn4=abs(rhogas*vkn4*D(i)/ugas);
if Rekn4~=0
    Cdkn4=0.28+6*Rekn4^(-0.5)+21/Rekn4;
else
```

```
            Cdkn4=0;
    end
    kn4=g+Cdkn4*rhogas*pi*D(i)^2*vkn4^2/(8*m);
    v(i+1)=v(i)+dt*(kn1+2*kn2+2*kn3+kn4)/6;
    %
    % Calculation of Droplet Temperature via Runge-Kutta Integration
    kn1=-pi*D(i)^2*(h*(T(i)-Tgas)+e*sb*T(i)^4)/(m*cpdrop);
    Tkn2=T(i)+kn1*dt/2;
    kn2=-pi*D(i)^2*(h*(Tkn2-Tgas)+e*sb*Tkn2^4)/(m*cpdrop);
    Tkn3=T(i)+kn2*dt/2;
    kn3=-pi*D(i)^2*(h*(Tkn3-Tgas)+e*sb*Tkn3^4)/(m*cpdrop);
    Tkn4=T(i)+kn3*dt;
    kn4=-pi*D(i)^2*(h*(Tkn4-Tgas)+e*sb*Tkn4^4)/(m*cpdrop);
    T(i+1)=T(i)+dt*(kn1+2*kn2+2*kn3+kn4)/6;
    %
    % Separate Radiative and Convective Losses
    dTradtot=dTradtot-pi*dt*D(i)^2*e*sb*T(i)^4/(m*cpdrop);
    dTcontot=dTcontot-pi*dt*D(i)^2*h*(T(i)-Tgas)/(m*cpdrop);
    %
    % Ratio of Radiative to Convective Terms
    radconv(i)=e*sb*T(i)^4/(h*(T(i)-Tgas));
    %
    % Time Update
    t(i+1)=t(i)+dt;
    %
    % Index Update
    i=i+1;
    %
else
    if P~=0
        % Gas Properties
        rhogas=P*gasprop(gas,1)/101325;
        ugas=gasprop(gas,2);
        kgas=gasprop(gas,3);
        Prgas=gasprop(gas,5);
        % Gas Reynolds Number
        Regas=abs(rhogas*v(i)*D(i)/ugas);
        %
        % Drag Coefficient
        if Regas~=0
            Cd(i)=0.28+6*Regas^(-0.5)+21/Regas;
        else
            Cd(i)=0;
        end
        %
        % Convective Heat Transfer Coefficient evaluated with Ranz-Marshall Equation
        h=kgas*(2+0.6*Regas^(1/2)*Prgas^(1/3))/D(i);
        %
        % Check Lumped Capacitance Validity with Biot Number (takes Radiation and Convection
into account)
        Bi=(h+e*sb*T(i)^3)*D(i)/kdrop;
        if Bi>0.1
            lumpflag=1;
        end
        if Bi>Bimax
```

82

```
        Bimax=Bi;
end
%
% Calculation of Force on Droplet and Droplet Acceleration
a=g+Cd(i)*rhogas*pi*D(i)^2*v(i)^2/(8*m);
%
% Calculation of New Droplet Height via Three Term Taylor Series
z(i+1)=z(i)+v(i)*dt+a*dt^2/2;
%
% Check for Impaction
if z(i+1)<0
        hitflag=1;
end
%
% Calculation of New Droplet Velocity via Runge-Kutta Integration
kn1=a;
vkn2=v(i)+kn1*dt/2;
Rekn2=abs(rhogas*vkn2*D(i)/ugas);
if Rekn2~=0
        Cdkn2=0.28+6*Rekn2^(-0.5)+21/Rekn2;
else
        Cdkn2=0;
end
kn2=g+Cdkn2*rhogas*pi*D(i)^2*vkn2^2/(8*m);
vkn3=v(i)+kn2*dt/2;
Rekn3=abs(rhogas*vkn3*D(i)/ugas);
if Rekn3~=0
        Cdkn3=0.28+6*Rekn3^(-0.5)+21/Rekn3;
else
        Cdkn3=0;
end
kn3=g+Cdkn3*rhogas*pi*D(i)^2*vkn3^2/(8*m);
vkn4=v(i)+kn3*dt;
Rekn4=abs(rhogas*vkn4*D(i)/ugas);
if Rekn4~=0
        Cdkn4=0.28+6*Rekn4^(-0.5)+21/Rekn4;
else
        Cdkn4=0;
end
kn4=g+Cdkn4*rhogas*pi*D(i)^2*vkn4^2/(8*m);
v(i+1)=v(i)+dt*(kn1+2*kn2+2*kn3+kn4)/6;
%
% Calculation of Droplet Temperature via Runge-Kutta Integration
kn1=-pi*D(i)^2*(h*(T(i)-Tgas)+e*sb*T(i)^4)/(m*cpdrop);
Tkn2=T(i)+kn1*dt/2;
kn2=-pi*D(i)^2*(h*(Tkn2-Tgas)+e*sb*Tkn2^4)/(m*cpdrop);
Tkn3=T(i)+kn2*dt/2;
kn3=-pi*D(i)^2*(h*(Tkn3-Tgas)+e*sb*Tkn3^4)/(m*cpdrop);
Tkn4=T(i)+kn3*dt;
kn4=-pi*D(i)^2*(h*(Tkn4-Tgas)+e*sb*Tkn4^4)/(m*cpdrop);
T(i+1)=T(i)+dt*(kn1+2*kn2+2*kn3+kn4)/6;
%
% Separate Radiative and Convective Losses
dTradtot=dTradtot-pi*dt*D(i)^2*e*sb*T(i)^4/(m*cpdrop);
dTcontot=dTcontot-pi*dt*D(i)^2*h*(T(i)-Tgas)/(m*cpdrop);
```

```
        %
        % Ratio of Radiative to Convective Terms
        radconv(i)=e*sb*T(i)^4/(h*(T(i)-Tgas));
        %
        % Time Update
        t(i+1)=t(i)+dt;
        %
        % Index Update
        i=i+1;
        %
    else
        % Check Lumped Capacitance Validity with Biot Number (takes Radiation and Convection
into account)
        Bi=e*sb*T(i)^3*D(i)/kdrop;
        if Bi>0.1
            lumpflag=1;
        end
        if Bi>Bimax
            Bimax=Bi;
        end
        %
        % Calculation of Force on Droplet and Droplet Acceleration
        a=g;
        %
        % Calculation of New Droplet Height via Three Term Taylor Series
        z(i+1)=z(i)+v(i)*dt+a*dt^2/2;
        %
        % Check for Impaction
        if z(i+1)<0
            hitflag=1;
        end
        %
        % Calculation of New Droplet Velocity
        v(i+1)=v(i)+g*dt;
        %
        % Calculation of Droplet Temperature via Runge-Kutta Integration
        kn1=-pi*D(i)^2*e*sb*T(i)^4/(m*cpdrop);
        Tkn2=T(i)+kn1*dt/2;
        kn2=-pi*D(i)^2*e*sb*Tkn2^4/(m*cpdrop);
        Tkn3=T(i)+kn2*dt/2;
        kn3=-pi*D(i)^2*e*sb*Tkn3^4/(m*cpdrop);
        Tkn4=T(i)+kn3*dt;
        kn4=-pi*D(i)^2*e*sb*Tkn4^4/(m*cpdrop);
        T(i+1)=T(i)+dt*(kn1+2*kn2+2*kn3+kn4)/6;
        %
        % Time Update
        t(i+1)=t(i)+dt;
        %
        % Index Update
        i=i+1;
        %
    end
    end
end
%
```

```
D(i)=D(i-1);
% Impact Velocity
vi=v(i)
% Impact Temperature
Ti=T(i)
% Metal Reynolds Number
Redrop=abs(rhodrop*v(i)*D(i)/udrop)
% Metal Weber Number
Wedrop=rhodrop*v(i)^2*D(i)/sdrop
% Metal Froude Number
Frdrop=abs(v(i)^2/(D(i)*g))
```

A1.2 Begin.m

```
% Matlab m-file Script for Input of Thermophysical Properties and Calculation of Dimensionless Numbers
% User-Specified or Default (Co or Ni on Cu)
%
% Inputs
================================================================================
D=input('Enter Diameter of Droplet [m] ');
R=D/2;                                                      % Droplet Radius [m]
v=input('Enter Impact Velocity of Droplet [m/s] ');
propflag=input('Thermophysical Properties Flag: 1=Co on Cu 2=Ni on Cu 3=Maunally Enter ');
if propflag==1
        % Cobalt Droplet on Copper Substrate
        Td=input('Enter Droplet Impact Temperature [K] ');
        Tm=1766;
        % Metal Properties
        k=2.45*Td/(0.0612*Td-6);
        rho=7750-1.09*(Td-Tm);
        cp=685;
        mu=2.55e-4*exp(4.44e4/(8.314*Td));
        sigma=1.873-4.9e-4*(Td-Tm);
        k1=42.5;
        rho1=7760;
        cp1=974;
        k2=400;
        rho2=8960;
        cp2=385;
        hf=2.747e5;
        Ts=300;
elseif propflag==2
        % Nickel Droplet on Copper Substrate
        Td=input('Enter Droplet Impact Temperature [K] ');
        Tm=1727;
        k=2.45*Td/(0.0127*Td+63);
        rho=7900-1.19*(Td-Tm);
        cp=656;
        mu=1.663e-4*exp(5.02e4/(8.314*Td));
        sigma=1.778-3.8e-4*(Td-Tm);
        k1=87.5;
        rho1=8280;
        cp1=650;
        k2=400;
```

85

```
            rho2=8960;
            cp2=385;
            hf=2.93e5;
            Ts=300;
elseif propflag==3
            Td=input('Enter Droplet Impact Temperature [K] ');
            Tm=input('Enter Melting Temperature [K] ');
            k=input('Enter Thermal Conductivity of Liquid [W/mK] ');
            rho=input('Enter Density of Liquid [kg/m3] ');
            cp=input('Enter Heat Capacity of Liquid [J/kgK] ');
            mu=input('Enter Viscosity of Liquid [kg/m s] ');
            sigma=input('Enter Surface Tension of Liquid [N/m] ');
            k1=input('Enter Thermal Conductivity of Solid [W/mK] ');
            rho1=input('Enter Density of Solid [kg/m3] ');
            cp1=input('Enter Heat Capacity of Solid [J/kgK] ');
            k2=input('Enter Thermal Conductivity of Substrate [W/mK] ');
            rho2=input('Enter Density of Substrate [kg/m3] ');
            cp2=input('Enter Heat Capacity of Substrate [J/kgK] ');
            hf=input('Enter Latent Heat of Fusion [J/kg] ');
            Ts=input('Enter Substrate Temperature [K] ');
end
%
h=input('Enter Interfacial Heat Transfer Coefficient [W/m2K] ');
%
% Dimensionless Groups
Re=rho*v*D/mu                                               % Reynolds Number
We=rho*v^2*D/sigma                                          % Weber Number
rhoratio=rho1/rho                                   % Solid/Liquid Density Ratio
% Dimensionless Thermal Resistances - Compared to Interface
n1=h*sqrt(2*pi*R/(k*rho*cp*v))                                     % Liquid
n2=2*R*h/k1                                                         % Solid
n3=h*sqrt(2*pi*R/(k2*rho2*cp2*v))                               % Substrate
% Freezing Velocity / Heat Flow Dimensionless Ratio
N4=h*(Td-Ts)/(rho*hf*v)
% Dimensionless Temperature Difference
N5=(Tm-Ts)/(Td-Ts)
```

A1.3 Freeze.m

```
% Matlab m-file Script to Calculate Transient Temperature Distribution
%       as Liquid Flows Over Substrate
% Used to Find Solidification Delay Time
% To Be Run After begin.m
%
% Initial Conditions
i=1;
t=0;
tstop=input('Enter Dimensionless Stop Time ');
dt=input('Enter Dimensionless Time Step ');
Ti=Td;                              % Initial Liquid-Side Interface Temperature
Ti1=Ts;                             % Initial Substrate-Side Interface Temperature
solflag=0;
timeflag=0;
Z=0;                                               % Frozen Thickness
```

```matlab
%
% Evaluate Freezing Constant for Madjeski Analytic Solution
U=heatiter([rho k1 rho1 cp1 k2 rho2 cp2 hf Tm Ts 1e-4 1]);
%
while (solflag==0)&(timeflag==0)
    % Dimensionless Heat Flux (Compared to Maximum)
    Q(i)=(n1*t(i)^0.5+1+n3*t(i)^0.5)^(-1);
    %
    % Updates
    t(i+1)=t(i)+dt;
    Z(i+1)=0;
    Ti(i+1)=Td-n1*(Td-Ts)*Q(i)*t(i)^0.5;
    Ti1(i+1)=Ts+n3*(Td-Ts)*Q(i)*t(i)^0.5;
    %
    % Check for Beginning of Freezing
    if Ti(i+1)<=Tm
        solflag=1;
    end
    %
    % Check for End of Time
    if t(i+1)>=tstop
        timeflag=1;
    end
    %
    % Update Iteration Index
    i=i+1;
    %
    % Analytic Models for Comparison
    Zmadj(i)=U*sqrt(2*k1*R*t(i)/(rho1*cp1*v))/R;
    ZGP(i)=k2*rho2*cp2*(Tm-Ts)*(h*sqrt(2*pi*R*t(i)/(k2*rho2*cp2*v))
    -log(1+h*sqrt(2*pi*R*t(i) /(k2*rho2*cp2*v))))/(pi*h*rho*hf*R);
end
ts=t(i);
Is=i;
%
solflag=0;
% Repeat Loop. Now With Solid Layer as Well
while timeflag==0
    % Dimensionless Heat Flux (Compared to Maximum)
    Q(i)=(n1*t(i)^0.5+n2*Z(i)+1+n3*t(i)^0.5)^(-1);
    %
    % Updates
    t(i+1)=t(i)+dt;
    Z(i+1)=Z(i)+N4*Q(i)*dt;
    Ti(i+1)=Tm-n2*(Td-Ts)*Z(i)*Q(i);
    Ti1(i+1)=Ts+n3*(Td-Ts)*Q(i)*t(i)^0.5;
    %
    % Check for End of Time
    if t(i+1)>=tstop
        timeflag=1;
    end
    %
    % Analytic Models for Comparison
    Zmadj(i)=U*sqrt(2*k1*R*t(i)/(rho1*cp1*v))/R;
    ZGP(i)=k2*rho2*cp2*(Tm-Ts)*(h*sqrt(2*pi*R*t(i)/(k2*rho2*cp2*v))
```

```matlab
        -log(1+h*sqrt(2*pi*R*t(i)/(k2*rho2*cp2*v))))/(pi*h*rho*hf*R);
    %
    % Update Iteration Index
        i=i+1;
end
t=t(1:i-1);
Z=Z(1:i-1);
Rliq=n1.*sqrt(t(1:Is));
Rsol=n2.*Z;
Rsub=n3.*sqrt(t);
```

A1.4 Splat.m

```matlab
% Matlab m-file to Simulate Oscillatory Spreading Motion
% To be run after begin.m, freeze.m
%
% Inputs
ts=input('Enter Dimensionless Delay Time ');
tstop=input('Enter Dimensionless Stop Time ');
dt=input('Enter Dimensionless Time Step ');
x=input('Enter Initial Spreading Extent ');
%
% Initial Conditions
t=0;                                              % Initial Time
I=1;                                              % Iteration Index
xs=0;                                             % Initial Solidification Front
Z=0;                                              % Frozen Thickness
fs=0;                                             % Fraction Solid
Is=1;                                             % Index of Time Step When Solidification Starts
% Initial Spreading Rate
dxdt=sqrt(4+48/We-24*x^2/We-32/(We*x));
viscsum=0;                                        % Sum Term for Integration of Viscous Losses
solsum=0                                          % Sum Term for Integration of Solidification Losses
solflag=0                                         % Solidification Flag
timeflag=0                                        % End Time Flag
expflag=0                                         % Solid Exposure Flag
rev=0                                             % Number of Flow Reversals
dampflag=0                                        % Flag Signifying Fully Damped Oscillation
tol=1e-2                                          % Tolerance for Damping
start=0                                           % Flag Signifying Solidification Start
flag10=0                                          % Flags for Progress Updates
flag20=0;
flag30=0;
flag40=0;
flag50=0;
flag60=0;
flag70=0;
flag80=0;
flag90=0;
%
% Calculational Loop
while (timeflag==0)&(solflag==0)&(rev<2)&(dampflag==0)
    dZdt(i)=((n2/(N4*N5))*Z(i)+1/(N4*N5)+(n3/(N4*N5))*(t(i)+ts)^0.5)^(-1);
    % Find index, Is, Corresponding to Solid Start Time, ts
```

88

```
if start==0
        % Solidification Hasn't Started Yet
        if t(i)>ts
                start=1;
                if (ts-t(i-1))<(t(i)-ts)
                        Is=i-1;
                else
                        Is=i;
                end
        end
        dfsdt(i)=0;
else
        % Solidification Has Started
        if ~expflag
                % No Solid Exposed Yet
                if i==Is+1
                        % First Step After Solidification Starts
                        dfsdt(i)=1.5*rhoratio*x(1)^2*dZdt(i-Is);
                else
                        dfsdt(i)=1.5*rhoratio*(x(1)^2*dZdt(i-Is)+2*dt*(dZdt(1:i-Is-1).*fliplr(x(1:i-Is-
1))*fliplr(dxdt(1:i-Is-1))')));
                end
        else
                % Some Solid is Exposed
                if x(i)>x(1)
                        % Spreading Extent Still Greater Than Initial
                        % Find index, I1, Corresponding to First Time at This Radius
                        I1flag=0;
                        j=0;
                        while I1flag==0;
                                j=j+1;
                                if x(i)<=x(j)
                                        I1flag=1;
                                        if abs(x(j)-x(i))<abs(x(j-1)-x(i))
                                                I1=j;
                                        else
                                                I1=j-1;
                                        end
                                end
                        end
                        % Vector of x Values to Use for Fracation Solid Calc.
                        % Real Values up to where liquid covers; Zeros thereafter
                        if I1<=Ir-Is-1
                                xfs=x(1:I1);
                                xfs(Ir-Is-1)=0;
                        elseif I1==Ir-Is
                                xfs=x(1:I1-1);
                        end
                        dfsdt(i)=1.5*rhoratio*(x(1)^2*dZdt(i-Is)+2*dt*(dZdt(i-
Ir+Is+2:i).*fliplr(xfs)*fliplr(dxdt(1:Ir-Is-1))')));
                        clear xfs
                else
                        % Spreading Extent Less Than Initial
                        % Use fractional contact area
                        fraction=x(i)/x(1);
```

```
                    dfsdt(i)=1.5*rhoratio*fraction^2*x(1)^2*dZdt(i-Is);
                end
            end
        end
%
% Dimensionless Kinetic Energy
Ek(i)=dxdt(i)^2/(4/(1-fs(i))+48/(We*(1-fs(i))));
% Dimensionless Kinetic Energy Lost to Solidification
Esol(i)=solsum(i)/(4+48/We);
% Dimensionless Viscous Losses
Lf(i)=viscsum(i)/(8*Re/9+32*Re/(3*We));
% Dimensionless Surface Energy
liqtop(i)=x(i)^2;
liqside(i)=8*(1-fs(i))/(3*x(i));
if i>Is
        solbot(i)=xs(i)^2;
        if expflag
            % Has Solid Top, Solid-Induced Liquid Side: Needs Solid Side
            soltop(i)=xs(i)^2-x(i)^2;
            liqsol(i)=4*dt*xs(1:Ir-Is)*fliplr(dZdt(1:Ir-Is))';
            liqbot(i)=0;
        else
            soltop(i)=0;
            liqsol(i)=4*dt*x(1:i-Is)*fliplr(dZdt(1:i-Is))';
            liqbot(i)=x(i)^2-xs(i)^2;
        end
else
        soltop(i)=0;
        solbot(i)=0;
        liqsol(i)=0;
        liqbot(i)=liqtop(i);
end
Esfc(i)=(liqtop(i)+liqside(i)+liqsol(i)+liqbot(i)+soltop(i)+solbot(i))/(We/3+4);
%
% Integration of All Quantities
% Runge-Kutta Integration of d2xdt2 = Rate of Change of Spreading Rate
        if (start)&(i>Is)
            if x(i)>xs(i)
                d2xdt2(i)=-24*x(i)/(We*(1-fs(i)))+16/(We*x(i)^2)-24*Z(i-Is)/(We*(1-fs(i)))-
9*x(i)^4*dxdt(i)/(4*Re*(1-fs(i))^2);
                kn1=-24*x(i)/(We*(1-fs(i)))+16/(We*x(i)^2)-24*Z(i-Is)/(We*(1-fs(i)))-
9*x(i)^4*dxdt(i)/(4*Re*(1-fs(i))^2);
            else
                d2xdt2(i)=16/(We*x(i)^2)-24*Z(i-Is)/(We*(1-fs(i)))-9*x(i)^4*dxdt(i)/(4*Re*(1-
fs(i))^2);
                kn1=16/(We*x(i)^2)-24*Z(i-Is)/(We*(1-fs(i)))-9*x(i)^4*dxdt(i)/(4*Re*(1-fs(i))^2);
            end
        else
            d2xdt2(i)=-24*x(i)/(We*(1-fs(i)))+16/(We*x(i)^2)-9*x(i)^4*dxdt(i)/(4*Re*(1-fs(i))^2);
            kn1=-24*x(i)/(We*(1-fs(i)))+16/(We*x(i)^2)-9*x(i)^4*dxdt(i)/(4*Re*(1-fs(i))^2);
        end
        xkn2=x(i)+dxdt(i)*dt/2;
        fskn2=fs(i)+dfsdt(i)*dt/2;
        dxdtkn2=dxdt(i)+kn1*dt/2;
        if (start)&(i>Is)
```

```
        if x(i)>xs(i)
            kn2=-24*xkn2/(We*(1-fskn2))+16/(We*xkn2^2)-24*Z(i-Is)/(We*(1-fs(i)))-
9*xkn2^4*dxdtkn2/(4*Re*(1-fskn2)^2);
        else
            kn2=16/(We*xkn2^2)-24*Z(i-Is)/(We*(1-fs(i)))-9*xkn2^4*dxdtkn2/(4*Re*(1-
fskn2)^2);
        end
    else
        kn2=-24*xkn2/(We*(1-fskn2))+16/(We*xkn2^2)-9*xkn2^4*dxdtkn2/(4*Re*(1-fskn2)^2);
    end
    xkn3=xkn2;
    fskn3=fskn2;
    dxdtkn3=dxdt(i)+kn2*dt/2;
    if (start)&(i>Is)
        if x(i)>xs(i)
            kn3=-24*xkn3/(We*(1-fskn3))+16/(We*xkn3^2)-24*Z(i-Is)/(We*(1-fs(i)))-
9*xkn3^4*dxdtkn3/(4*Re*(1-fskn3)^2);
        else
            kn3=16/(We*xkn3^2)-24*Z(i-Is)/(We*(1-fs(i)))-9*xkn3^4*dxdtkn3/(4*Re*(1-
fskn3)^2);
        end
    else
        kn3=-24*xkn3/(We*(1-fskn3))+16/(We*xkn3^2)-9*xkn3^4*dxdtkn3/(4*Re*(1-fskn3)^2);
    end
    xkn4=x(i)+dxdt(i)*dt;
    fskn4=fs(i)+dfsdt(i)*dt;
    dxdtkn4=dxdt(i)+kn3*dt;
    if (start)&(i>Is)
        if x(i)>xs(i)
            kn4=-24*xkn4/(We*(1-fskn4))+16/(We*xkn4^2)-24*Z(i-Is)/(We*(1-fs(i)))-
9*xkn4^4*dxdtkn4/(4*Re*(1-fskn4)^2);
        else
            kn4=16/(We*xkn4^2)-24*Z(i-Is)/(We*(1-fs(i)))-9*xkn4^4*dxdtkn4/(4*Re*(1-
fskn4)^2);
        end
    else
        kn4=-24*xkn4/(We*(1-fskn4))+16/(We*xkn4^2)-9*xkn4^4*dxdtkn4/(4*Re*(1-fskn4)^2);
    end
    dxdt(i+1)=dxdt(i)+dt*(kn1+2*kn2+2*kn3+kn4)/6;
% Three Term Taylor Series Integration of x
    x(i+1)=x(i)+dxdt(i)*dt+d2xdt2(i)*dt^2/2;
% Solidification Front
    if expflag
        xs(i+1)=Xs;
    elseif (start==0)|(i<=Is+1)
        xs(i+1)=0;
    else
        xs(i+1)=x(i-Is);
    end
% Runge-Kutta Integration of Z
    kn1=((n2/(N4*N5))*Z(i)+1/(N4*N5)+(n3/(N4*N5))*(t(i)+ts)^0.5)^(-1);
    kn2=((n2/(N4*N5))*(Z(i)+kn1*dt/2)+1/(N4*N5)+(n3/(N4*N5))*(t(i)+ts+dt/2)^0.5)^(-1);
    kn3=((n2/(N4*N5))*(Z(i)+kn2*dt/2)+1/(N4*N5)+(n3/(N4*N5))*(t(i)+ts+dt/2)^0.5)^(-1);
    kn4=((n2/(N4*N5))*(Z(i)+kn3*dt)+1/(N4*N5)+(n3/(N4*N5))*(t(i)+ts+dt)^0.5)^(-1);
    Z(i+1)=Z(i)+dt*(kn1+2*kn2+2*kn3+kn4)/6;
```

```
% Euler Integration of fs
    fs(i+1)=fs(i)+dfsdt(i)*dt;
% Viscous Losses Integral
    viscsum(i+1)=viscsum(i)+x(i)^4*dxdt(i)^2*dt/(1-fs(i));
% Kinetic Energy Losses Due to Solidification
    solsum(i+1)=solsum(i)+dxdt(i)^2*dfsdt(i)*dt;
% Time
    t(i+1)=t(i)+dt;
    if t(i+1)>tstop
        stopflag=1;
    end
% Check for Exposed Solid
    if (x(i+1)<=xs(i+1))&(expflag==0)
        expflag=1;
        Ir=i;
        Xs=xs(i+1);
    end
% Check for Completeness
    if t(i+1)>=tstop
        timeflag=1;
    end
% Solidification Check
    if fs(i+1)>=1
        solflag=1;
    end
% Check for Complete Damping
    if (abs(d2xdt2(i))<tol)&(abs(dxdt(i+1))<tol)
        dampflag=1;
    end
% Check for Flow Reversal
    if sign(dxdt(i+1))~=sign(dxdt(i))
        rev=rev+1;
    end
% Periodic Time Checks Displayed
    if (t(i+1)>0.1*tstop)&~flag10
        flag10=1
    elseif (t(i+1)>0.2*tstop)&~flag20
        flag20=1
    elseif (t(i+1)>0.3*tstop)&~flag30
        flag30=1
    elseif (t(i+1)>0.4*tstop)&~flag40
        flag40=1
    elseif (t(i+1)>0.5*tstop)&~flag50
        flag50=1
    elseif (t(i+1)>0.6*tstop)&~flag60
        flag60=1
    elseif (t(i+1)>0.7*tstop)&~flag70
        flag70=1
    elseif (t(i+1)>0.8*tstop)&~flag80
        flag80=1
    elseif (t(i+1)>0.9*tstop)&~flag90
        flag90=1
    end
% Update Iteration Index
    i=i+1;
```

end

APPENDIX 2 - TABULAR TRANSIENT SPREADING DATA

Appendix 2 contains tabular transient spreading data obtained directly from image processing of the splat photographs. Plots of the data are also included in Figures 32-42 for a visual representation of those experiments not discussed.

A2.1 ID# 319_1

frame #	t[ms]	τ	ξ	βctr	βother	βmax
528	0.00	0.00	0.00	1.06	0.00	1.06
529	0.22	0.05	0.20	1.02	0.00	1.02
530	0.44	0.10	0.52	0.98	0.00	0.98
531	0.67	0.15	0.74	0.94	0.00	0.94
532	0.89	0.20	0.94	0.90	0.00	0.90
533	1.11	0.24	1.10	0.88	0.00	0.88
534	1.33	0.29	1.27	0.84	0.00	0.84
535	1.56	0.34	1.43	0.82	0.00	0.82
536	1.78	0.39	1.51	0.80	0.00	0.80
537	2.00	0.44	1.62	0.76	0.00	0.76
538	2.22	0.49	1.77	0.68	0.00	0.68
539	2.44	0.54	1.81	0.70	0.00	0.70
540	2.67	0.59	1.91	0.66	0.00	0.66
541	2.89	0.63	2.01	0.62	0.00	0.62
542	3.11	0.68	2.07	0.58	0.00	0.58
543	3.33	0.73	2.13	0.54	0.00	0.54
545	3.78	0.83	2.31	0.44	0.00	0.44
547	4.22	0.93	2.41	0.36	0.00	0.36
549	4.67	1.02	2.53	0.38	0.00	0.38
551	5.11	1.12	2.63	0.24	0.00	0.24
553	5.56	1.22	2.72	0.24	0.28	0.28
555	6.00	1.32	2.80	0.24	0.30	0.30
560	7.11	1.56	3.01	0.30	0.38	0.38
565	8.22	1.80	3.13	0.30	0.40	0.40
570	9.33	2.05	3.19	0.30	0.42	0.42
575	10.44	2.29	3.13	0.32	0.42	0.42
580	11.56	2.54	3.16	0.34	0.44	0.44
590	13.78	3.02	2.99	0.28	0.46	0.46
600	16.00	3.51	2.88	0.28	0.48	0.48
610	18.22	4.00	2.84	0.26	0.44	0.44
620	20.44	4.49	2.70	0.26	0.40	0.40
630	22.67	4.97	2.51	0.32	0.38	0.38
640	24.89	5.46	2.41	0.36	0.38	0.38

650	27.11	5.95	2.35	0.28	0.36	0.36
660	29.33	6.44	2.45	0.32	0.38	0.38
670	31.56	6.92	2.45	0.54	0.00	0.54
680	33.78	7.41	2.41	0.66	0.00	0.66
690	36.00	7.90	2.43	0.74	0.00	0.74
700	38.22	8.39	2.43	0.74	0.00	0.74
710	40.44	8.87	2.43	0.78	0.00	0.78
720	42.67	9.36	2.37	0.75	0.00	0.75
730	44.89	9.85	2.39	0.70	0.00	0.70
740	47.11	10.34	2.39	0.60	0.00	0.60
750	49.33	10.83	2.39	0.44	0.00	0.44
760	51.56	11.31	2.37	0.36	0.36	0.36
770	53.78	11.80	2.37	0.30	0.32	0.32
780	56.00	12.29	2.41	0.28	0.32	0.32
790	58.22	12.78	2.39	0.30	0.30	0.30
800	60.44	13.26	2.37	0.32	0.32	0.32

Figure 32: ID# 319_1
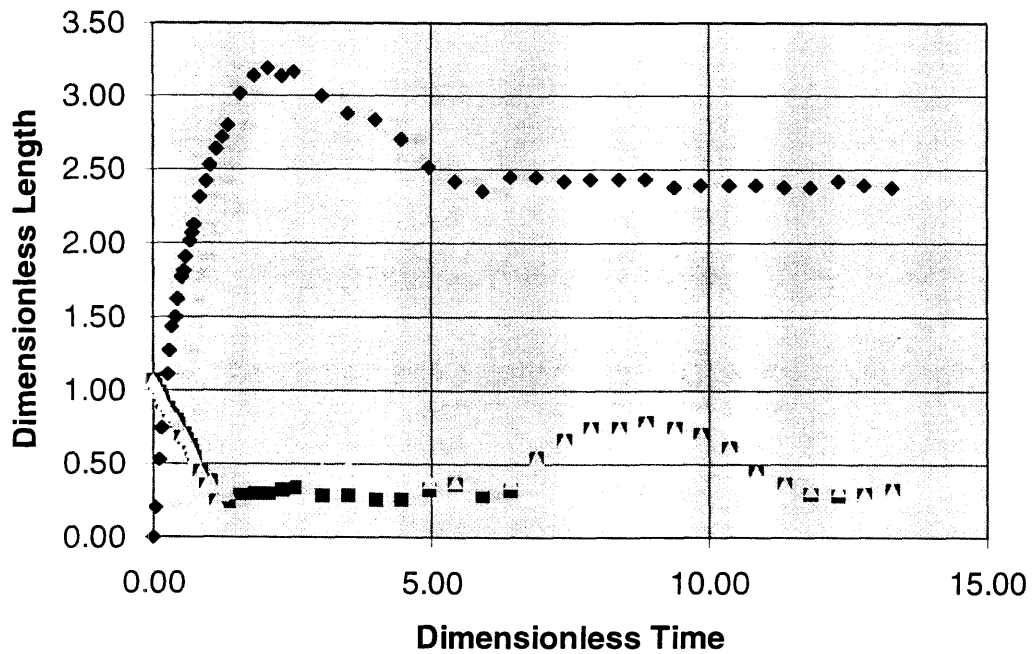
A2.2 ID# 319_2

frame #	t[ms]	τ	ξ	βctr	βother	βmax
951	0.00	0.00	0.00	0.99	0.00	0.99
952	0.22	0.05	0.34	0.96	0.00	0.96
953	0.44	0.10	0.70	0.89	0.00	0.89
954	0.67	0.16	0.89	0.89	0.00	0.89
955	0.89	0.21	1.07	0.83	0.00	0.83
956	1.11	0.26	1.28	0.78	0.00	0.78
957	1.33	0.31	1.38	0.73	0.00	0.73
958	1.56	0.36	1.55	0.69	0.00	0.69
959	1.78	0.41	1.66	0.58	0.00	0.58
960	2.00	0.47	1.78	0.58	0.00	0.58
961	2.22	0.52	1.91	0.56	0.00	0.56
962	2.44	0.57	1.98	0.53	0.00	0.53
963	2.67	0.62	2.03	0.51	0.00	0.51
964	2.89	0.67	2.13	0.48	0.00	0.48
965	3.11	0.72	2.24	0.43	0.00	0.43
966	3.33	0.78	2.31	0.43	0.00	0.43
968	3.78	0.88	2.47	0.38	0.00	0.38
970	4.22	0.98	2.61	0.36	0.00	0.36
972	4.67	1.09	2.70	0.38	0.00	0.38
974	5.11	1.19	2.79	0.41	0.00	0.41
976	5.56	1.29	2.87	0.38	0.00	0.38
978	6.00	1.40	2.97	0.38	0.00	0.38
980	6.44	1.50	3.02	0.25	0.00	0.25
985	7.56	1.76	3.18	0.26	0.00	0.26
990	8.67	2.02	3.36	0.26	0.00	0.26
995	9.78	2.28	3.46	0.23	0.00	0.23
1000	10.89	2.54	3.51	0.21	0.00	0.21
1005	12.00	2.79	3.10	0.21	0.00	0.21
1010	13.11	3.05	3.10	0.21	0.00	0.21
1015	14.22	3.31	3.10	0.16	0.00	0.16
1020	15.33	3.57	3.07	0.16	0.00	0.16

Figure 33: ID# 319_2
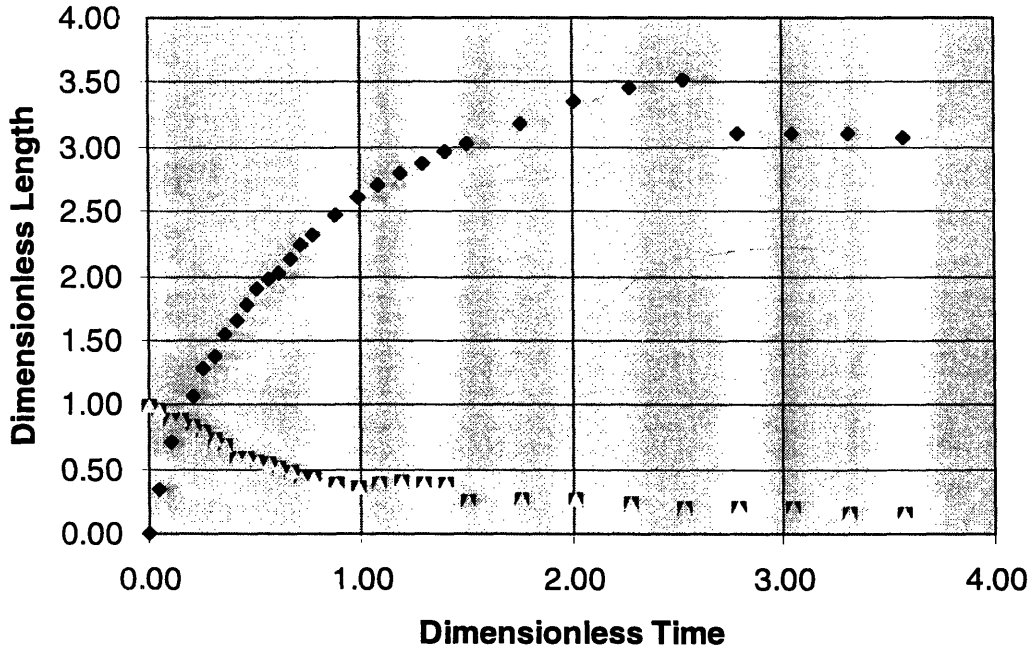
A2.3 ID# 319_3

frame #	t[ms]	τ	ξ	βctr	βother	βmax
732	0.00	0.00	0.00	0.97	0.00	0.97
733	0.22	0.05	0.30	1.03	0.00	1.03
734	0.44	0.09	0.57	0.99	0.00	0.99
735	0.67	0.14	0.85	0.95	0.00	0.95
736	0.89	0.18	1.04	0.91	0.00	0.91
737	1.11	0.23	1.19	0.87	0.00	0.87
738	1.33	0.27	1.37	0.83	0.00	0.83
739	1.56	0.32	1.49	0.81	0.00	0.81
740	1.78	0.37	1.59	0.77	0.00	0.77
741	2.00	0.41	1.72	0.75	0.00	0.75
742	2.22	0.46	1.84	0.69	0.00	0.69
743	2.44	0.50	1.96	0.65	0.00	0.65
745	2.89	0.60	2.12	0.59	0.00	0.59
747	3.33	0.69	2.28	0.55	0.00	0.55
749	3.78	0.78	2.45	0.49	0.00	0.49
751	4.22	0.87	2.55	0.44	0.00	0.44
753	4.67	0.96	2.65	0.38	0.00	0.38
755	5.11	1.05	2.75	0.34	0.00	0.34
760	6.22	1.28	2.98	0.34	0.00	0.34
765	7.33	1.51	3.11	0.34	0.00	0.34

770	8.44	1.74	3.23	0.36	0.00	0.36
780	10.67	2.20	3.43	0.34	0.00	0.34
790	12.89	2.66	3.57	0.32	0.00	0.32
800	15.11	3.11	3.47	0.36	0.00	0.36
810	17.33	3.57	3.46	0.38	0.00	0.38
820	19.56	4.03	3.49	0.32	0.00	0.32
830	21.78	4.49	3.45	0.32	0.00	0.32
840	24.00	4.94	3.43	0.30	0.00	0.30
850	26.22	5.40	3.39	0.30	0.00	0.30
860	28.44	5.86	3.35	0.10	0.42	0.42
880	32.89	6.78	3.37	0.14	0.42	0.42
930	44.00	9.06	3.37	0.12	0.49	0.49
980	55.11	11.35	3.35	0.10	0.44	0.44

Figure 34: ID# 319_3
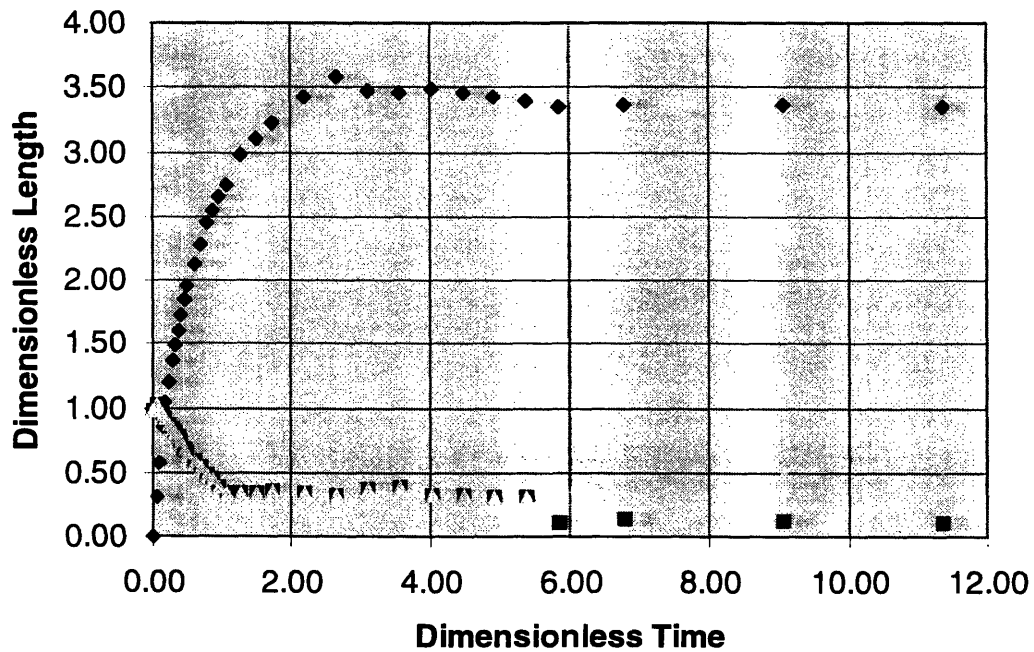
A2.4 ID# 319_4

frame #	t[ms]	τ	ξ	βctr	βother	βmax
437	0.00	0.00	0.00	1.08	0.00	1.08
438	0.22	0.05	0.37	1.04	0.00	1.04
439	0.44	0.09	0.67	0.95	0.00	0.95
440	0.67	0.14	0.86	0.95	0.00	0.95
441	0.89	0.19	1.11	0.86	0.00	0.86

442	1.11	0.24	1.23	0.86	0.00	0.86
443	1.33	0.28	1.43	0.84	0.00	0.84
444	1.56	0.33	1.57	0.78	0.00	0.78
445	1.78	0.38	1.71	0.76	0.00	0.76
446	2.00	0.43	1.80	0.67	0.00	0.67
447	2.22	0.47	1.93	0.65	0.00	0.65
448	2.44	0.52	2.03	0.61	0.00	0.61
449	2.67	0.57	2.14	0.58	0.00	0.58
450	2.89	0.62	2.18	0.54	0.00	0.54
451	3.11	0.66	2.32	0.54	0.00	0.54
452	3.33	0.71	2.41	0.50	0.00	0.50
454	3.78	0.81	2.51	0.45	0.00	0.45
456	4.22	0.90	2.64	0.39	0.00	0.39
458	4.67	1.00	2.72	0.37	0.00	0.37
460	5.11	1.09	2.85	0.00	0.00	0.00
462	5.56	1.19	2.94	0.00	0.00	0.00
464	6.00	1.28	3.03	0.00	0.00	0.00
469	7.11	1.52	3.24	0.00	0.00	0.00
474	8.22	1.76	3.39	0.00	0.00	0.00
479	9.33	1.99	3.46	0.00	0.00	0.00
489	11.56	2.47	3.64	0.00	0.00	0.00
499	13.78	2.94	3.66	0.00	0.00	0.00
509	16.00	3.42	3.61	0.00	0.00	0.00
519	18.22	3.89	3.61	0.00	0.00	0.00
529	20.44	4.36	3.61	0.00	0.00	0.00
539	22.67	4.84	3.59	0.00	0.00	0.00
549	24.89	5.31	3.50	0.00	0.00	0.00
559	27.11	5.79	3.39	0.00	0.00	0.00
569	29.33	6.26	3.27	0.00	0.00	0.00
579	31.56	6.74	3.16	0.00	0.00	0.00
589	33.78	7.21	3.12	0.48	0.00	0.48
599	36.00	7.68	3.10	0.48	0.00	0.48
619	40.44	8.63	2.99	0.45	0.00	0.45
639	44.89	9.58	3.01	0.41	0.00	0.41
659	49.33	10.53	3.05	0.00	0.00	0.00
679	53.78	11.48	3.01	0.00	0.00	0.00

Figure 35: ID# 319_4
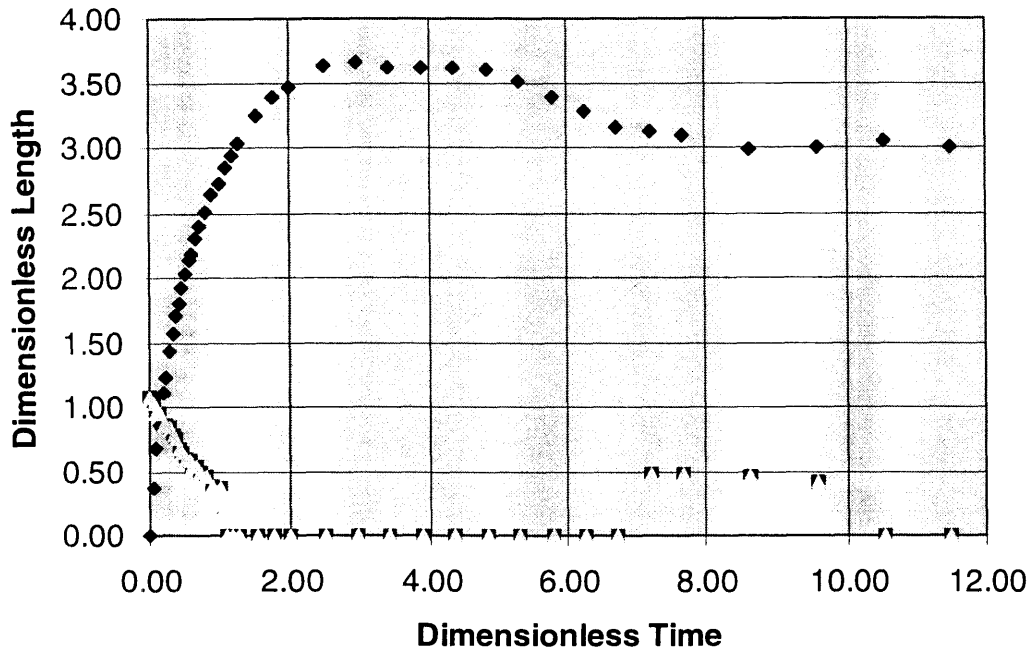
A2.5 ID# 321_1

frame #	t[ms]	τ	ξ	βctr	βother	βmax
1459	0.00	0.00	0.00	1.05	0.00	1.05
1461	0.11	0.03	0.29	1.03	0.00	1.03
1463	0.22	0.05	0.39	1.00	0.00	1.00
1465	0.33	0.08	0.56	0.98	0.00	0.98
1467	0.44	0.10	0.66	0.95	0.00	0.95
1469	0.56	0.13	0.81	0.95	0.00	0.95
1471	0.67	0.15	0.98	0.91	0.00	0.91
1473	0.78	0.18	1.10	0.88	0.00	0.88
1475	0.89	0.21	1.15	0.86	0.00	0.86
1477	1.00	0.23	1.27	0.88	0.00	0.88
1479	1.11	0.26	1.35	0.86	0.00	0.86
1481	1.22	0.28	1.42	0.81	0.00	0.81
1483	1.33	0.31	1.52	0.78	0.00	0.78
1485	1.44	0.33	1.59	0.76	0.00	0.76
1490	1.72	0.40	1.71	0.71	0.00	0.71
1495	2.00	0.46	1.93	0.68	0.00	0.68
1500	2.28	0.53	2.03	0.64	0.00	0.64
1505	2.56	0.59	2.15	0.56	0.00	0.56
1515	3.11	0.72	2.38	0.42	0.00	0.42
1525	3.67	0.85	2.50	0.32	0.00	0.32

1535	4.22	0.98	2.76	0.24	0.00	0.24
1545	4.78	1.10	2.91	0.20	0.00	0.20
1555	5.33	1.23	2.98	0.22	0.00	0.22
1565	5.89	1.36	3.08	0.15	0.00	0.15
1575	6.44	1.49	3.19	0.07	0.00	0.07
1585	7.00	1.62	3.28	0.12	0.17	0.17
1595	7.56	1.75	3.23	0.05	0.15	0.15
1605	8.11	1.87	3.25	0.07	0.15	0.15
1615	8.67	2.00	3.34	0.07	0.17	0.17
1665	11.44	2.65	3.24	0.07	0.17	0.17
1715	14.22	3.29	3.19	0.07	0.20	0.20
1765	17.00	3.93	3.19	0.07	0.29	0.29
1815	19.78	4.57	3.10	0.07	0.27	0.27
1865	22.56	5.21	3.07	0.10	0.24	0.24
1915	25.33	5.86	3.02	0.10	0.20	0.20
1965	28.11	6.50	3.19	0.10	0.15	0.15
2015	30.89	7.14	3.29	0.07	0.12	0.12
2065	33.67	7.78	3.27	0.07	0.15	0.15
2115	36.44	8.42	3.27	0.10	0.10	0.10

Figure 36: ID# 321_1
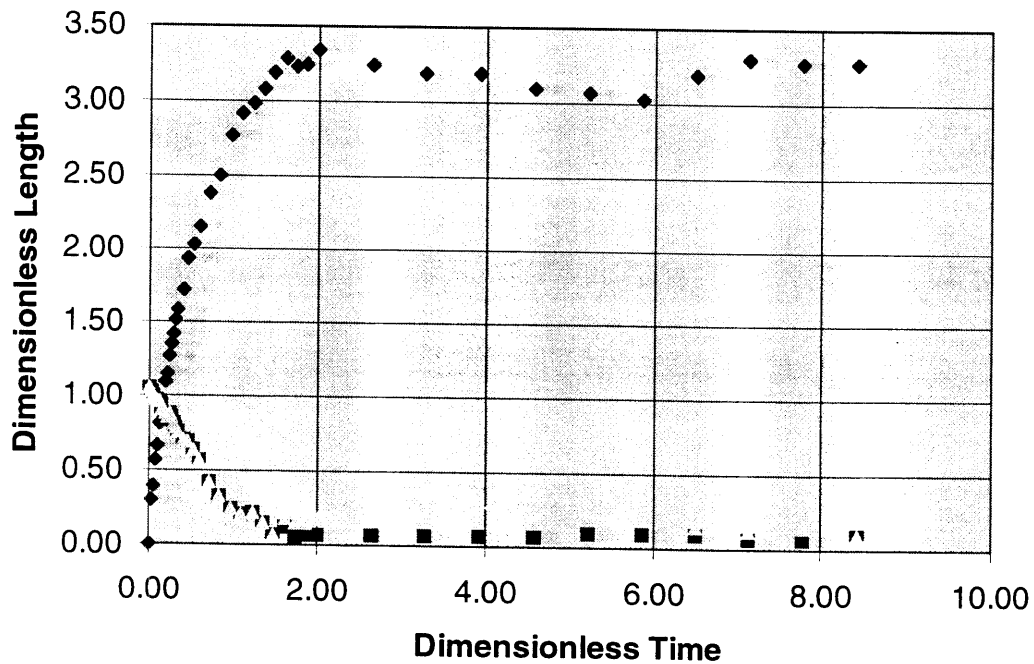
A2.6 ID# 328_1

frame #	t[ms]	τ	ξ	βctr	βother	βmax
1286	0.00	0.00	0.00	0.94	0.00	0.94
1288	0.22	0.06	0.44	0.86	0.00	0.86
1290	0.44	0.11	0.65	0.86	0.00	0.86
1292	0.67	0.17	1.06	0.80	0.00	0.80
1294	0.89	0.23	1.26	0.74	0.00	0.74
1296	1.11	0.28	1.48	0.71	0.00	0.71
1298	1.33	0.34	1.63	0.62	0.00	0.62
1300	1.56	0.40	1.74	0.56	0.00	0.56
1302	1.78	0.46	1.86	0.56	0.00	0.56
1304	2.00	0.51	2.01	0.53	0.00	0.53
1306	2.22	0.57	2.13	0.47	0.00	0.47
1308	2.44	0.63	2.21	0.41	0.00	0.41
1310	2.67	0.68	2.33	0.38	0.00	0.38
1312	2.89	0.74	2.45	0.35	0.00	0.35
1314	3.11	0.80	2.54	0.33	0.00	0.33
1316	3.33	0.85	2.66	0.27	0.00	0.27
1318	3.56	0.91	2.72	0.27	0.00	0.27
1323	4.11	1.05	2.89	0.24	0.00	0.24
1328	4.67	1.20	3.01	0.18	0.00	0.18
1338	5.78	1.48	3.19	0.09	0.15	0.15
1348	6.89	1.77	3.30	0.09	0.18	0.18
1358	8.00	2.05	3.30	0.09	0.21	0.21
1368	9.11	2.34	3.25	0.09	0.21	0.21
1378	10.22	2.62	3.16	0.09	0.18	0.18
1388	11.33	2.91	3.12	0.12	0.18	0.18
1398	12.44	3.19	3.16	0.09	0.18	0.18
1408	13.56	3.47	3.12	0.09	0.12	0.12
1418	14.67	3.76	3.16	0.09	0.18	0.18
1428	15.78	4.04	3.12	0.09	0.15	0.15
1438	16.89	4.33	3.04	0.09	0.12	0.12
1448	18.00	4.61	3.07	0.09	0.15	0.15
1458	19.11	4.90	3.01	0.12	0.18	0.18
1468	20.22	5.18	3.04	0.09	0.18	0.18
1478	21.33	5.47	2.99	0.12	0.18	0.18
1488	22.44	5.75	2.92	0.15	0.18	0.18
1498	23.56	6.04	2.77	0.15	0.18	0.18
1508	24.67	6.32	2.81	0.21	0.00	0.21
1518	25.78	6.61	2.74	0.21	0.00	0.21
1528	26.89	6.89	2.74	0.24	0.00	0.24
1538	28.00	7.18	2.81	0.24	0.00	0.24
1548	29.11	7.46	2.74	0.24	0.00	0.24
1558	30.22	7.75	2.72	0.24	0.00	0.24
1568	31.33	8.03	2.81	0.21	0.00	0.21
1618	36.89	9.46	2.77	0.15	0.00	0.15
1668	42.44	10.88	2.69	0.15	0.00	0.15

Figure 37: ID# 328_1
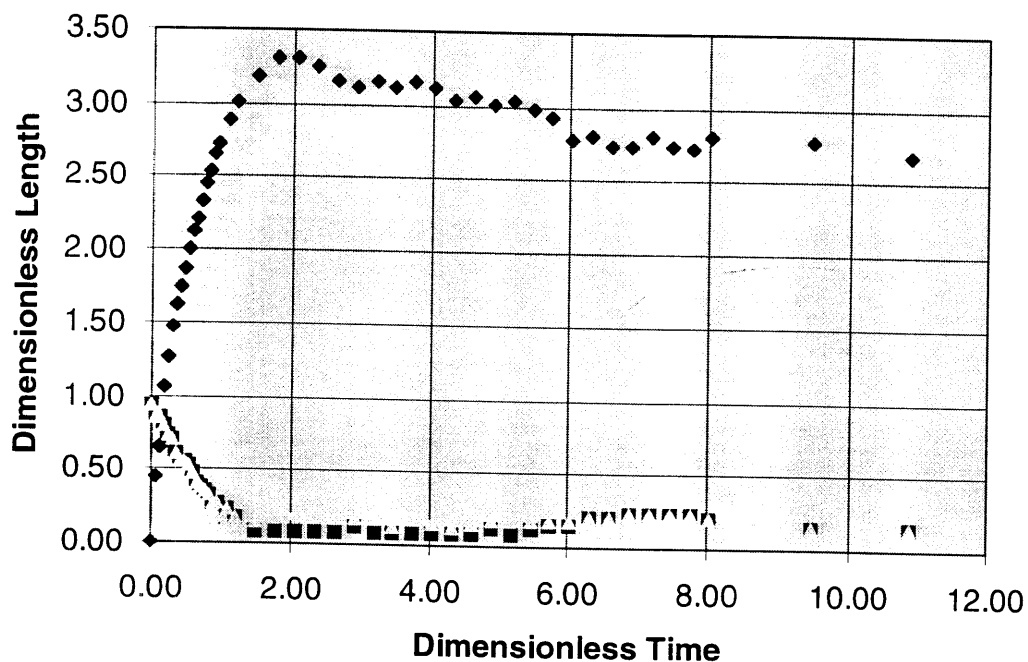
A2.7 ID# 328_2

frame #	t[ms]	τ	ξ	βctr	βother	βmax
976	0.00	0.00	0.00	0.90	0.00	0.90
978	0.22	0.06	0.51	0.84	0.00	0.84
980	0.44	0.11	0.81	0.78	0.00	0.78
982	0.67	0.17	1.23	0.75	0.00	0.75
984	0.89	0.22	1.50	0.66	0.00	0.66
986	1.11	0.28	1.68	0.63	0.00	0.63
988	1.33	0.33	1.77	0.60	0.00	0.60
990	1.56	0.39	1.98	0.57	0.00	0.57
992	1.78	0.44	2.10	0.51	0.00	0.51
994	2.00	0.50	2.22	0.51	0.00	0.51
996	2.22	0.56	2.34	0.48	0.00	0.48
998	2.44	0.61	2.44	0.45	0.00	0.45
1000	2.67	0.67	2.58	0.42	0.00	0.42
1002	2.89	0.72	2.65	0.33	0.00	0.33
1004	3.11	0.78	2.77	0.30	0.00	0.30
1006	3.33	0.83	2.83	0.30	0.00	0.30
1008	3.56	0.89	2.89	0.30	0.00	0.30
1010	3.78	0.95	2.89	0.24	0.00	0.24
1012	4.00	1.00	2.91	0.21	0.00	0.21
1014	4.22	1.06	2.97	0.21	0.00	0.21

1016	4.44	1.11	3.07	0.24	0.00	0.24
1026	5.56	1.39	3.21	0.12	0.21	0.21
1036	6.67	1.67	3.27	0.09	0.24	0.24
1046	7.78	1.95	3.27	0.12	0.24	0.24
1056	8.89	2.22	3.27	0.12	0.24	0.24
1066	10.00	2.50	3.19	0.15	0.21	0.21
1076	11.11	2.78	3.19	0.18	0.27	0.27
1086	12.22	3.06	3.19	0.15	0.27	0.27
1096	13.33	3.34	3.13	0.15	0.24	0.24
1106	14.44	3.61	3.03	0.18	0.24	0.24
1116	15.56	3.89	2.91	0.15	0.24	0.24
1126	16.67	4.17	2.85	0.12	0.24	0.24
1136	17.78	4.45	2.85	0.12	0.18	0.18
1146	18.89	4.73	2.83	0.12	0.24	0.24
1156	20.00	5.00	2.76	0.15	0.24	0.24
1166	21.11	5.28	2.79	0.18	0.24	0.24
1176	22.22	5.56	2.82	0.21	0.00	0.21
1186	23.33	5.84	2.79	0.21	0.39	0.39
1196	24.44	6.12	2.76	0.21	0.42	0.42
1206	25.56	6.39	2.67	0.39	0.00	0.39
1216	26.67	6.67	2.70	0.36	0.00	0.36
1226	27.78	6.95	2.70	0.36	0.00	0.36
1276	33.33	8.34	2.50	0.27	0.00	0.27
1326	38.89	9.73	2.70	0.21	0.00	0.21
1376	44.44	11.12	2.46	0.18	0.00	0.18

Figure 38: ID# 328_2
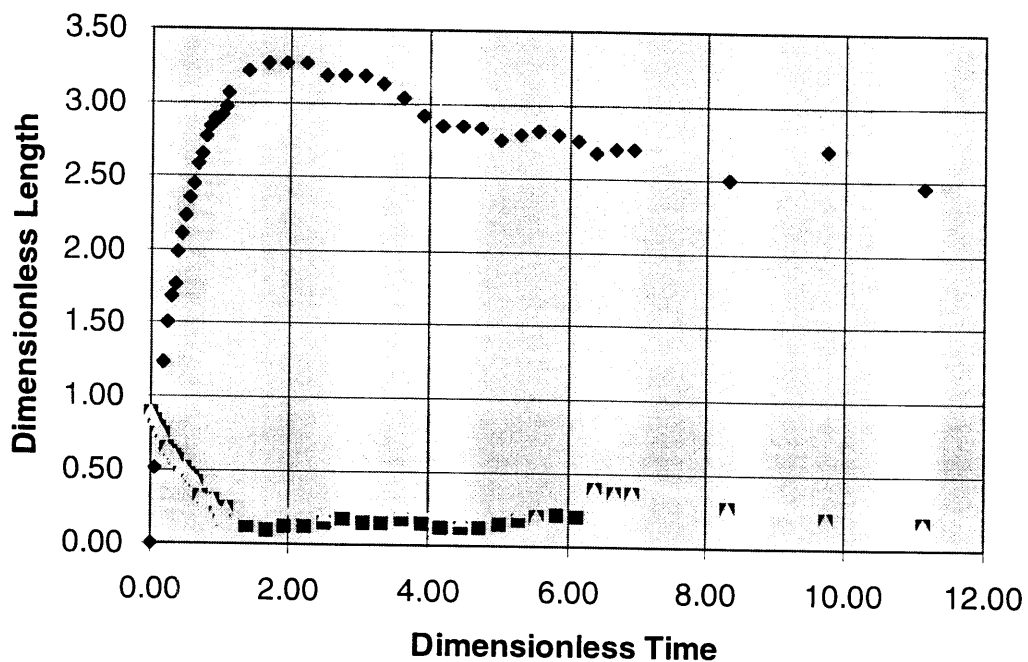
A2.8 ID# 329_3

frame #	t[ms]	τ	ξ	βctr	βother	βmax
993	0.00	0.00	0.00	0.85	0.00	0.85
995	0.22	0.07	0.56	0.81	0.00	0.81
997	0.44	0.14	0.95	0.74	0.00	0.74
999	0.67	0.21	1.20	0.67	0.00	0.67
1001	0.89	0.27	1.41	0.67	0.00	0.67
1003	1.11	0.34	1.62	0.56	0.00	0.56
1005	1.33	0.41	1.76	0.53	0.00	0.53
1007	1.56	0.48	1.87	0.46	0.00	0.46
1009	1.78	0.55	2.01	0.42	0.00	0.42
1011	2.00	0.62	2.16	0.39	0.00	0.39
1013	2.22	0.69	2.19	0.35	0.00	0.35
1015	2.44	0.75	2.33	0.32	0.00	0.32
1017	2.67	0.82	2.44	0.28	0.00	0.28
1019	2.89	0.89	2.47	0.25	0.00	0.25
1021	3.11	0.96	2.54	0.25	0.00	0.25
1023	3.33	1.03	2.62	0.21	0.00	0.21
1025	3.56	1.10	2.68	0.18	0.00	0.18
1030	4.11	1.27	2.71	0.14	0.00	0.14
1035	4.67	1.44	2.79	0.14	0.00	0.14
1045	5.78	1.78	2.93	0.18	0.00	0.18

1055	6.89	2.13	2.82	0.18	0.18	0.18
1065	8.00	2.47	2.71	0.14	0.21	0.21
1075	9.11	2.81	2.65	0.11	0.25	0.25
1085	10.22	3.16	2.57	0.21	0.25	0.25
1095	11.33	3.50	2.44	0.21	0.28	0.28
1105	12.44	3.84	2.36	0.25	0.32	0.32
1115	13.56	4.19	2.33	0.53	0.00	0.53
1125	14.67	4.53	2.33	0.74	0.00	0.74
1135	15.78	4.87	2.36	0.88	0.00	0.88
1145	16.89	5.21	2.40	0.95	0.00	0.95
1155	18.00	5.56	2.36	1.06	0.00	1.06
1165	19.11	5.90	2.33	1.16	0.00	1.16
1175	20.22	6.24	2.30	1.16	0.00	1.16
1185	21.33	6.59	2.33	1.20	0.00	1.20
1195	22.44	6.93	2.33	1.20	0.00	1.20
1205	23.56	7.27	2.30	1.20	0.00	1.20
1215	24.67	7.62	2.25	1.20	0.00	1.20
1225	25.78	7.96	2.25	1.13	0.00	1.13
1235	26.89	8.30	2.25	1.06	0.00	1.06
1245	28.00	8.64	2.25	1.02	0.00	1.02
1255	29.11	8.99	2.22	0.95	0.00	0.95
1265	30.22	9.33	2.22	0.88	0.00	0.88
1275	31.33	9.67	2.19	0.74	0.00	0.74
1285	32.44	10.02	2.22	0.71	0.00	0.71
1295	33.56	10.36	2.22	0.64	0.00	0.64
1305	34.67	10.70	2.22	0.53	0.00	0.53
1315	35.78	11.05	2.19	0.46	0.00	0.46
1325	36.89	11.39	2.19	0.42	0.00	0.42
1335	38.00	11.73	2.19	0.39	0.00	0.39
1345	39.11	12.08	2.19	0.28	0.00	0.28
1395	44.67	13.79	2.19	0.28	0.00	0.28
1445	50.22	15.51	2.19	0.35	0.00	0.35
1495	55.78	17.22	2.25	0.28	0.00	0.28
1545	61.33	18.94	2.19	0.25	0.00	0.25
1595	66.89	20.65	2.19	0.32	0.00	0.32
1645	72.44	22.37	2.19	0.28	0.00	0.28
1695	78.00	24.08	2.19	0.25	0.00	0.25
1745	83.56	25.80	2.08	0.28	0.00	0.28
1795	89.11	27.51	2.08	0.28	0.00	0.28
1845	94.67	29.23	2.16	0.25	0.00	0.25
1895	100.22	30.94	2.08	0.28	0.00	0.28
1945	105.78	32.66	2.16	0.28	0.00	0.28
1995	111.33	34.37	2.16	0.25	0.00	0.25
2045	116.89	36.09	2.16	0.25	0.00	0.25

Figure 39: ID# 329_3
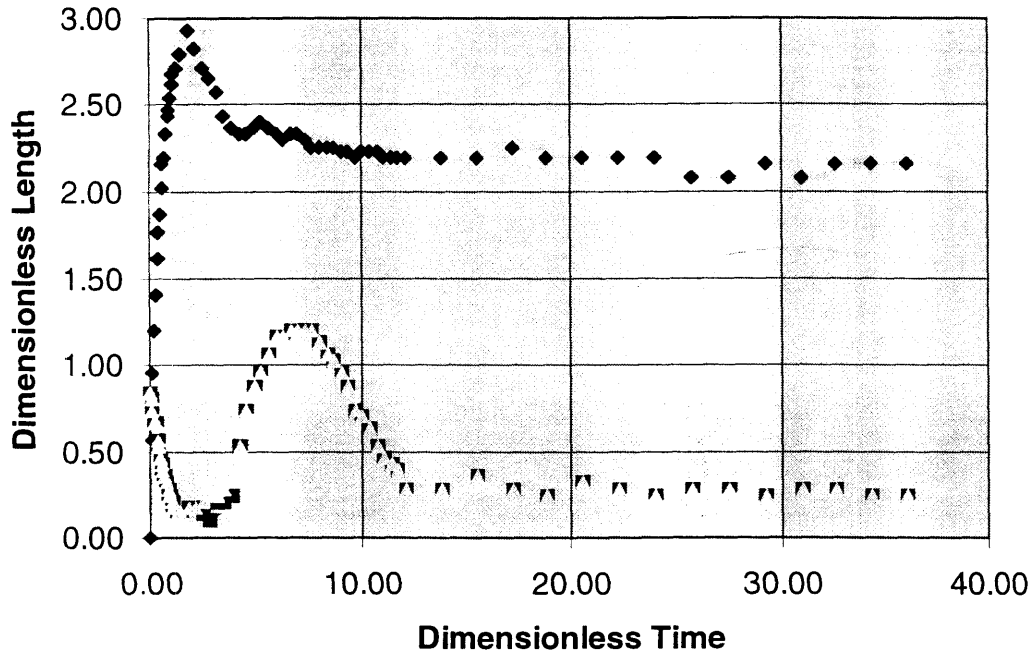
A2.9 ID# 329_4

frame #	t[ms]	τ	ξ	βctr	βother	βmax
1075	0.00	0.00	0.26	0.84	0.00	0.84
1077	0.22	0.07	0.58	0.78	0.00	0.78
1079	0.44	0.14	0.91	0.71	0.00	0.71
1081	0.67	0.20	1.16	0.65	0.00	0.65
1083	0.89	0.27	1.36	0.58	0.00	0.58
1085	1.11	0.34	1.52	0.55	0.00	0.55
1087	1.33	0.41	1.68	0.48	0.00	0.48
1089	1.56	0.48	1.84	0.45	0.00	0.45
1091	1.78	0.55	2.00	0.42	0.00	0.42
1093	2.00	0.61	2.10	0.39	0.00	0.39
1095	2.22	0.68	2.23	0.32	0.00	0.32
1097	2.44	0.75	2.36	0.32	0.00	0.32
1099	2.67	0.82	2.46	0.26	0.00	0.26
1101	2.89	0.89	2.55	0.23	0.00	0.23
1103	3.11	0.96	2.68	0.19	0.00	0.19
1105	3.33	1.02	2.78	0.16	0.00	0.16
1107	3.56	1.09	2.81	0.13	0.00	0.13
1109	3.78	1.16	2.88	0.13	0.00	0.13
1111	4.00	1.23	2.94	0.10	0.00	0.10
1113	4.22	1.30	2.97	0.10	0.00	0.10

1115	4.44	1.37	3.00	0.10	0.16	0.16
1120	5.00	1.54	3.17	0.07	0.13	0.13
1125	5.56	1.71	3.30	0.06	0.13	0.13
1130	6.11	1.88	3.40	0.06	0.13	0.13
1140	7.22	2.22	3.46	0.06	0.16	0.16
1150	8.33	2.56	3.49	0.06	0.16	0.16
1160	9.44	2.90	3.49	0.10	0.16	0.16
1170	10.56	3.24	3.40	0.03	0.19	0.19
1180	11.67	3.58	3.26	0.10	0.16	0.16
1190	12.78	3.93	3.04	0.06	0.23	0.23
1200	13.89	4.27	2.94	0.10	0.19	0.19
1210	15.00	4.61	2.85	0.06	0.23	0.23
1220	16.11	4.95	2.85	0.06	0.19	0.19
1230	17.22	5.29	2.78	0.06	0.16	0.16
1240	18.33	5.63	2.78	0.06	0.16	0.16
1250	19.44	5.97	2.78	0.06	0.16	0.16
1260	20.56	6.32	2.55	0.06	0.16	0.16
1270	21.67	6.66	2.46	0.10	0.16	0.16
1280	22.78	7.00	2.36	0.06	0.16	0.16
1330	28.33	8.71	2.30	0.10	0.00	0.10
1380	33.89	10.41	2.33	0.13	0.00	0.13

Figure 40: ID# 329_4
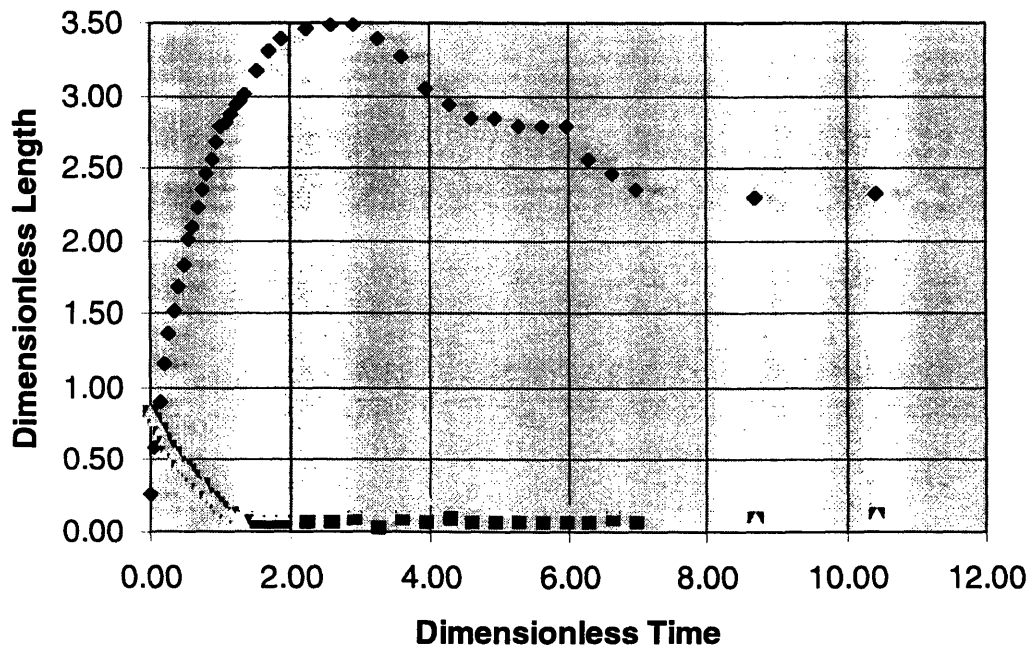
A2.10 ID# 329_5

frame #	t[ms]	τ	ξ	βctr	βother	βmax
1218	0.00	0.00	0.12	0.86	0.00	0.86
1220	0.22	0.06	0.59	0.80	0.00	0.80
1222	0.44	0.13	0.83	0.68	0.00	0.68
1224	0.67	0.19	1.14	0.68	0.00	0.68
1226	0.89	0.26	1.30	0.65	0.00	0.65
1228	1.11	0.32	1.48	0.59	0.00	0.59
1230	1.33	0.39	1.60	0.52	0.00	0.52
1232	1.56	0.45	1.76	0.49	0.00	0.49
1234	1.78	0.51	1.88	0.43	0.00	0.43
1236	2.00	0.58	1.98	0.43	0.00	0.43
1238	2.22	0.64	2.09	0.40	0.00	0.40
1240	2.44	0.71	2.16	0.31	0.00	0.31
1242	2.67	0.77	2.22	0.25	0.00	0.25
1244	2.89	0.83	2.31	0.25	0.00	0.25
1246	3.11	0.90	2.38	0.25	0.00	0.25
1248	3.33	0.96	2.41	0.22	0.00	0.22
1250	3.56	1.03	2.47	0.19	0.00	0.19
1252	3.78	1.09	2.53	0.19	0.00	0.19
1254	4.00	1.16	2.53	0.15	0.00	0.15
1256	4.22	1.22	2.59	0.15	0.00	0.15
1258	4.44	1.28	2.65	0.12	0.19	0.19
1268	5.56	1.60	2.74	0.15	0.19	0.19
1278	6.67	1.93	2.81	0.12	0.25	0.25
1288	7.78	2.25	2.74	0.09	0.22	0.22
1298	8.89	2.57	2.63	0.12	0.22	0.22
1308	10.00	2.89	2.56	0.09	0.31	0.31
1318	11.11	3.21	2.41	0.09	0.31	0.31
1328	12.22	3.53	2.31	0.12	0.31	0.31
1338	13.33	3.85	2.31	0.12	0.34	0.34
1348	14.44	4.17	2.25	0.15	0.37	0.37
1358	15.56	4.49	2.09	0.15	0.40	0.40
1368	16.67	4.81	2.04	0.15	0.40	0.40
1378	17.78	5.13	2.04	0.19	0.40	0.40
1388	18.89	5.45	1.95	0.25	0.37	0.37
1398	20.00	5.78	1.98	0.34	0.00	0.34
1408	21.11	6.10	1.95	0.40	0.00	0.40
1418	22.22	6.42	1.88	0.46	0.00	0.46
1428	23.33	6.74	1.88	0.46	0.00	0.46
1438	24.44	7.06	1.88	0.46	0.00	0.46
1448	25.56	7.38	1.88	0.40	0.00	0.40
1458	26.67	7.70	1.85	0.34	0.00	0.34
1468	27.78	8.02	1.82	0.28	0.00	0.28
1478	28.89	8.34	1.85	0.19	0.22	0.22
1488	30.00	8.66	1.85	0.19	0.22	0.22
1498	31.11	8.98	1.82	0.19	0.25	0.25
1508	32.22	9.31	1.95	0.22	0.28	0.28

1518	33.33	9.63	1.98	0.15	0.25	0.25
1528	34.44	9.95	1.95	0.22	0.28	0.28
1538	35.56	10.27	1.91	0.19	0.25	0.25
1548	36.67	10.59	1.95	0.22	0.28	0.28
1558	37.78	10.91	1.91	0.25	0.00	0.25
1568	38.89	11.23	1.95	0.28	0.00	0.28
1578	40.00	11.55	2.00	0.31	0.00	0.31
1588	41.11	11.87	2.00	0.34	0.00	0.34
1598	42.22	12.19	1.95	0.40	0.00	0.40
1608	43.33	12.51	1.98	0.37	0.00	0.37
1618	44.44	12.83	1.98	0.40	0.00	0.40
1668	50.00	14.44	1.66	0.34	0.00	0.34
1718	55.56	16.04	1.66	0.22	0.28	0.28
1768	61.11	17.65	1.66	0.28	0.00	0.28
1818	66.67	19.25	1.70	0.31	0.00	0.31
1868	72.22	20.86	1.66	0.25	0.28	0.28
1918	77.78	22.46	1.70	0.25	0.00	0.25
1968	83.33	24.06	1.73	0.25	0.00	0.25
2018	88.89	25.67	1.66	0.28	0.00	0.28

Figure 41: 329_5
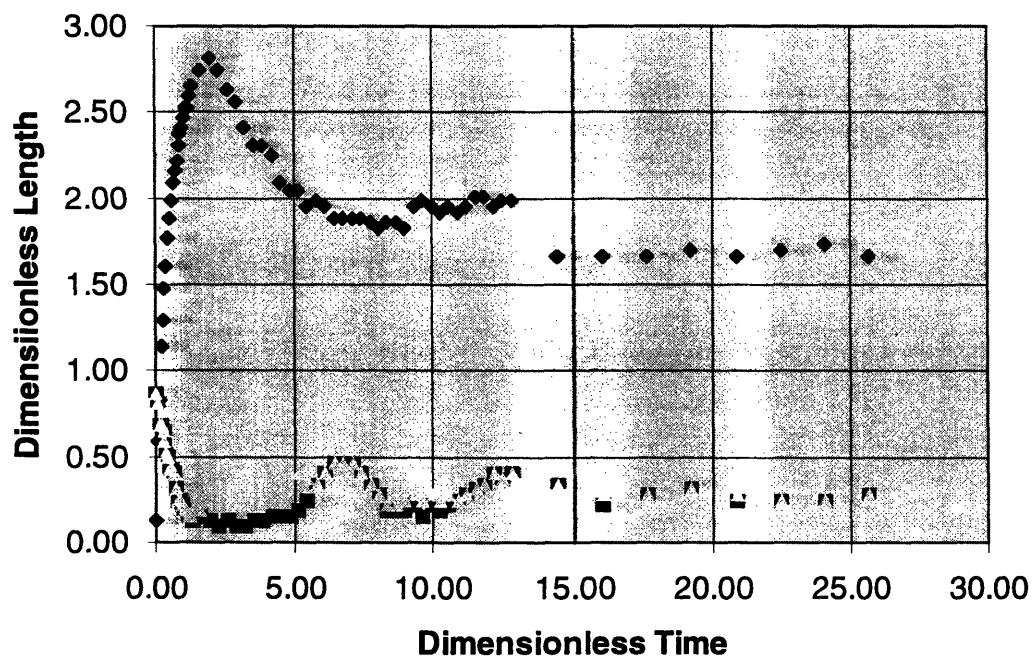
A2.11 ID# 329_6

frame #	t[s]	τ	ξ	βctr	βother	βmax
1469	0.00	0.00	0.07	0.90	0.00	0.90
1471	0.22	0.05	0.45	0.87	0.00	0.87
1473	0.44	0.10	0.67	0.85	0.00	0.85
1475	0.67	0.15	0.95	0.77	0.00	0.77
1477	0.89	0.20	1.15	0.75	0.00	0.75
1479	1.11	0.24	1.32	0.70	0.00	0.70
1481	1.33	0.29	1.44	0.65	0.00	0.65
1483	1.56	0.34	1.59	0.60	0.00	0.60
1485	1.78	0.39	1.72	0.55	0.00	0.55
1487	2.00	0.44	1.80	0.50	0.00	0.50
1489	2.22	0.49	1.93	0.47	0.00	0.47
1491	2.44	0.54	2.02	0.45	0.00	0.45
1493	2.67	0.59	2.10	0.42	0.00	0.42
1495	2.89	0.64	2.14	0.40	0.00	0.40
1497	3.11	0.68	2.20	0.32	0.00	0.32
1499	3.33	0.73	2.27	0.32	0.00	0.32
1501	3.56	0.78	2.33	0.30	0.00	0.30
1503	3.78	0.83	2.44	0.27	0.00	0.27
1505	4.00	0.88	2.51	0.25	0.00	0.25
1507	4.22	0.93	2.54	0.23	0.00	0.23
1509	4.44	0.98	2.50	0.23	0.00	0.23
1511	4.67	1.03	2.55	0.17	0.00	0.17
1513	4.89	1.08	2.57	0.20	0.00	0.20
1515	5.11	1.12	2.60	0.20	0.00	0.20
1525	6.22	1.37	2.72	0.15	0.20	0.20
1535	7.33	1.61	2.77	0.10	0.17	0.17
1545	8.44	1.86	2.77	0.12	0.15	0.15
1555	9.56	2.10	2.72	0.15	0.17	0.17
1565	10.67	2.35	2.69	0.12	0.20	0.20
1585	12.89	2.83	2.67	0.10	0.20	0.20
1605	15.11	3.32	2.69	0.15	0.20	0.20
1625	17.33	3.81	2.67	0.20	0.27	0.27
1645	19.56	4.30	2.65	0.17	0.30	0.30
1665	21.78	4.79	2.48	0.17	0.27	0.27
1685	24.00	5.28	2.40	0.20	0.23	0.23
1705	26.22	5.77	2.33	0.27	0.00	0.27
1725	28.44	6.26	2.10	0.30	0.00	0.30
1745	30.67	6.74	2.07	0.27	0.00	0.27
1765	32.89	7.23	2.05	0.30	0.00	0.30
1785	35.11	7.72	2.00	0.23	0.00	0.23
1805	37.33	8.21	2.02	0.23	0.00	0.23
1825	39.56	8.70	1.97	0.20	0.00	0.20
1845	41.78	9.19	1.95	0.17	0.00	0.17
1865	44.00	9.68	1.93	0.15	0.00	0.15

Figure 42: ID# 329_6
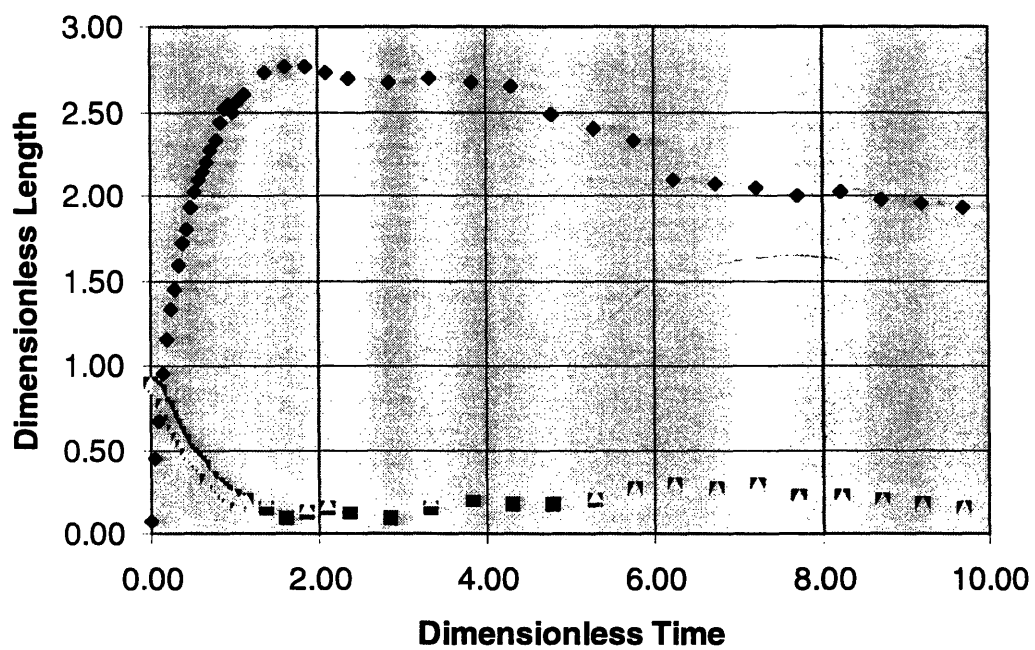
REFERENCES

[1] Chandra, S. and Avedisian, C. T. "On the Collision of a Droplet with a Solid Surface" in *Proceedings of the Royal Society of London A*, Vol. 432, 1991, pgs. 13-41.

[2] Engel, O. "Waterdrop Collisions With Solid Surfaces" in *Journal of Research of the National Bureau of Standards*, Vol. 54, 1955, pgs. 281-298.

[3] Worthington, A. M. "On the Forms Assumed by Drops of Liquids Falling Vertically on a Horizontal Plate" in *Proceedings of the Royal Society of London*, Vol 25, 1877, pgs. 261-271.

[4] Savic, P. and Boult, G. T. "The Fluid Flow Associated with the Impact of Liquid Drops with Solid Surfaces," National Research Laboratories of Canada Report MT-26, Ottawa, Canada, 1955.

[5] Harlow, F. H., Shannon, J. P., and Welch, J. E. "Liquid Waves by Computer" in *Science*, Vol. 14, 1965, pgs. 1092-1093.

[6] Harlow, F. H. and Welch, J. E. "Numerical Calculation of Time-Dependent Viscous Incompressible Flow of Fluid with Free Surface" in *Physics of Fluids*, Vol. 8, No. 12, 1965, pgs. 2182-2189.

[7] Harlow, F. H. and Shannon, J. P. "The Splash of a Liquid Drop" in *Journal of Applied Physics*, Vol. 38, No. 10, 1967, pgs. 3855-3866.

[8] Harlow & Shannon "Splash" p. 3859.

[9] Harlow & Shannon "Splash" p. 3861.

[10] Jones, H. "Cooling, Freezing, and Substrate Impact of Droplets Formed by Rotary Atomization" in *Journal of Applied Physics D*, Vol. 4, 1971, pgs. 1657-1660.

[11] Bennett, T. and Poulikakos, D. "Splat-Quench Solidification: Estimating the Maximum Spreading of a Droplet Impacting a Solid Surface" in *Journal of Materials Science*, Vol. 28, 1993, p. 964.

[12] Madejski, J. "Solidification of Droplets on a Cold Surface" in *International Journal of Heat and Mass Transfer*, Vol. 19, 1976, pgs. 1009-1013.

[13] Madejski "Solidification" p. 1012.

[14] Madjeski, J. "Droplets on Impact With a Solid Surface" in *International Journal of Heat and Mass Transfer*, Vol. 26, No. 7, 1983, pgs. 1095-1098.

[15] Collings, E. W., Markworth, A. J., McCoy, J. K., and Saunders, J. H. "Splat-Quench Solidification of Freely Falling Liquid-Metal Drops by Impact on a Planar Substrate" in *Journal of Materials Science*, Vol. 25, 1990, pgs. 3677-3682.

[16] Bennett & Poulikakos, p. 965.

[17] Chandra, S. and Avedisian, C. T. "Droplet Impact on a Porous Surface" in *HTD-Phase Change Heat Transfer*, Vol. 159, 1991, pgs. 17-25.

[18] Chandra & Avedisian "On the Collision" p. 21.

[19] Trapaga, G. and Szekely, J. "Mathematical Modeling of the Isothermal Impingement of Liquid Droplets in Spraying Processes" in *Metallurgical Transactions B*, Vol. 22B, 1991, pgs. 901-914.

[20] Trapaga, G., Matthys, E. F., Valencia, J. J., and Szekely, J. "Fluid Flow, Heat Transfer, and Solidification of Molten Metal Droplets Impinging on Substrates: Comparison of Numerical and Experimental Results" in *Metallurgical Transactions B*, Vol. 23B, 1992, pgs. 701-718.

[21] Trapaga & Szekely, "Mathematical" p. 909.

[22] Trapaga & Szekely, "Mathematical" p. 907.

[23] Fukanuma, H. and Ohmori, A. "Behavior of Molten Droplets Impinging on Flat Surfaces" in *Proceedings of the 7th National Thermal Spray Conference*, 1994, pgs. 563-568.

[24] Sobolev, V. V. and Guilemany, J. M. "Flattening of Thermally Sprayed Particles" in *Materials Letters*, Vol. 22, 1995, pgs 209-213.

[25] Sobolev, p. 209.

[26] Shi, M. H., Bai, T. C., and Yu, J. "Dynamic Behavior and Heat Transfer of a Liquid Droplet Impinging on a Solid Substate" in *Experimental Thermal and Fluid Science*, Vol. 6, 1993, pgs. 202-207.

[27] Bennett, T. and Poulikakos, D. "Splat-Quench Solidification: Estimating the Maximum Spreading of a Droplet Impacting a Solid Surface" in *Journal of Materials Science*, Vol. 28, 1993, pgs. 963-970.

[28] Bennett & Poulikakos, p. 964.

[29] Fukai, J., Zhao, Z., Poulikakos, D., Megaridis, C. M, and Miyatake, O. "Modeling of the Deformation of a Liquid Droplet Impinging Upon a Flat Surface" in *Physics of Fluids A*, Vol. 5, 1993, pgs. 2588-2599.

[30] Fukai et al. "Modeling" p. 2588.

[31] Fukai, J., Shiiba, T., Yamamoto, T., Miyatake, O., Poulikakos, D., Megaridis, C. M., and Zhao, Z. "Wetting Effects on the Spreading of a Liquid Droplet Colliding with a Flat Surface: Experiments and Modeling" in *Physics of Fluids A*, Vol. 7, No. 2, 1995, pgs. 236-247.

[32] Liu, W., Wang, X., and Matthys, E. F. "Thermal Analysis and Measurements for a Molten Metal Drop Impacting on a Substrate: Cooling, Solidification, and Heat Transfer Coefficient" in *International Journal of Heat and Mass Transfer*, Vol. 38, No. 8, 1995, pgs. 1387-1395.

[33] Wang, G. X. and Matthys, E. F. "Numerical Modeling of Phase Change and Heat Transfer During Rapid Solidification Processes: Use of Control Volume Integrals with Element Subdivision" in *International Journal of Heat and Mass Transfer*, Vol. 35, No. 1, 1992, pgs. 141-153.

[34] Kang, B., Zhao, Z., and Poulikakos, D. "Splat-Quench Solidification of Two Liquid Metal Droplets Impacting Sequentially on a Solid Surface" in *Journal of Heat Transfer*, 1994.

[35] Rolland, M. "Spray Forming: Droplet Microstructure and Impingement Behavior" *M. S. Thesis*, MIT, 1996.

[36] Poirier, D. R. and Geiger, G. H. Transport Phenomena in Materials Processing. Warrendale, PA: TMS, 1994, p. 345.

[37] Poirier & Geiger, pgs. 345-346.

[38] Smithells, C. J., Ed. Metals Reference Book, 5th Ed., 1976, pgs. 14-7 to 14-8.

[39] Iida, T. and Guthrie R., The Physical Properties of Liquid Metals, 1993, p. 232.

[40] Iida & Guthrie, p. 91.

[41] Peker, A. and Johnson, W. L. "Time-Temperature-Transformation Diagram of a Highly Processable Metallic Glass" in *Materials Science and Engineering*, Vol. A179/A180, 1994, p. 174.

[42] Lee, D., Personal Communication.

[43] Boyce, W. E. and DiPrima, R. C. <u>Elementary Differential Equations and Boundary Value Problems</u>, 2nd Ed. New York: John Wiley and Sons, 1969, pgs. 353-355.

[44] White, F. M. <u>Viscous Fluid Flow</u> New York: McGraw-Hill, 1974.

[45] Scheller, B. L. and Bousfield, D. W. "Newtonian Drop Impact with a Solid Surface" in *AIChE Journal*, Vol. 41, No. 6, 1995, pgs. 1358-1367.

BIBLIOGRAPHY

Akao, F., Araki, K., Mori, S., and Moriyama, A. "Deformation Behaviors of a Liquid Droplet Impinging onto Hot Metal Surface" in *Transactions ISU*, Vol. 20, 1980, pgs. 737-743.

Bennett, T. and Poulikakos, D. "Heat Transfer Aspects of Splat-Quench Solidification: Modeling and Experiment" in *Journal of Materials Science*, Vol. 29, 1994, pgs. 2025-2039.

Bertagnolli, M., Marchese, M., and Jacucci, G. "Modeling of Particles Impacting on a Rigid Substrate Under Plasma Spraying Conditions" in *Journal of Thermal Spray Technology*, Vol. 4, 1995, pgs. 41-49.

Bianchi, L. Blein, F., Lucchese, P., Vardelle, M., Vardelle, A., and Fauchais, P. "Effect of Particle Velocity and Substrate Temperature on Alumina and Zirconia Splat Formation" in *Proceedings of the 7th National Thermal Spray Conference*, 1994, pgs. 569-574.

Bianchi, L., Lucchese, P., Denoirjean, P., and Fauchais, P. "Zirconia Splat Formation and Resulting Coating Properties" in *Proceedings of the 8th National Thermal Spray Conference*, 1995, pgs. 261-266.

Busch, R., Kim, Y. J. and Johnson, W. L. "Thermodynamics and Kinetics of the Undercooled Liquid and the Glass Transition of the $Zr_{41.2}Ti_{13.8}Cu_{12.5}Ni_{10.0}Be_{22.5}$ Alloy."

Chandra, S. and Avedisian, C. T. "Droplet Impact on a Porous Surface" in *HTD-Phase Change Heat Transfer*, Vol. 159, 1991, pgs. 17-25.

Cheng, Lung. "Dynamic Spreading of Drops Impacting onto a Solid Surface" in *Ind. Chem. Process Des. Dev.*, Vol. 16, No. 2, 1977, pgs. 192-197.

Fantassi, S., Vardelle, M., Vardelle, A., and Fauchais, P. "Influence of the Velocity of Plasma Sprayed Particles on the Splat Formation" in *Proceedings of the 1993 National Thermal Spray Conference*, 1993, pgs. 1-6.

Floryan, J. M. and Rasmussen, H. "Numerical Methods for Viscous Flows with Moving Boundaries" in *Appl. Mech. Rev.*, Vol. 42, No. 12, 1989, pgs. 323-341.

Grest, G. S. and Cohen, M. H. "Liquid-Glass Transistion: Dependence of the Glass Transition on Heating and Cooling Rates" in *Physical Review B*, Vol. 21, No. 9, 1980, pgs. 4113-4117.

Gutierrez-Miravette, E., Lavernia, E. J., Trapaga, G., Szekely, J., and Grant, N. J. "A Mathematical Model of the Spray Deposition Process" in *Metallurgical Transactions A*, Vol. 20A, 1989, pgs. 71-85.

Hocking, L. M. "The Wetting of a Plane Surface by a Fluid" in *Physics of Fluids*, Vol. 7, No. 6, 1995, pgs. 1214-1219.

Incropera, F. P. and DeWitt, D. P. Introduction to Heat Transfer, 2nd Ed. New York: John Wiley and Sons, 1990.

Johnson, W. L. and Peker, A. "Synthesis and Properties of Bulk Metallic Glasses," Kluwer Academic Publishing, 1995, pgs. 25-41.

Kim, Y. J., Busch, R., Johnson, W. L., Rulison, A. J., and Rhim, W. K. "Metallic Glass Formation in Highly Undercooled $Zr_{41.2}Ti_{13.8}Cu_{12.5}Ni_{10.0}Be_{22.5}$ During Containerless Electrostatic Levitation Processing" in *Appl. Phys. Lett.*, Vol. 65, 1994, pgs. 2136-2138.

Liu, J. and Spalding, D. B. "Numerical Simulation of Flows With Moving Interfaces" in *PhysicoChemical Hydronamics*, Vol. 10, No. 5/6, 1988, pgs. 625-637.

Liu, H., Lavernia, E. J., Rangel, R. H., Muehlberger, E., and Sickinger, A. "Deformation and Interaction Behavior of Molten Droplets Impinging on a Flat Substrate in Plasma Spray Process" in *Proceedings of the 1993 National Thermal Spray Conference*, 1993, pgs. 457-462.

Liu, H., Lavernia, E. J., and Rangel, R. H. "Numerical Simulation of Substrate Impact and Freezing of Droplets in Plasma Spray Processes" in *Journal of Applied Physics*, Vol. 26, 1993, pgs. 1900-1908.

Liu, H., Lavernia, E. J., Rangel, R. H., Muehlberger, E., and Sickinger, A. "Numerical Investigation of Micro-Pore Formation During Substrate Impact of Molten Droplets in Spraying Processes" in *Proceedings of the 7th National Thermal Spray Conference*, 1994, pgs. 375-380.

Moreau, C., Cielo, P., and Lamontagne, M. "Flattening and Solidification of Thermally Sprayed Particles" in *Journal of Thermal Spray Technology*, Vol. 1, 1992, pgs. 317-323.

Pasandideh-Fard, M. and Mostaghimi, J. "Deformation and Solidification of Molten Particles on a Substrate in Thermal Plasma Spraying" in *Proceedings of the 7th National Thermal Spray Conference*, 1994, pgs. 405-414.

Peker, A. and Johnson, W. L. "A Highly Processable Metallic Glass: $Zr_{41.2}Ti_{13.8}Cu_{12.5}Ni_{10.0}Be_{22.5}$" in *Appl. Phys. Lett.*, Vol. 63, 1993, pgs. 2342-2344.

SanMarchi, C., Liu, H., Lavernia, E. J., Rangel, R. H., Sickinger, A., and Muehlberger, E. "Numerical Analysis of the Deformation and Solidification of a Single Droplet Impinging onto a Flat Substrate" in *Journal of Materials Science*, Vol. 28, 1993, pgs. 3313-3321.

Savic, P. and Boult, G. T. "The Fluid Flow Associated with the Impact of Liquid Drops with Solid Surfaces," National Research Laboratories of Canada Report MT-26, Ottawa, Canada, 1955.

Stow, C. D. and Hadfield, M. G. "An Experimental Investigation of Fluid Flow Resulting from the Impact of a Water Drop with an Unyielding Dry Surface" in *Proceedings of the Royal Society of London A*, Vol. 373, 1981, pgs. 419-441.

Vardelle, M., Vardelle, A., Leger, A. C., and Fauchais, P. "Influence of the Particle Parameters at Impact on Splat Formation and Solidification in Plasma Spraying Processes" in *Proceedings of the 1993 National Thermal Spray Conference*, 1993, pgs. 555-574.

Watanabe, T., Kuribayashi, I., Honda, T., and Kanzawa, A. "Deformation and Solidification of a Droplet on a Cold Substrate" in *Chemical Engineering Science*, Vol. 47, No. 12, 1992, pgs. 3059-3065.

Westhoff, R., Trapaga, G., and Szekely, J. "Plasma-Particle Interactions in Plasma Spraying Systems" in *Metallurgical Transactions B*, Vol. 23B, 1992, pgs. 683-693.